

Experimental and computational study of unsaturated flow in a stack of thin layers

Application to non-woven hygiene products

Amir Hossein Tavangarrad

Reading and examination committee:

Prof. M.Th. van Genuchten

Prof. M. Prat

Prof. A. Ahmadi

Prof. J. M. Huyghe

Dr. A. Raof

Copyright © 2019 by Amir Hossein Tavangarrad

All rights reserved. No part of this material may be copied or reproduced in any way without prior permission of the author.

ISBN: 978-90-6266-526-6

Title: Experimental and computational study of unsaturated flow in a stack of thin layers; Application to non-woven hygiene products

NUR code: 934

NUR description: Hydrology

Number of pages: 164

Cover photo by: Amir Hossein Tavangarrad

Cover layout: Margot Stoete

Printed by: ProefschriftMaken || www.proefschriftmaken.nl

Experimental and computational study of unsaturated flow in a stack of thin layers

Application to non-woven hygiene products

Experimentele en computationele studie van onverzadigde stroming in een stapeling van dunne lagen

toepassingen voor niet-geweven hygiënische producten

(met een samenvatting in het Nederlands)

Proefschrift

ter verkrijging van de graad van doctor
aan de Universiteit Utrecht
op gezag van de rector magnificus, prof.dr. H.R.B.M. Kummeling,
ingevolge het besluit van het college voor promoties
in het openbaar te verdedigen op
woensdag 6 februari 2019 des middags te 2.30 uur

door

Amir Hossein Tavangarrad

geboren op 9 mei 1988
te Shahreza, Iran

Promotor: Prof.dr.ir. S.M. Hassanizadeh

Copromotor: R. Rosati

This thesis was accomplished with the financial support from European Research Council (ERC) under the contract no. 341225, entitled: SCIPORE (A new paradigm in modeling flow and transport in porous media: revisiting foundations of porous media science) and by Procter and Gamble.

To my wife and son; Elham and Sam...

Those who went in pursuit of knowledge

Soared up so high, stretched the edge

Khayyam, Persian poet

Contents

Chapter 1: Introduction

1.1	Background and motivation	3
1.2	Hydraulic properties of thin fibrous layers	4
1.3	Effect of inter-layer space on unsaturated fluid flow in a stack of thin fibrous layers	8
1.3.1	Gravimetric measurements of wicking from layer to layer	8
1.3.2	X-ray measurements of wicking from layer to layer	10
1.3.2.1	Experiments by Weder et al (2006)	10
1.3.2.2	Experiments by Birrfelder et al. (2013)	13
1.3.3	Continuum-scale modeling of a stack of thin fibrous layers and their interfaces	16
	References	17

Chapter 2: Measurements of capillary pressure-saturation curves of thin hydrophilic fibrous layers; effects of overburden pressure, number of layers, and multiple imbibition-drainage cycles

	Abstract	22
2.1	Introduction	23
2.2	Methods and materials	25
2.2.1	Materials	25
2.2.2	Experimental setup	25
2.2.3	Experimental procedure	26
2.2.4	Fitting of data points	27
2.3	Results	28
2.3.1	Influence of overburden pressure	28

2.3.2	Influence of number of layers	30
2.3.3	Influence of multiple imbibition-drainage cycles	32
2.3.4	Effect of layer material	33
2.4	Scaling of Pc_s curves using Leverett J-function	35
2.5	Conclusions	37
2.6	Appendix A: Influence of capillarity on liquid accumulation inside the chamber	38
2.7	Appendix B: Influence of equilibration threshold value	41
2.8	Appendix C: Dynamics of flow during measurements of Pc_s curves	41
	References	43

Chapter 3: Continuum-scale modeling of liquid redistribution in a stack of thin hydrophilic fibrous layers

	Abstract	48
3.1	Introduction	49
3.2	Experimental methods and materials	52
3.2.1	Materials	52
3.2.2	NMR instrument	52
3.2.3	Water redistribution experiment	54
3.3	Modeling approaches	55
3.3.1	Richards model	55
3.3.2	Reduced continua model (RCM)	57
3.4	Numerical simulations	59
3.4.1	Values of model parameters	59
3.4.2	Richards model solution	60
3.4.3	RCM solution	61
3.5	Results	62
3.5.1	Water redistribution Experiment	62
3.5.2	Results of simulation with Richards model	63

3.5.3	Results of simulation with RCM.....	65
3.6	Discussion and conclusions.....	67
	References.....	68

Chapter 4: Continuum-scale modeling of water infiltration in a stack of two thin fibrous layers and their interface

	Abstract.....	72
4.1	Introduction.....	73
4.2	Materials and experiments.....	76
4.3	Characterization approaches.....	79
4.4	Numerical approaches.....	88
4.5.1	Governing equations.....	88
4.5.2	RCM approach.....	89
4.5	Numerical implementation.....	91
4.5.1	Richards model.....	91
4.5.2	Reduced continua model.....	91
4.5.3	Boundary conditions.....	91
4.6	Results and discussion.....	92
4.7	Conclusion.....	97
4.8	Appendix A: Relative permeability function of a thin fibrous layer using pore morphology method and van Genuchten fitting parameters.....	97
	References.....	98

Chapter 5: Experimental and numerical study of dynamic non-equilibrium in a thin non-woven fibrous layer

	Abstract.....	102
5.1	Introduction.....	103
5.2	Experimental methods and materials.....	104
5.2.1	Materials.....	104
5.2.2	Autoporosimeter setup.....	107
5.2.3	One step and multistep inflow/outflow experiment.....	108

5.3	Modeling approaches	109
5.3.1	Two-phase flow model and the Richards equation	109
5.3.3	Reduced continua model (RCM).....	111
5.4	Numerical simulations	113
5.4.1	Values of input parameters	113
5.4.2	Two phase flow solutions	114
5.4.3	Solution of the Richards model	115
5.4.4	Solution of the Reduced Continua Model (RCM).....	116
5.5	Results and discussion	116
5.5.1	Dynamic inflow experiments	116
5.5.2	Dynamic inflow simulation results using the two-phase flow and Richards models	118
5.5.3	Results of one-step inflow simulations using the Reduced Continua Model (RCM).....	125
5.5.4	Dynamic outflow experiments.....	128
5.5.5	Dynamic outflow simulations using the two phase flow model and Reduced Continua Model (RCM).....	129
5.6	Conclusions	133
	References	134
 Chapter 6: Summary and conclusions		
6.1	Conclusions	138
	Samenvatting	144
	Acknowledgements	152

Chapter 1

Introduction

1.1 Background and motivation

Engineered fibrous substrates are widely used for managing liquid absorption and distribution in many products, including sanitary products, wound dressings, and diapers. Most of these products are structured in a multilayer fashion with varying geometries and functionalities. Understanding unsaturated fluid flow through the layers and their interstices is essential to optimally design such products.

Sanitary paper products such as disposable diapers are designed to keep moisture and vapor away from the skin. Thus, their layers are engineered to facilitate fluid movement from the top fibrous sheet next to the skin towards a core storage layer consisting of super absorbent polymer grains. The storage core is backed with an impermeable layer to avoid leakage from the product. Key transport processes are involved simultaneously, such as two-phase flow in thin fibrous layers and their interlayer spaces, swelling of super absorbent particles, deformation of the storage layer, and evaporation of liquid from the layers. Managing unsaturated fluid flow has great impact on the dryness of the top layer and comfortability for users.

Non-woven thin fibrous layers used in sanitary products are deformable soft porous materials with a high porosity and permeability. Hence, void spaces in such layers can easily change upon external compression. This will apparently influence the interaction of fluid with the fibers and intra-fiber void spaces. Additionally, since fibrous layers are consisting of many fibers that could be arranged in different ways to produce fabrics with diverse fiber orientations and fiber length distributions, the void space of a layer may consist of pores with irregular shapes and unclear boundaries. Therefore, many challenges lie ahead of characterization and modeling such layers.

Given the fact that thin non-woven layers are stacked together and each single thin layer has less than 10-15 pores along its thickness, the role of interlayer space is of great importance in unsaturated fluid flow. Many knowledge gaps about these topics exist in the literature, particularly in terms of modeling the basic processes involved. Additional studies are hence very much needed.

The main focus of this dissertation is on the characterization and continuum-scale modeling of thin non-woven fibrous layers and their interfaces. Different experimental and modeling techniques have been employed to describe a thin fibrous layer, which has only a few pores along its thickness. A comprehensive

study was carried out about traditional continuum-scale modeling approaches, while a recently proposed approach, called the Reduced Continua Model (RCM), will be used to simulate unsaturated fluid flow through the layers and their interfaces.

The structure of this thesis is as follows. In the next subsection of this introduction chapter, an overview of previous studies on measuring and modeling the hydraulic properties of thin fibrous layers are given. Moreover, results of a few studies, which have reported liquid transfer from a fabric layer to another layer, are reviewed and summarized in a final subsection of this chapter. In Chapter 2, the effects of overburden pressure, number of layers, and multiple imbibition-drainage cycles on measurements of the capillary pressure-saturation curves of thin hydrophilic fibrous layers are discussed. Chapter 3 is devoted to a study of continuum-scale modeling of liquid redistribution in a stack of thin hydrophilic fibrous layers. Simulations of liquid infiltration in a stack of two thin fibrous layers and their interface are presented in Chapter 4. Furthermore, dynamic non-equilibrium conditions in thin non-woven fabric during one-step inflow/outflow experiments are investigated, both numerically and experimentally, in Chapter 5. Finally, summary and conclusions are provided in Chapter 6.

1.2 Hydraulic properties of thin fibrous layers

A porous medium can be characterized by its porosity, absolute and relative permeabilities, and the capillary pressure-saturation relationship, among other properties that serve as input parameters for macroscopic models. Determination of constitutive correlations, namely the relative permeability and capillary pressure-saturation functions for fluid flow through thin fibrous layers, has received relatively little attention up to now. Measuring these relationships for thin layers has several challenges since they have only a few pores along their thickness. In this sub-section we briefly introduce some experimental and numerical studies that have been done to determine properties of thin fibrous layer.

Porosity, being one of the most fundamental characteristics of porous media, is defined as the void volume of the porous matrix over its total volume. One simple way for calculating thin layer porosity was proposed by Mathias et al. (2003):

$$\varphi = \frac{1 - V^s}{Ab} \quad (1.1)$$

where φ is the porosity, A is the area of the thin fibrous layer sample, b is the thickness of the material, and V^s is the volume of solid phase given by:

$$V^s = \frac{m^s}{\rho^f} \quad (1.2)$$

where m^s is the solid mass of the fibrous layer, and ρ^f the fiber density. Shortcoming of this approach is difficulty in determining the thin layer thickness. Since a thin fibrous layer is not perfectly flat and since only a few pores are present along its thickness, the boundary of the material is always poorly defined, while calculated porosities based on the average thickness may be unreliable.

Porosimetry is a relatively standard method to determine the porosity of thin fibrous layers and measure their capillary pressure-saturation relationships (e.g. Miller and Tyomkin, 1994). Using this approach, the maximum liquid uptake of a thin fabric sample can be measured and, accordingly, the porosity given by:

$$\varphi = \frac{m_{max}^l}{m_{max}^l + \frac{\rho^l}{\rho^f} m^s} \quad (1.3)$$

where m_{max}^l is the maximum mass of the liquid phase, and ρ^l the liquid density.

Imaging is another approach for determination of fibrous layer porosities. For instance, a μ CT scanner can be used to obtain images of a thin fibrous layer. The porosity of a layer can be obtained subsequently from its binarized images such as shown by Mohebbi et al. (2018), among others.

The intrinsic permeability is also a key characteristic of porous layer reflecting the permeability of the porous substrate to single phase fluid flow. The intrinsic permeability coefficient appears in Darcy's law, which is an empirical constitutive relation describing multiphase flow in porous media. Assuming laminar flow and neglecting gravity, the Darcy velocity vector \mathbf{v}^w for a two-phase flow system is given by:

$$\mathbf{v}^i = -\frac{k^{r,i}K}{\mu^i} \nabla P^i \quad (1.4)$$

where K is the intrinsic permeability, $k^{r,i}$ is the relative permeability of phase i , μ^i is the dynamic viscosity of phase i , and ∇P^i is the pressure gradient. A range of experimental and numerical modeling investigations exist about the intrinsic permeability of fibrous layers (Tomadakis and Robertson 2005). A comprehensive literature review of studies of the intrinsic permeability of fibrous media is reported by Tomadakis and Robertson (2005). Many empirical relations for the intrinsic permeability have been defined based on porosity and the fiber radii of the fibrous layer (e.g., Tomadakis and Robertson 2005; Jackson and James 1986; Davies 1973; Spielman and Goren 1968). For example, Jackson and James (1986) developed the following formula based on flow through three-dimensional arrays of cylinders to predict the permeability of a highly porous fabric (having porosities above 0.7):

$$K = \frac{3 r^2}{20(1 - \varphi)} (-\ln(1 - \varphi) - 0.931) \quad (1.5)$$

where r is the fiber radius.

The effective permeability of porous media under unsaturated conditions is a product of the intrinsic permeability and the relative permeability. The relative permeability function, $k^{r,i}$, is a dimensionless modifier within a range of 0 to 1, which is assumed to be function of saturation only (Kaviany 1995). One common formula for the wetting phase relative permeability was suggested by Van Genuchten (1980) as:

$$k^{r,w}(S^w) = S_e^l (1 - (1 - S_e^{1/m})^m)^2 \quad (1.6)$$

where m is the same parameter that appears in the $P^c - S^w$ relationship, $l = 0.5$, S^w is the saturation of the wetting phase, and $S_e = (S^w - S_{ir})/(1 - S_{ir})$ is effective saturation in which S_{ir} is the irreducible water saturation. Due to very large porosities of the samples, no residual air needs to be considered. Another formulation for the relative permeability is a power-law model based on the empirical correlation of Brooks and Corey (1964):

$$k^r(S^w) = (S^w)^\delta \quad (1.7)$$

where δ is as a material property and should be determined experimentally. Several experimental studies exist for determining δ of a thin fibrous layer (Sole

2008; Hussaini and Wang 2010). For the in-plane permeability, Hussaini and Wang (2010) found a value of $\delta=4$ for a thin non-woven fibrous layer, but they reported large uncertainties in their measurements of the through-plane permeability (Hussaini and Wang 2010). A wide range of values for this coefficient ($3 \leq \delta \leq 6$) has been used in numerical simulations of thin fibrous layers (Jaganathan et al. 2009; Landeryou et al. 2005; Ashari and Tafreshi 2009).

One of the most important characteristics of porous media is the capillary pressure-saturation relationship. This relationship expresses the pressure difference between the non-wetting and wetting phases as follow:

$$P^{nw} - P^w = P^c(S^w) \quad (1.8)$$

in which P^{nw} is the non-wetting phase pressure, P^w is the wetting phase pressure and $P^c(S^w)$ is the capillary pressure, which traditionally is assumed to be a solely function of saturation. A nonlinear relationship suggested by van Genuchten (VG) can be used for the capillary pressure function as follows:

$$P^c(S_e) = \frac{1}{\alpha} (S_e^{-1/m} - 1)^{1/n} \quad (1.9)$$

where α and n are fitting parameters, and $m = 1 - 1/n$. All parameters in this equation have to be determined experimentally. A number of studies focusing on measurements of capillary pressure-saturation relationships of thin non-woven fabrics are reported in the literature. Several of these concern $P_c(S)$ curves of water-air systems involving the gas diffusion layer (GDL) of polymer electrolyte fuel cells (PEFC) (see e.g., Sole 2008; Gostick et al. 2006; Gostick et al. 2008; Nguyen et al. 2006; Kumbur et al. 2007a; Fairweather et al. 2007; Jena and Gupta 2005; Nguyen et al. 2008). A comprehensive review of available techniques employed for GDLs is reported in a study by Sole et.al (2008). Some measurements have been carried out also to determine the capillary pressure-saturation relationships of thin hydrophilic fabrics used in medical and hygienic absorbent products (Landeryou et al. 2005; Jaganathan et al. 2009a; Tavangarrad et al. 2018). More detailed information about numerical and experimental works of the capillary pressure-saturation relationships of thin non-woven fabrics is provided in Chapter 2.

1.3 Effect of inter-layer space on unsaturated fluid flow in a stack of thin fibrous layers

The mechanism of water transfer from one fibrous layer to another layer has gained much interest in the textile research fields such as those dealing with multilayer clothing fabrics. Here we briefly review results of previous studies on fluid flow in multilayer fibrous systems and discuss both destructive and non-destructive techniques used in those studies.

In textile engineering, some special concepts are used for quantifying fluid uptake of fibers or fibrous layers. Moisture content is defined as the ratio of mass of moisture to the mass of wet layer. Alternatively, the ratio of the moisture mass to the dry mass of material is known as regain.

1.3.1 Gravimetric measurements of wicking from layer to layer

The inter-layer space between two adjacent fibrous layers is a key parameter affecting the saturation threshold before water moves from a wet to a dry layer. Below this saturation threshold, no water transfer occurs between the layers. Among others, Adler and Walsh (1984) investigated the mechanisms of moisture transport between two layers of a woven fabric. A cotton or polyester fabric was soaked into one of the following three solutions: water, a salt solution, or a thickener solution. The fabric was subsequently allowed to dry until it reached a certain moisture regain. Afterwards, the sample was quickly wrapped and sealed for 10 minutes in order to give time for a uniform moisture distribution throughout the fabric to be reached. Next, a wet layer was placed underneath a dry layer of same material and the whole stack was sealed for a designated period of time (5, 10, 30, or 60 minutes). The stack was then unsealed and both samples weighted gravimetrically. Adler and Walsh (1984) presumed that both vapor diffusion and capillary wicking would occur when the working liquid was water while the thickener solution would be so viscous that vapor diffusion would be the prevailing mechanism when this solution was used. For experiments with a saline solution, the salt content of each sample was measured using a chloride electrode. Capillary liquid wicking would be determined by comparing water transport results with the salt solution transfer. For a cotton fabric, they found that moisture was transferred from a wet to dry layer due to vapor diffusion up to 30% above regain. But, capillary wicking accounted for 55% of moisture transported for 122%

above regain. This implies that 45% of moisture transfer occurred by vapor diffusion. Their analysis indicates that capillary wicking from bottom to top will not start until the sample wetness becomes 110% above regain. Gravity effects should be negligible in these types of experiments because of the thinness of the layers. Note that maximum moisture regain has not been reported in their research. Therefore, the degree of saturation (the ratio of moisture regain over its maximum value, or of fluid volume over total void volume) above which water passes through the interface and reaches the top dry layer is unclear. Assuming that a maximum moisture regain of 1200%, which we measured for raw cotton material, can be used for estimation of the saturation level here, a saturation threshold value of about 10% should be accumulated first in the bottom layer before water reaches the top dry layer. However, this is just an estimate in that the exact value for this critical threshold cannot be calculated with the current data. Adler and Walsh (1984) stated that the critical threshold of 110% moisture regain depends on the external pressure applied on the layers and their material. However, no external pressure was imposed on a stack of two identical layers in their study. For polyester, the above-mentioned threshold value is about 90% above regain. Based on their observations, Adler and Walsh concluded that wicking between two layers takes place only after a sufficient amount of water filled the capillaries between fibers and yarns.

Spencer-Smith (1977) performed similar tests by placing a dry linen drill fabric (made of cotton) on a wet one and applying 90 Pascal external pressures using a light glass plate. He found that the regain of a wet layer must exceed a critical threshold value of 80% before water transfer occurs between layers. Adler and Walsh (1984) stated that the critical threshold value found by Spencer-Smith (1977) was smaller than that of their experiment because of external pressure applied in his experiment.

To investigate the wicking mechanisms between fabric layers, Zhuang et al. (2002) studied the effects of external pressure exerted on a wet-dry bi-layer system. In one set of experiments, a wet woven fabric was placed on top of a dry fabric, which was mounted horizontally. A sand dish was placed on top of the stack to exert an external pressure on the layers. The external pressures were 45 Pa, 90 Pa, 135 Pa, 180 Pa, and 270 Pa. In each run, liquid transfer between layers was allowed for certain periods of time, after which the layers were gravimetrically

weighted. The tests were repeated from the same initial state but with different time periods in order to obtain at least six data point for each layer in half an hour. The experiments were performed with different initial levels of wetness, and also with different external pressures. Results of the experiments by Zhuang et al. (2002) using a fleece fabric showed the significance of external pressure on layer-layer fluid flow exchange. A higher external pressure led to early liquid transfer between the layers. Moreover, the experiments showed that a critical initial amount of water was needed for the transfer to initiate. This initial amount was lower when the external pressure was higher. Obviously, the external pressure alters the void space of the layers as such, as well as of the interface between the layers. Finally, since the woven layers, as used by Zhuang et al. (2002) in their study, had one side rough and the other side smooth, the way in which the layers contacted each other affected the liquid transfer process between the layers.

1.3.2 X-ray tomography measurements of wicking from layer to layer

One major uncertainty about all of the above-mentioned gravimetric measurement techniques is the amount of water that would drip out when layers are separated. This is due to the fact that liquid can be stored in the interlayer pore space. A second problem is that experiments could not be continued to find the time dependency of moisture transport in different time intervals, and thus had to be repeated several times. Thirdly, it was not possible to map liquid distributions along the thickness with gravimetric techniques. Alternatively, non-destructive techniques could be used to not disturb the assembly of layers during the experiments (Weder et al. 2006).

A non-destructive method for obtaining through-plane liquid distributions in multilayer configurations is X-ray tomography. This technique can provide a three-dimensional profile of the liquid distribution of a multilayer system at distinct time intervals. One can then also observe temporal evolutions of liquid ingress without manipulating the sample, based on X-ray tomography images (Weder et al. 2006).

1.3.2.1 Experiments by Weder et al (2006)

Weder et al. (2006) used X-ray tomography techniques to study moisture transport dynamics in multilayered fabric systems. They used a μ CT scanner to obtain detailed information on moisture transport in five different textile combinations,

each consisting of 4 textile layers. Each sample was up to 74 mm in diameter and had a maximum total thickness of 6.5 mm. The layers were scanned with a spatial resolution of 74 μm and a temporal resolution of 6.5 minutes. They explained that a higher spatial resolution (37 μm) can be reached at the expense of a lower temporal resolution. The contrast agent used in their working liquid gave a higher signal for wet than for dry samples. Accordingly, the amount of absorbed water per layer could be calculated based on a signal intensity threshold analysis. They investigated the role of hydrophilicity or hydrophobicity of the layers on the water content of each layer as well as on its distribution over the thickness of sample. For this purpose, water was supplied from the bottom of the stack at a flow rate of 9.4 ml/hour for about 36 minutes. A sample holder was designed in a way to exert a mild pressure of 160 Pascal to reduce the effects of swelling and repositioning of the layers during the experiment. Since water was injected from below, it filled the space between the bottom layer (layer 1) and the sample support. The temperature of the sample support was increased to 35 degrees in order to evaluate the effect of body temperature and evaporation on different layering systems.

The first combination of textile layers consisted of hydrophobic-hydrophilic-hydrophobic-membrane layers positioned from bottom to top, with a total thickness of 4.7 mm. Results of the through-plane water distribution for this combination were extracted from images at the end of experiment (after 36 minutes). The moisture distribution across the thickness was quantified based on 60 slices of μCT images. Final results are shown in Figure 1.1 (from Weder et al. 2006) indicate no liquid reached the top membrane (the first ten data points in the figure). The moisture distribution in the three layers was bell-shaped. The largest water content was reached in the second layer from the bottom, which was hydrophilic. Since layers were not perfectly flat in the planar direction, and swelling could change their thickness as well, the exact boundary between the layers cannot be identified. However, layer-averaged moisture contents can be calculated considering the thickness of each layer based on two mass minima, which was checked against dry thickness of each layer. Integration of each Gaussian curve between those two minima gave total moisture content of a layer.

Based on image analysis of water movement into the first combination of layers over time, Weder et al. (2006) found that the bottom layer exhibited very weak in-plane wicking because of its hydrophobic character. Water was transported to the

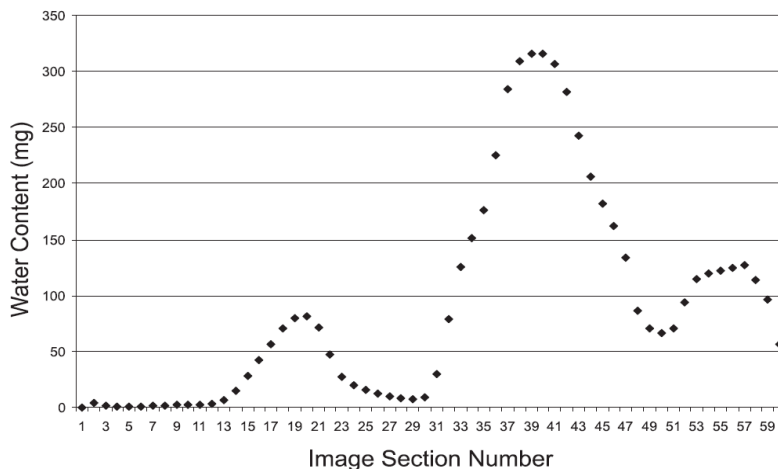


Figure 1.1 Water content variation over 4.7 mm thickness of stack of four layers (from Weder et al., 2006).

second layer rapidly because of its hydrophilicity. Additionally, large amounts of water were collected in this layer because the third layer was hydrophobic. Furthermore, water was distributed horizontally more evenly in the second layer rather than its two adjacent layers.

Details of water content variations over the thickness also revealed low water contents of the interlayer spaces. The very low contents between two layers corresponded to the interface region. For example, the interface region between the lower hydrophobic layer and upper hydrophilic layer was located between data points 49 to 51 in Figure 1.1. The lower water contents observed there indicate that larger pores are present in the interlayer pore space region compared to the middle part of each layer. For thin layers with a few pores along their thickness, one can expect a large impact of the space between two adjacent layers on the dynamics of fluid flow. Challenges about the characterization and modeling of such thin layers and their interfaces are discussed in more detail in Chapter 5. Of course, observing interface effects on the dynamics of fluid flow requires different sets of experiments and using techniques with higher spatial and temporal resolution.

In the study of Weder et al. (2006), layer-averaged water contents obtained from image analysis were validated by comparing to gravimetric tests. Good agreement was reached between x-ray results and corresponding gravimetric data. Final results of fluid flow for different combinations of textiles used in their study

demonstrate the role of hydrophilicity on liquid distribution and penetration in a stack of layers.

1.3.2.2 Experiments by Birrfelder et al. (2013)

Birrfelder et al. (2013) examined the effect of fabric structure on both in-plane and trans-planar wicking in a stack of two knitted polyester layers by X-ray tomography. They conducted experiments with two identical layers of the same material exposed to different external pressures. Different sets of layers with different knit structures and hydraulic properties were tested in their work. Table 1.1 gives a list of hydrophilic layers used in the Birrfelder et al. (2013) study. Round samples, with diameters of 65mm, were placed in a sample holder. Three different external pressures (0.2, 2 and 5 kPa) were applied to the top of the samples. Water was injected at a rate of 0.45 ml/min to the bottom surface of the sample using a nozzle. Volumetric water contents were measured by analyzing projection images with a spatial resolution of 74 μm , which were recorded every 4.5 seconds for a total time of 910 seconds. Birrfelder et al. (2013) concluded that there was a high correlation between in-plane wicking and hydrophilicity of the material, showing that in-plane wicking was faster in the more hydrophilic knit structure samples. For semi-hydrophobic materials, however, the supplied water could not be transported rapidly in the in-plane direction and stayed around the nozzle. This led to faster trans-planar wicking of the semi-hydrophobic samples. Water in these samples reached the upper layer without time delay. However, larger time delays of layer-to-layer mass transfer was observed for the hydrophilic layers. The time lag in water transfer from a lower hydrophilic layer to its identical upper one correlated with saturation build up in the bottom layer. Time delays could be shortened by applying larger external pressure, which is believed to have caused a decrease of the inter-layer void space and more contact between two layers.

Birrfelder et al. (2013) performed similar experiments (i.e. wicking into a stack of two identical layers) with four different hydrophilic materials, whose properties are reported in Table 1.1. Figure 1.2a shows the influence of knit structure on the time delays of the materials listed in Table 1.1. On top of each bar, the interfacial void area is given, which was determined from an optical micrograph and is presented in percentages. Surprisingly, layer-to-layer wicking delays were negatively correlated with larger void areas between the layers. One may expect

Chapter 1

Table 1.1 Properties of hydrophilic knitted fabrics used in study of Birrfelder et al. (2013)

#Code	Porosity [-]	construction	Thickness [mm] at 0.2 kPa	Thickness [mm] at 5 kPa	Contact angle [degrees]
I-68	0.87	Interlock	1.08	0.98	79±3
R-68	0.86	Rib	1.06	0.84	66±4
Im-68	0.88	Interlock mod	1.31	1.09	66±4
E-68	0.89	Eyelet	1.51	1.26	65±1

longer time delays with a larger interfacial void area (accordingly a smaller interlayer contact), but the opposite was observed in their experiments with different materials. Birrfelder et al. (2013) stated that this might be due to the fact that faster conducting pathways can be created inside the layer in the through-plane direction for R-68 and E-68, which had larger interfacial void areas. However, they found that time delays were consistently lower at higher external overburden pressures for all stacks (Figure 1.2b). As can be seen in Figure 1.2b, the average time delays of all four structures decreased exponentially by imposing higher external pressures because of decreasing interfacial void volume and increasing contact points. As a result, the time delay in mass exchange between two adjacent layers does not depend only on their interfacial geometrical

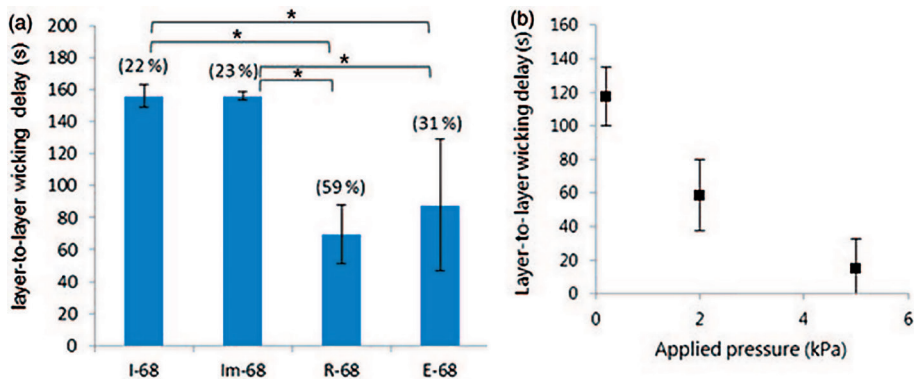


Figure 1.2 a) Layer to layer wicking delays for four different knit structures (shown in Table 1.1.) at 0.2kPa. Error bars are based on three replicate measurements. Percentage of interfacial void areas are shown in parenthesis b) Effect of external pressure on time delays averaged over all four hydrophilic structures (from Birrfelder et al., 2013).

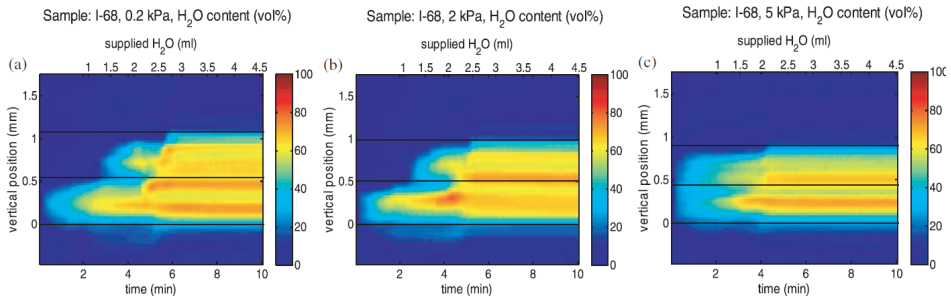


Figure 1.3 Variation of saturation across the thickness of two identical layers as a function of time. Results for three external pressures: a) 0.2kPa b) 2kPa c) 5kPa (from Birrfelder et al. 2013).

properties but also on the hydraulic properties of the layer which is filled first and its break-through time.

Figure 1.3 (from Birrfelder et al., 2013) gives more indication of how interfacial properties can change fluid flow dynamics when imbibition occurs in a stack of two identical layers exposed to different external pressures. The wicking behavior of two interlocked hydrophilic layers depicted in this figure shows that earlier wetting of the upper layer occurs when a 5 kPa external pressure is applied. This is most probably because of a smaller interlayer gap. Of course, external pressure affects layer properties itself as well. Therefore, all physical effects behind layer-layer wicking transfer should be combined to define a local critical saturation or volumetric water content threshold. Accordingly, liquid only moves from a layer to its neighboring layer if volumetric water content is higher than a certain threshold value. For instance, based on experimental observations of I-68 exposed to an external pressure of 0.2 kPa, shown in Figure 1.3, the average critical volumetric water content threshold was above 40% globally. Hence, the local threshold value must be more than 40%. In order to determine local threshold, results of in-plane water distributions in the lower layer are plotted as volumetric water content against radial position in Figure 1.4 (from Birrfelder et. al, 2013). Local volumetric water contents at breakthrough time (around 3 minutes) were between 60% to 80% for the case of a 0.2 kPa external pressure. The range of volumetric water contents for 2kPa was estimated to be between 40% to 60% (Figure 1.4b). Obviously, smaller interlayer gaps due to increasing external pressure would result in lower local thresholds. However, as can be seen in Figure

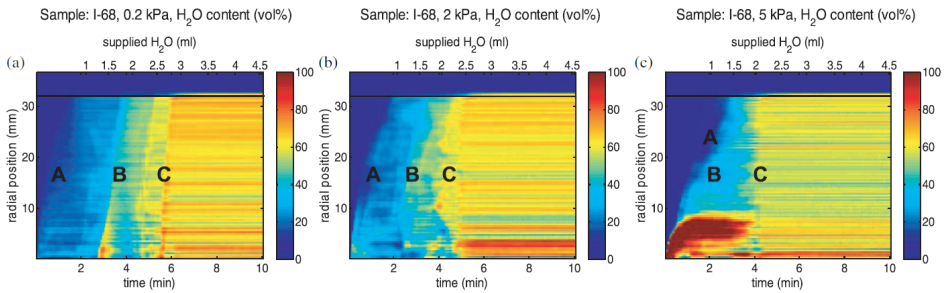


Figure 1.4 The in-plane water distribution in stack of two I68 at different external pressures a)0.2kPa b)2kPa c)5kPa. A, B and C indicate three distinct waterfronts: intra-yarn fronts of the lower layer (A), and the upper layer (B), and inter-yarn wicking fronts (C). Radial position: 0mm indicates the center of the sample (position of the sweating nozzle) and 32mm the edge of sample (from Birrfelder et al., 2013).

1.4c, the water content already reached 100% at a 5 kPa pressure at the very beginning; so the exact threshold value is uncertain. Consequently, water in the lower layer can only move to the upper one if and only if the volumetric water content will exceed the local threshold.

As a conclusion, one can state that water transfer from a layer to its adjacent layer is controlled by the hydraulic properties of the layers, the saturation builds up in the first layer, and the interlayer pore-space. Experiments demonstrated that water transfer time delay may be noticeable when two identical hydrophilic layers are placed on top of each other.

1.3.3 Continuum-scale modeling of a stack of thin fibrous layers and their interfaces

The effect of interlayer pore space on unsaturated fluid flow in stacked thin fibrous layers has not received enough attention in previous continuum-scale modeling studies (Hizir et al. 2010). Prat and Agaësse (2015) proposed the concept of modeling interlayer space as a virtual third layer, acting as a transition region between two adjacent layers. However, determining the hydraulic properties of a virtual third layer introduces additional complexity. Not only will the REV concept not hold for such an interface; the virtual third layer thickness itself can only be a vague entity. Another modeling approach in which the interface effects are described by means of terms for the exchange of mass, momentum and energy, referred to as Reduced Continua Model, has been developed recently (Qin and

Hassanizadeh 2014; Qin and Hassanizadeh 2015). Still many questions regarding determination of the mass exchange term remain, which will be addressed in this dissertation.

In this research, a comprehensive study of continuum-scale modeling of a stack of multilayer thin fabrics is presented. Reduced Continua Model is used for modeling multilayer thin system, which enabled us to take into account interlayer effect and saturation build up threshold. Results of this modeling approach are compared with traditional Darcy based models and experimental data.

References

- Adler, M. M., and Walsh, W. K: Mechanisms of Transient Moisture Transport between Fabrics, *Textile Research Journal*. 54, 334–343 (1984)
- Ashari, A., Tafreshi, H.V.: A two-scale modeling of motion-induced fluid release from thin fibrous porous media. *Chem. Eng. Sci.* 64, 2067–2075 (2009)
- Birrfelder, P., et al.: Effect of fiber count and knit structure on intra- and inter-yarn transport of liquid water. *Textile Research Journal*. 83(14), 1477–1488 (2013)
- Brooks, R. H., Corey, A. T.: Hydraulic properties of porous media. Hydrology Paper No. 3. Colorado State Univ. Fort Collins, Colorado, 27 pp. (1964)
- Davies, C.N.: Air Filtration. Academic Press, London (1973)
- Fairweather, J. D., Cheung, P., St-Pierre, J., and Schwartz, D. T.: A Microfluidic Approach for Measuring Capillary Pressure in PEMFC Gas Diffusion Layers. *Electrochemistry Communications*. 9(9), 2340-2345 (2007)
- Gostick, J.T., Fowler, M. W., Ioannidis, M.A., Pritzker, M. D., Volfkovich, Y.M., Sakars, A.: Capillary pressure and hydrophilic porosity in gas diffusion layers for polymer electrolyte fuel cells. *J. Power Sources* 156, 375–387 (2006)
- Gostick, J.T., Ioannidis, M.A., Fowler, M. W., Pritzker, M. D.: Direct measurement of the capillary pressure characteristics of water-air-gas diffusion layer systems for PEM fuel cells. *Electrochemistry Communications* 10, 1520-1523 (2008)
- Hizir, F. E., S. O. Ural, E. C. Kumbur, and M. M. Mench: Characterization of interfacial morphology in polymer electrolyte fuel cells: Micro-porous layer and catalyst layer surfaces, *Journal of Power Sources*, 195(11), 3463–3471 (2010)
- Hussaini, I.S., Wang, C.Y.: Measurement of relative permeability of fuel cell diffusion media. *J Power Sources*. 195, 3830-3840 (2010)
- Jackson, G. W., James, D. G.: The permeability of fibrous porous media. *Can. J. Chem. Eng.* 64, 362-374 (1986)
- Jaganathan, S., Vahedi Tafreshi, H., Pourdeyhimi, B.: A realistic modeling of fluid

Chapter 1

- infiltration in thin fibrous sheets. *J. Appl. Phys.* 105, 113522 (2009)
- Jena, A., Gupta, K.: Characterization of Pore Structure of Fuel Cell Components Containing Hydrophobic and Hydrophilic Pores. 41st Power Sources Conference (2005)
- Kaviany, M.: Principles of Heat Transfer in Porous Media, Mechanical Engineering Series, Springer-Verlag New York, Inc., New York. (1995)
- Kumbur, E. C., Sharp, K. V., and Mench, M. M.: Validated Leverett Approach for Multiphase Flow in PEFC Diffusion Media, I. Hydrophobicity Effect. *Journal of the Electrochemical Society*. 154(12), B1295-B1304 (2007a)
- Kumbur, E. C., Sharp, K. V., and Mench, M. M.: Validated Leverett Approach for Multiphase Flow in PEFC Diffusion Media, II. Compression Effect. *Journal of the Electrochemical Society*. 154(12), B1305-B1314 (2007b)
- Landeryou, M., Eames, I., Cottenden, A.: Infiltration into inclined fibrous sheets. *Journal of Fluid Mechanics*. 529, 173–193 (2005)
- Leisen, J., Beckham, H.W.: Fluid Distribution and Movement in Engineered Fibrous Substrates by Magnetic Resonance Microscopy Magnetic Resonance Microscopy: Spatially Resolved NMR Techniques and Applications. 399-419 (2009)
- Mathias, M., Roth, J., Fleming, J., and Lehnert, W.: Handbook of Fuel Cells: Volume 3 - Fuel Cell Technology and Applications, John Wiley & Sons, Ltd, New York, Chapter 46 - Diffusion Media Materials and Characterisations (2003)
- Miller, B., Tyomkin, I.: Liquid porosimetry: new methodology and applications. *J Col Int Sci*. 62,163-170 (1994)
- Mohebbi, B., Tavangarrad, A.H., Clausen, J., Blümich, B., Hassanizadeh, S. M., Rosati, R.: Revealing how interfaces in stacked thin fibrous layers affect liquid ingress and transport properties by single-sided NMR. *Journal of Magnetic Resonance* (2018)
- Nguyen, T. V., Guangyu, L., Heebong, O., Dan, H., David, J., and Muhammad, A.: Measurements of Two-Phase Flow Properties of the Porous Media Used in PEM Fuel Cells. *ECS Transactions*. 3(1), 415-423 (2006)
- Nguyen, T.V., Lin, G., Ohn, H., Wang, X.: Measurement of capillary pressure property of gas diffusion media used in proton exchange membrane fuel cells. *Electrochem. Solid-State Lett* 11, B127–B131 (2008)
- Prat, M., Agaësse, T.: Thin porous media. In: Vafai, K. (ed.) *Handbook of Porous Media* (Chapter 4), 3rd edn. Taylor & Francis, London (2015)
- Qin, C. Z. and Hassanizadeh, S. M.: Multiphase flow through multilayers of thin porous media: General balance equations and constitutive relationships for a solid-gas-liquid three-phase system. *Int. J. Heat Mass Transf.* 70, 693–708 (2014)
- Qin, C. Z., Hassanizadeh, S.M.: A new approach to modelling water flooding in a polymer electrolyte fuel cell. *International journal of hydrogen energy*. 40, 3348-3358 (2015)
- Sole, J.D.: Investigation of water transport parameters and processes in the gas

- diffusion layer of PEM fuel cells. PhD dissertation, Virginia Polytechnic Institute and State University (2008)
- Spencer-Smith, J. L.: The Physical Basis of Clothing Comfort, Part 4: The passage of heat and water through dan-clothing assemblies. *Cloth. Res. J.*, 5, 116 (1977)
- Spielman, L., and Goren, S. L.: Model for predicting pressure drop and filtration efficiency in fibrous media. *Environ. Sci. Technol.* 2, 279-287 (1968)
- Tavangarrad, A.H., Mohebbi, B., Hassanizadeh, S. M., Rosati, R., Clausen, J., Blümich, B.: Continuum-scale modeling of liquid redistribution in a stack of thin hydrophilic fibrous layers. *Transport in Porous Media.* 122, 203-219 (2018)
- Tomadakis, M.M., Robertson, T.J.: Viscous permeability of random fiber structures: Comparison of electrical and diffusional estimates with experimental and analytical results. *J. Compos. Mater.* 39, 163–188 (2005)
- Van Genuchten, M. Th.: A closed-form equation for predicting the hydraulic conductivity of unsaturated soils. *Soil Sci Soc. Am J.* 44, 892-898 (1980)
- Weder, M., Bruhwiler, P.A., Laib, A.: X-ray tomography measurements of the moisture distribution in multilayered clothing systems. *Textile research journal.* 76, 18–26 (2006)
- Zhuang, Q., Harlock, S.C., Brook, B.D.: Transfer Wicking Mechanisms of Knitted Fabrics Used as Undergarments for Outdoor Activities. *Textile. Research. Journal.* 72, No. 8, 727–734 (2002)

Chapter 2

Measurements of capillary pressure-saturation curves of thin hydrophilic fibrous layers; effects of overburden pressure, number of layers, and multiple imbibition-drainage cycles

Submitted as: Tavangarrad, A.H., Hassanizadeh, S.M., Rosati, R., Digirolamo, L., van Genuchten, M.Th.: Measurements of capillary pressure-saturation curves of thin hydrophilic fibrous layers. *Textile Research Journal* (2018).

Abstract

Unsaturated fluid flow in thin porous media depends on hydraulic properties such as the capillary pressure, P_c , as a function of saturation, S . We measured this relationship for two different types of deformable thin hydrophilic fibrous layers under varying conditions. Among other factors, we changed the number of layers and the overburden pressure imposed on one layer or a stack of layers. Applying an overburden pressure drastically affected the $P_c(S)$ curves. However, increasing the number of fibrous layers had little impact on the capillary pressure-saturation curves. We also investigated the effect of multiple imbibition-drainage cycles on the $P_c(S)$ data. Measured data points were used to find general expressions for the $P_c(S)$ relationships of deformable thin porous media. Existing quasi-empirical correlations used in vadose zone hydrology, notably expressions by van Genuchten (1980) and Durner (1994) for single- and dual-porosity media, respectively, were employed to fit the measured data points.

2.1 Introduction

Thin non-woven fabrics have many applications, such as for use in hygiene products, filters, and fuel cells (Albrecht et al. 2003; Prat and Agaësse 2015). Hydraulic characteristics of a thin fibrous layer have great impact on the performance of fibrous products. Knowledge of hydraulic properties of thin fabrics is hence essential for optimizing the performance of these products. Unfortunately, there are several challenges when measuring the unsaturated hydraulic properties of such thin layers. A layer is considered physically thin when the number of pores along its thickness is less than approximately 15 (Qin and Hassanizadeh 2014; Qin and Hassanizadeh 2015; Ceballos et al. 2011; Tavangarrad et al. 2018), with the thickness of a thin porous layer obviously being much smaller than in its planar extent.

A number of studies focusing on measurements of capillary pressure-saturation relationships of thin non-woven fabrics are reported in the literature. Several concern $P_c(S)$ curves of water-air system in the gas diffusion layer (GDL) of polymer electrolyte fuel cells (PEFC) (see e.g., Sole 2008; Gostick et al. 2006; Gostick et al. 2008; Nguyen et al. 2006; Kumbur et al. 2007a; Fairweather et al. 2007; Jena and Gupta 2005; Nguyen et al. 2008). A comprehensive review of available techniques employed for GDLs is reported in a study by Sole et.al (2008). Some measurements have been carried out also to determine the $P_c(S)$ relationships of thin hydrophilic fabrics used in medical and hygienic absorbent products (Landeryou et al. 2005; Jaganathan et al. 2009a; Tavangarrad et al. 2018).

Several modeling studies also exist to estimate the capillary pressure saturation curves of thin fibrous layers. For example, in a recent study, general expressions for the $P_c(S)$ relationship of thin fabrics were developed for a family of fibrous media using a pore morphology methodology (Ashari and Tafreshi 2009). That work, however, was based on virtual non-woven fibrous materials. Pore morphology modeling has been used also to determine the $P_c(S)$ relationship of uncoated thin paper (Aslannejad and Hassanizadeh 2017).

A few studies can be found in the literature on changes in the $P_c(S)$ curves of thin fabrics due to the effect of an overburden pressure. In an experimental study by Kumbur et.al (2007b), the effect of compression on the drainage capillary pressure-saturation curve of thin fibrous layers with mixed wettability was

investigated. Another study concerned image analysis of compression-induced morphological changes of non-woven fibrous materials (Jaganathan et al. 2009). Furthermore, Jena and Gupta (1999) investigated the influence of overburden effects on the pore structure of battery separators made of non-woven fibrous layers. These various studies, however, focused on changes in the pore size distribution rather than capillary-pressure saturation curves.

To the best of our knowledge, the effects of overburden pressure, the occurrence of multiple imbibition-drainage cycles and number of layers on imbibition-drainage $P_c(S)$ relationships of thin hydrophilic non-woven fabrics have not been studied experimentally thus far. These different effects are encountered in many practical applications. Examples are hygienic products such as diapers, in which the weight of a baby imposes compression on the stack of thin fibrous layers. The compression effect is also a key factor in the optimization of fuel cell stack assemblies. Multiple imbibition-drainage cycles occur in many products such as diapers, adult incontinence products and absorption pads. The number of imbibition-drainage cycles is then different depending upon the volume of liquid in each gush and the maximum available pore volume for fluid storage.

For this study we used an autoporosimetry technique developed by Miller and Tomkin (1994) to characterize thin hydrophilic non-woven fabrics. Our objective was to evaluate the effects of three main factors on the capillary pressure-saturation relationship of thin hydrophilic non-woven fabrics: number of layers, overburden pressure, and number of imbibition-drainage cycles. Measurements were performed on thin layers made of two different synthetic polymers. A comprehensive study was carried out to determine the $P_c(S)$ curves of compressed and uncompressed thin fabrics. The individual data points were fitted with relationships proposed by van Genuchten (1980) and Durner (1994) for single- and dual-porosity media, respectively. We also investigated the effects of overburden pressure on porosity and permeability changes of the thin layers.

The remainder of this paper is organized as follows. In Section 2, the experimental setup and procedure are briefly described. In Subsection 3.1, the influence of overburden pressure on the $P_c(S)$ relationship is explained, and the fitting functions are introduced. In Subsection 3.2, the influence of number of layers on the capillary pressure-saturation measurement is discussed, while in Subsection 3.3, results of multiple $P_c(S)$ imbibition-drainage cycles are presented. Results of our

study on another type of non-woven fabric are given in Subsection 3.4. Finally, scaling $P_c(S)$ curves using Leverett J-function are described in Section 4, followed by conclusions in Section 5.

2.2 Methods and materials

2.2.1 Materials

Two different non-woven fabrics were used in this study: polyolefin fabric and polyethylene terephthalate (PET) fabric. The layers were made of polyolefin fabric thermally bonded in some regions during the production process. They were also treated with a surfactant to make them hydrophilic. Each polyolefin layer was about 260 μm thick with a porosity of approximately 90%. The PET fabric was made of hollow fibers. The PET layer was about 1500 μm thick with a porosity of close to 97%. Other properties of the materials, including fiber radius and density values, are given in Table 2.1.

A saline solution, made of 0.9% NaCl (by weight) and distilled water, was chosen as the working liquid. The solution had a surface tension of 72.5 mN/m, a density of 1.005 g/cm³, and a viscosity of 1.019 mPa.s. Both fibrous materials exhibited negligible swelling in such a solution (Albrecht et al. 2003).

2.2.2 Experimental setup

The setup used in this study to measure capillary pressure and saturation is referred to as a PVD-Autoporosimeter (Pore Volume Distribution Autoporosimeter) as developed by Miller (1994). A schematic of the setup is shown in Figure 2.1. The PVD-Autoporosimeter consisted of two parts: a chamber containing the fabric sample and a solution reservoir. The sample chamber consisted of a glass frit, a

Table 2.1 Properties of the two fibrous layers used in this study

Properties	Unit	Polyolefin	PET
Fiber radius	[μm]	10	16
Fiber density	[g/cm ³]	0.92	1.35
Porosity (Compressed)	[-]	0.84	0.93
Porosity (Uncompressed)	[-]	0.90	0.97
Permeability (Compressed)	[m ²]	8.29×10^{-11}	1.46×10^{-9}
Permeability (Uncompressed)	[m ²]	2.05×10^{-10}	5.10×10^{-9}

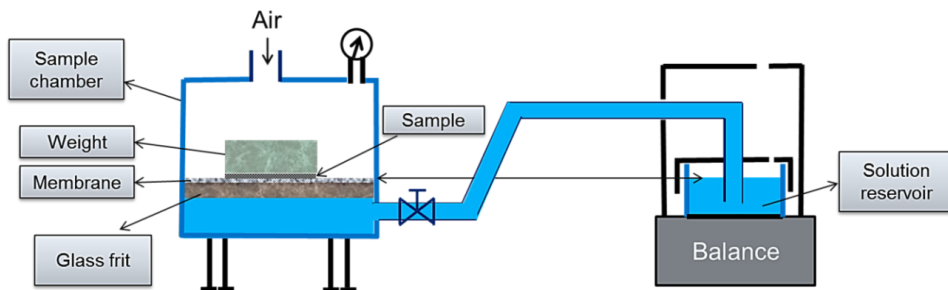


Figure 2.1 Schematic view of the PVD-Autoporosimeter.

membrane, a tube to connect the chamber to the reservoir, an electronic balance, and an automatic system to control the pressure and temperature of air in the headspace. The membrane covered the glass frit, while the circular sample with a diameter of 50 mm was placed on the membrane. A weight could be placed on the sample to provide compression loading. The solution reservoir was placed on a high-precision balance. The reservoir was covered by a lid to minimize evaporation, while still being connected to atmospheric air. The water level in the reservoir was set equal to the same elevation as the top of the membrane. Changes in the water level due to drainage or imbibition of the sample could be considered negligible since the lateral surface area was relatively large.

2.2.3 Experimental procedure

The PVD-Autoporosimeter was used to obtain capillary pressure-saturation curves based on quasi-static multistep inflow-outflow measurements. Capillary pressures were varied by increasing or decreasing the air pressure during drainage and imbibition, respectively. Water pressures in the sample were assumed to remain equal to atmospheric pressure at equilibrium since they were at the same level as the level of the solution reservoir. Air pressure steps were specified in the PVD-Autoporosimeter software and fed into automatic controller which could change the air pressure in the chamber. Fluid saturation values of the sample were measured gravimetrically using the balance. At each step, the air pressure was kept constant until equilibrium was reached and capillary flow had ceased. A few hours were needed to perform a full imbibition-drainage cycle. We note that a slight loss of weight of the solution reservoir was still recorded due to evaporation, which could not be neglected completely despite the reservoir being covered by a lid. The evaporation rate was determined from mass loss of the reservoir as measured for 26

an extended period of time. During measurement of the $P_c(S)$ curves, we assumed that equilibrium was reached when the reservoir mass loss rate became less than some small threshold value. The experimental results were corrected by taking the measured evaporation rate into an account. More information about the equilibrium threshold is given in Appendix B.

The glass frit and membrane were kept fully saturated at all times. Sometimes during imbibition a few droplets of water formed on the membrane surface, but disappeared during drainage. Also, a very small volume of water ($\cong 200\mu\text{l}$) could accumulate around the edge of the membrane at the bottom due to capillary rise against the wall of the chamber in the form of a corner triangle. Such effects are negligible for $P_c(S)$ measurements of large porous samples (such as soil samples). However, because of the very small pore volumes involved, they cannot be neglected in the case of thin layers. In order to reduce this effect, we modified the setup. This reduced the capillary rise volume to about $40\mu\text{l}$. Therefore, in order to reduce uncertainty and measurement error, the corresponding volume of water was quantified in blank measurements (without any sample) at various air pressures. The mass loss or gain of the reservoir during $P_c(S)$ measurements of the layers was corrected using this blank volume. More details about this correction are provided in Appendix A.

2.2.4 Fitting of data points

Equations commonly used for describing observed of capillary pressure-saturation data are those proposed by van Genuchten (VG) (1980), Brooks and Corey (BC) (1964) and Durner (1994), among others. The VG formula is given by:

$$S_e(h) = \frac{1}{(1 + |\alpha h|^n)^m} \quad (2.1)$$

where h is the capillary pressure head, α and n are fitting parameters, $m = 1 - 1/n$, and S_e is effective saturation given by $S_e = (S - S_{\text{ir}})/(1 - S_{\text{ir}})$, in which S is the degree of fluid saturation and S_{ir} is irreducible saturation. Because of the very large porosity of our samples, no residual air saturation needed to be considered. In physical terms, α corresponds approximately to the inverse of non-wetting phase entry pressure, while the value of n reflects the pore-size distribution. Another formula is the Brooks and Corey (BC) equation (1964):

$$S_e(h) = \left(\frac{h}{h_e}\right)^{-\lambda}; \text{ for } h > h_e \quad (2.2)$$

where h_e is the air entry pressure head, while λ is often referred to as pore size distribution index. For more complex cases, the Durner bimodal function, which is constructed by linear superposition of VG sub-curves, may be needed:

$$S_e(h) = \frac{w_f}{(1 + |\alpha_f h|^{n_f})^{m_f}} + \frac{w_m}{(1 + |\alpha_m h|^{n_m})^{m_m}} \quad (2.3)$$

where $\alpha_f, n_f, \alpha_m, n_m$ are fitting parameters, w_f and w_m are weights of the overlapping regions (subject to $w_f + w_m = 1$), $m_f = 1 - 1/n_f$, and $m_m = 1 - 1/n_m$. The above equations may be used for woven or non-woven fabrics under both compressed and uncompressed conditions. The VG and BC equations are appropriate for unimodal $P_c(S)$ curves, while Durner's equation (and extensions thereof) can be applied to bimodal (and multi modal) curves. For instance, Gostick et.al (2006) only used unimodal VG- and BC-based $P_c(S)$ curves for their thin fibrous GDLs. Bimodal models such as Durner's equation should provide better descriptions of some of their $P_c(S)$ data sets.

2.3 Results

2.3.1 Influence of overburden pressure

To study the effect of overburden pressure on capillary pressure-saturation curves, the $P_c(S)$ curves of a single polyolefin layer were measured with and without placing a metal weight on top of the sample. We also studied the effect of compression on the porosity of the fabric. When putting a 0.3 psi metal weight on top of the polyolefin fabric, the porosity was reduced from 0.9 to 0.84. The measured imbibition and drainage curves with and without compression were both found to be significantly different also, as shown in Figure 2.2. The error bars in this figure are based on duplicate measurements. Higher capillarity was observed with the overburden pressure as compared to the uncompressed layer. This is because the mean pore size becomes smaller when the fabric carries a metal weight. Jaganathan et al. (2009b) observed similar effects on the mean pore size

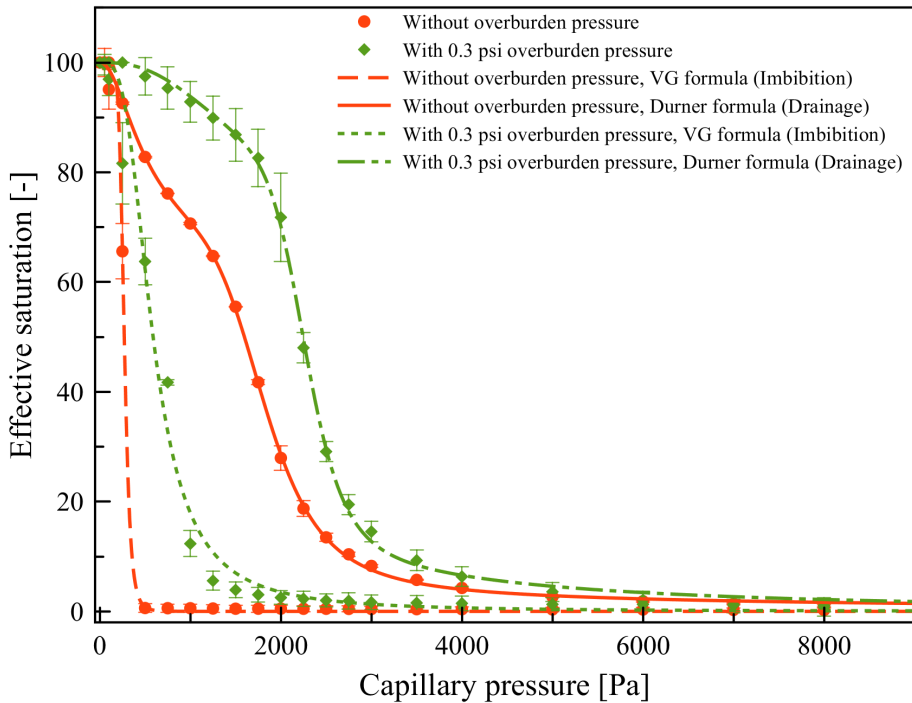


Figure 2.2 Measured capillary pressure-saturation data for a single polyolefin layer with and without overburden pressure. Lines show curves fitted to the data using van Genuchten (VG) and Durner formulas.

of a hydroentangled non-woven fabric when exposed to an overburden pressure, based on DVI image analyses. We also observed a milder slope of the $P_c(S)$ curve during drainage of the uncompressed layer compared to the compressed sample.

Parameters of the fitted imbibition and drainage curves shown in Figure 2.2 are listed in Table 2.2. The VG formula was found to fit imbibition data points satisfactorily. However, Durner's formula could fit drainage data for both compressed and uncompressed layers much better. The higher value of α for the imbibition curve of the uncompressed layer, compared to the compressed layer, showed that the air entry pressure was lower for uncompressed fabric. Similarly, corresponding α_f and α_m values of Durner's equation fitted to the drainage data of the uncompressed layer were larger than those of the compressed layer. A larger value of n_m in Durner's formula was obtained for the compressed layer, which

Table 2.2 Fitting parameters of imbibition (VG formula) and drainage (Durner formula) curves of compressed and uncompressed single polyolefin layer

	α [1/Pa]	n [-]	S_{ir} [-]	w_f, w_m [-]	α_f [1/Pa], α_m [1/Pa]	n_f, n_m [-]
Uncompressed	0.00378	8.53	0.02	0.42, 0.58	0.00260, 0.00056	2.07, 6.64
Compressed	0.00197	3.44	0.06	0.35, 0.65	0.00069, 0.00044	2.63, 11.80

indicates a sharper transition of saturation at larger capillary- pressures compared to the uncompressed layer within the same range.

2.3.2 Influence of number of layers

One fibrous layer, or stacks of two or five layers, of polyolefin were placed on top of the membrane in the sample chamber, and exposed to an overburden pressure of 0.3 psi (about 2 kPa). Capillary pressure-saturation data for the compressed stack were collected for both imbibition and drainage. The influence of increasing the number of polyolefin layers on the $P_c(S)$ curves is shown in Figure 2.3. The error bars in this figure are based on the standard deviation of two replicates of the same

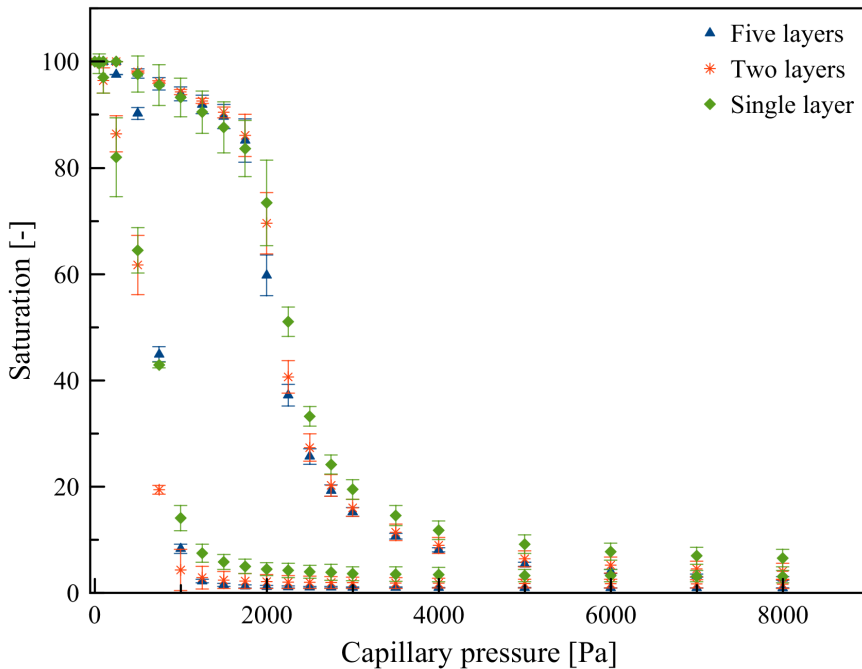


Figure 2.3 Capillary pressure-saturation data for different sets of polyolefin layers under 0.3 psi overburden pressure.

Table 2.3 VG Fitting parameters of the imbibition and drainage curves of compressed samples containing different numbers of polyolefin layers

Sample	Imbibition	Imbibition	Drainage	Drainage
	α [1/Pa]	n [-]	α [1/Pa]	n [-]
Single layer	0.00197	3.44	0.000469	6.29
Stack of two layers	0.00197	5.04	0.000475	7.16
Stack of five layers	0.00143	7.24	0.000488	6.62

experiment. Results indicate no significant difference between the drainage data for different stacks of layers. VG fitting parameters of the drainage curves, shown in Table 2.3, confirm the similarity of the various curves. Differences are within the effect of variability in the sample material itself. However, noticeable differences exist in the imbibition data for saturations above 10%: higher saturations at a given capillary pressure occur for the stack of five layers. These differences are also seen in the fitted parameter values, shown in Table 2.3.

A similar comparison was made between the $P_c(S)$ curves of a single polyolefin layer and stacks of multiple layers without overburden pressure. Results are shown in Figure 2.4. Slightly higher saturation values were obtained for a single layer as

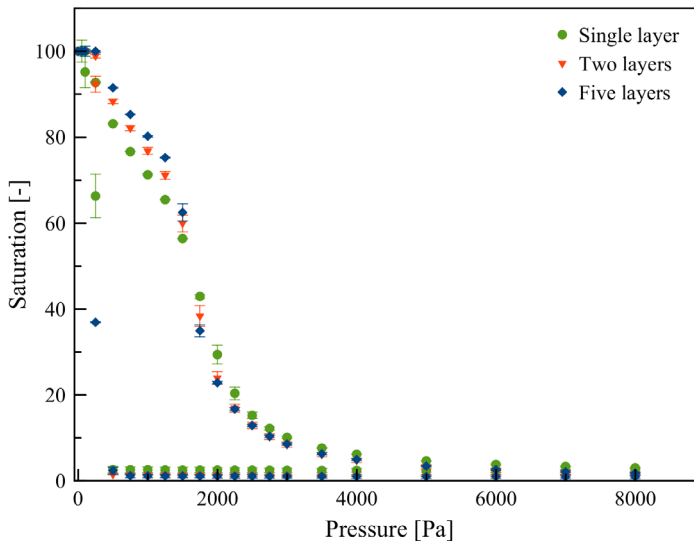


Figure 2.4 Capillary pressure-saturation data points for different number of polyolefin layers without applying overburden pressure.

compared to multiple layers for saturations from zero up to about 50% during drainage. Beyond this saturation, the trend reversed and the stacks of multiple layers had higher saturation values compared to a single layer. Nevertheless, differences between the measured curves are relatively minor. We conclude that the number of layers has little impact on measured capillary pressure-saturation data points, especially for uncompressed layers.

2.3.3 Influence of multiple imbibition-drainage cycles

We next investigated the effect of multiple imbibition-drainage cycles on the hydraulic properties of a single polyolefin layer, starting with a dry sample subject to an overburden pressure of 0.3 psi. Figure 2.5 shows results for two consecutive imbibition- drainage cycles. No significant difference is apparent for the drainage data, except for a clear shift in the imbibition data points towards higher saturation and capillary pressures.

The main reason for this effect is the fact that the dry polyolefin fibers have a low

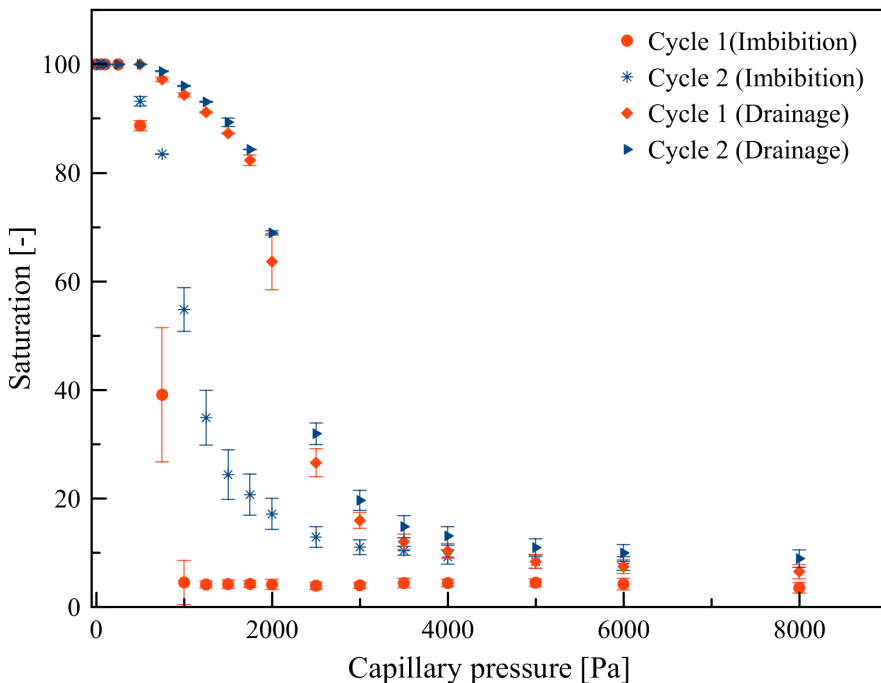


Figure 2.5 Effect of multiple imbibition-drainage cycles on capillary pressure-saturation measurements of a single polyolefin layer subject to overburden pressure.

surface energy and are receptive to being wetted by water. At the start of the second imbibition cycle, the fibers already contained some fluid (because of an irreducible saturation of around 6%). Surface energies as a result increased, leading to higher capillary pressures at given saturation levels.

2.3.4 Effect of layer material

The experiments thus far were carried out using polyolefin fabric. A similar series of experiments was performed on layers made of polyethylene terephthalate (PET). The PET layers are thicker than those made of polyolefin, but are much coarser and contain at most 10 pores along its thickness (Table 2.1). Fiber diameters and mean pore sizes of the PET layers, as well as their porosity, are larger than those of the polyolefin layer. Measured capillary pressure-saturation data for various sets of PET layers are presented in Figure 2.6. As expected, a lower capillarity for PET layer was observed during both imbibition and drainage (compare Figures 2.2 and 2.6). Values of the VG parameters obtained by fitting Eq. (1) to the data points are listed in Table 2.4. Clearly, values of α for the imbibition and drainage curves of the compressed PET layers were much larger than those of the polyolefin layer, as is shown also by the entries in Tables 2.2 and 2.3. Similarly, measured permeability and porosity of PET fabric are much higher.

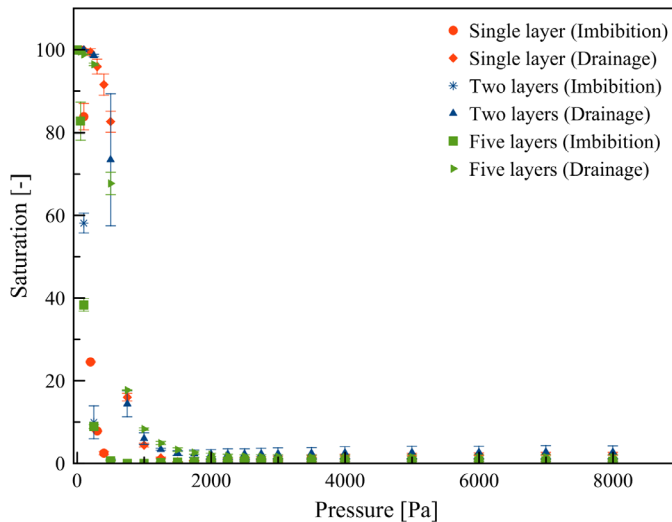


Figure 2.6 Capillary pressure-saturation of different number of PET layers under 0.3 psi overburden pressure.

Table 2.4 Hydraulic parameters of the imbibition and drainage curves of a single compressed PET layer used in this study

Sample	Imbibition	Imbibition	Drainage	Drainage	$S_{tr}[-]$
	$\alpha[1/Pa]$	$n[-]$	$\alpha[1/Pa]$	$n[-]$	
Compressed PET layer	0.073	4.32	0.001698	7.71	0.01

Results of the capillary pressure-saturation measurements of the stacks with different numbers of PET layers are depicted in Figure 2.6. The variability in the measurements can be attributed mainly to inherent differences in the fabrication of the fabric. The relatively small difference in the data for different numbers of layers shows that the effect of interlayer space is negligible. This is similar to results we obtained for the polyolefin stacks as shown in Figure 2.2.

Next, the effect of multiple imbibition-drainage cycles was studied on a single PET layer under compressed conditions. Results are shown in Figure 2.7. The data again do not show any differences between the second and third cycle for both imbibition and drainage. However, similarly as for the polyolefin experiments, the imbibition curves of second and third cycles exhibited higher capillary pressures compared to the first cycle. Finally, we studied the effect of overburden pressure

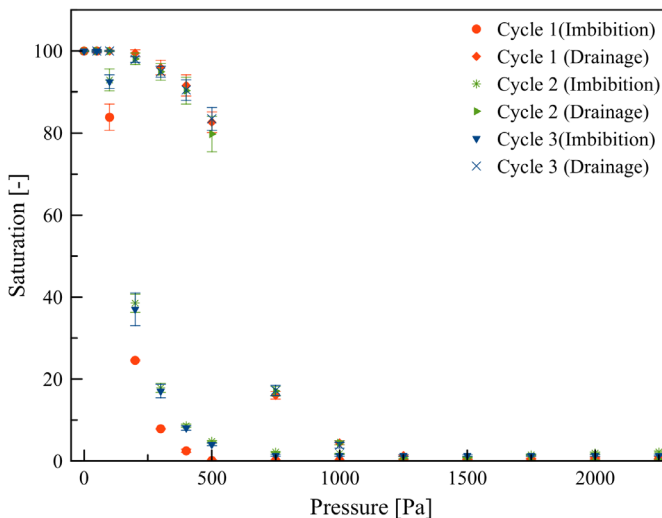
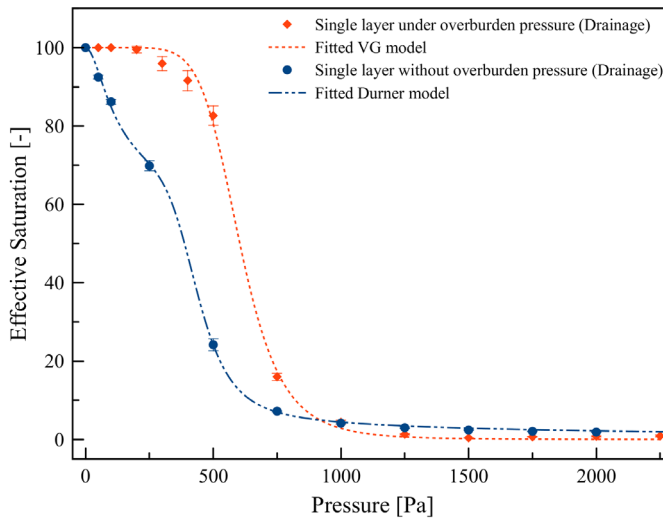


Figure 2.7 Effect of multiple imbibition/drainage cycles on capillary pressure-saturation measurements of a single PET layer.

Table 2.5 Fitting parameters of Durner drainage curve of an uncompressed single PET layer used in this study

Sample	$w_f, w_m[-]$	$\alpha_f[1/\text{Pa}], \alpha_m[1/\text{Pa}]$	$n_f, n_m[-]$	$S_{tr}[-]$
Uncompressed PET layer	0.43, 0.57	0.012, 0.0023	1.94, 7.38	0.02

on the $P_c(S)$ curves of a single PET layer. Figure 2.8 shows capillary pressure-saturation drainage curves with and without the overburden pressure (again 0.3 psi). Corresponding fitting parameters of the $P_c(S)$ drainage curves using the unimodal van Genuchten and bimodal Durner models are given in Tables 2.4 and 2.5, respectively. The PET results are very much in line with those of the polyolefin fabric as shown in Figure 2.3. Higher capillary pressures were obtained with the overburden pressure since the fabric then deforms and the pores become smaller.

**Figure 2.8** Observed (symbols) and fitted (lines) drainage capillary pressure-saturation curves of a single PET layer with and without overburden pressure.

2.4 Scaling of $P_c(s)$ curves using Leverett J-function

The purpose of employing Leverett J -function (Leverett 1941) is to use measured $P_c(S)$ curves for a given non-woven fibrous material in order to construct $P_c(S)$ curves for similar materials and/or for different conditions. The $P_c(S)$ equation as proposed by Leverett (1941) is of the form:

$$P_c(S) = \gamma \cos(\theta) \left(\frac{\varphi}{K}\right)^{\frac{1}{2}} J(S) \quad (2.4)$$

in which θ is the static contact angle of a fluid-solid system, φ is porosity, and γ is the interfacial tension between the wetting and non-wetting fluids. The function $J(S)$ depends on morphological properties of the porous medium and presumably is the same for similar media. Udell (1985) did propose an equation for $J(S)$ for highly hydrophilic geological porous media, which was used later also, for thin fibrous layers (Pasaogullari and Wang 2004):

$$J(s) = \begin{cases} 1.417(1 - S) - 2.12(1 - S)^2 + 1.263(1 - S)^3 & \text{for } \theta \leq 90 \\ 1.417S - 2.12S + 1.263S & \text{for } \theta > 90 \end{cases} \quad (2.5)$$

The generic Leveret approach given by the above equations was used to fit capillary pressure saturation curves of a compressed polyolefin layer. Assuming the interfacial tension between air and liquid to remain constant during the measurements, the only unknown parameter is the static contact angle. The best fit of the drainage data was obtained with a contact angle of 25 degrees, while the imbibition data points matched using a contact angle of 77 degrees. We thus used Equation (5) to predict the $P_c(S)$ data of an uncompressed non-woven fibrous material from a similar type of fabric based on equality of the J -function for the two fabrics as follows (Pinder and Gray 2008):

$$P_{c2}(S) = P_{c1}(S) \frac{\gamma_2}{\gamma_1} \left(\frac{K_1}{K_2}\right)^{\frac{1}{2}} \left(\frac{\varphi_2}{\varphi_1}\right)^{\frac{1}{2}} \quad (2.6)$$

where the subscripts 1 and 2 denote uncompressed and compressed layers, respectively. The contact angle was assumed to be same for both layers. It should be noted that a change in the contact angle is not the only reason for hysteresis in the capillary pressure-saturation curve. Differences occur also since small pores control drainage events while the larger pores regions control imbibition (Pinder and Gray 2008), often referred to as the ink bottle effect.

As explained in previous studies (see e.g., Kumber et al. 2007b), the equations above are insufficient for describing capillary flow phenomena. One should consider additional variables such as pore size distribution and stress-strain relationships to better scale the $P_c(S)$ curves under different compression loads. However, as illustrated in Figure 2.9, similar trends in Leveret's -J function, and

hence the $P_c(S)$ curves, were obtained due to the overburden pressure effect. The predicted curves could not reproduce the bimodal behavior of uncompressed layer under drainage condition. But, as shown by Figure 2.9, changes in the $P_c(S)$ curves due to hysteresis and the overburden pressure were well reproduced by the Leverett scaling approach.

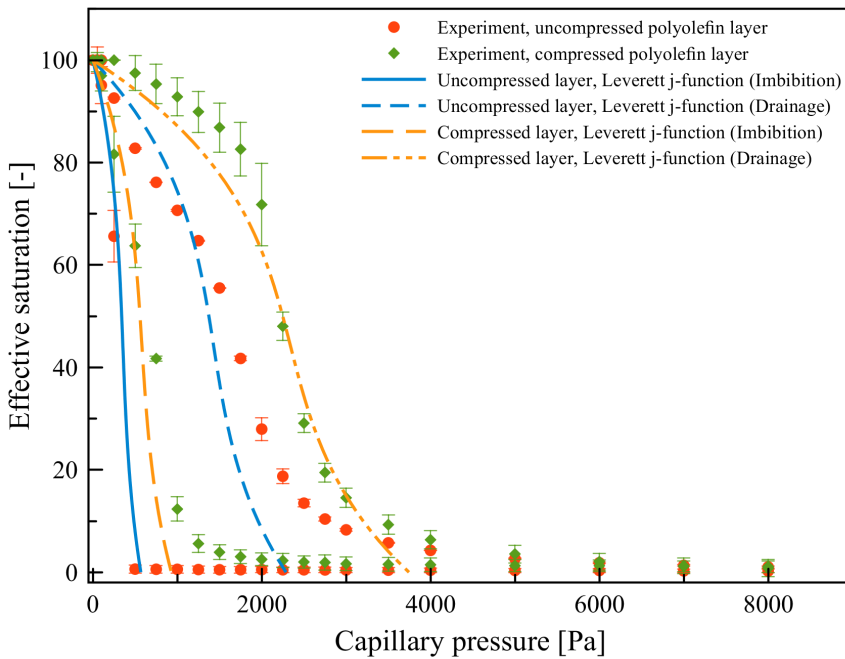


Figure 2.9 Observed and fitted imbibition-drainage curves of a compressed polyolefin layer using Leverett's J function. The fitted curve was used to obtain the $P_c(S)$ curve for an uncompressed layer based on Eq. (5).

2.5 Conclusions

In this research, we investigated the effect of several factors on the capillary pressure-saturation curves of two different thin non-woven fibrous materials. Results for both materials demonstrated the important effect of overburden pressure on the $P_c(S)$ curves. However, increasing the number of layers did not seem to affect the curves drastically. Additionally, the influence of multiple imbibition-drainage cycles showed that wetting of a sample in the first cycle would increase the capillarity in the next cycles. We used both the unimodal van

Genuchten and bimodal Durner models to fit the experimental data. The Durner model is recommended when the capillary pressure-saturation data show clear bimodal (dual-porosity) behavior. One major question that remained unanswered is how the capillary-pressure saturation function of non-woven fabric (like that of many medical absorbent products) may change during dynamic flow conditions, like has been noted for other porous media (Hassanizadeh et al. 2002). Work on dynamic capillary pressure-saturation curves is still in progress.

2.6 Appendix A: Influence of capillarity on liquid accumulation inside the chamber

One major challenge when measuring capillary pressure-saturation curves of a thin layer, such as of the polyolefin fabric discussed in this paper, is the fact that the total volume of pores being drained or filled is very small. This will cause small changes in the water volumes of other parts of the setup, which usually can be neglected when working with large samples, to affect the results. It is therefore important to quantify these types of effects and correct the measurement results if needed. For example, as explained in Section 2.3, some water droplets may form during imbibition along the open surface of the membrane (i.e., the part that is not covered by the sample; see Figure 2.1). Also, a very small amount of water may accumulate wherever there is a corner, due to capillary rise. This could happen along the edge of the membrane against the sample chamber wall and around the edge of metal weight that is placed on top of the sample in the experiments with an overburden pressure. Capillary rise and the associated volumes are expected to depend on the gas pressure, and may be different during drainage and imbibition. For this reason, we performed a set of full imbibition-drainage cycle measurements without placing a sample in the chamber (the blank runs). Measurements were performed with and without metal weight. Results are shown in Figure 2.A-1. The maximum uptake volume of 140 – 200 μl in the blank runs was comparable to the total pore volume of a polyolefin layer. To reduce this uncertainty, we modified the setup. This reduced the capillary rise and the associated volume drastically, as seen in Figure 2.A-2.

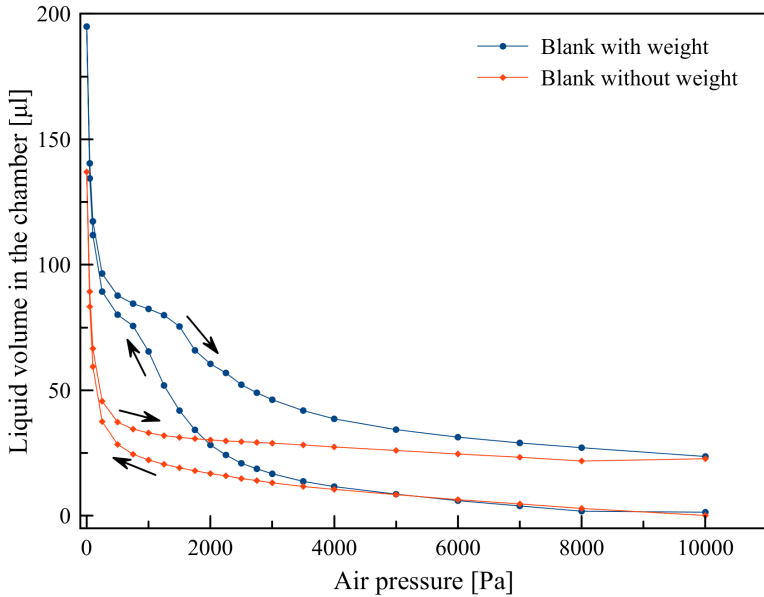


Figure 2.A-1 Liquid volume inside the blank chamber at different pressures.

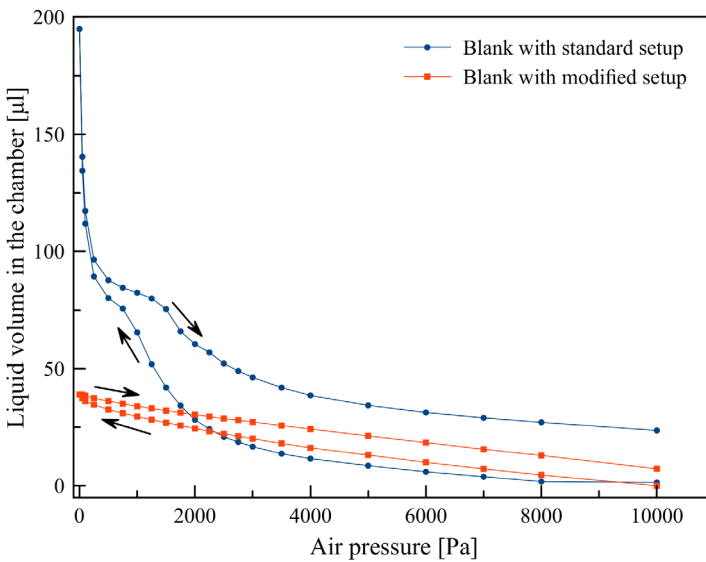


Figure 2.A-2 Observed volumes of liquid inside the blank chamber with standard and modified setup at different pressures (a metal weight was placed on top of membrane in both cases).

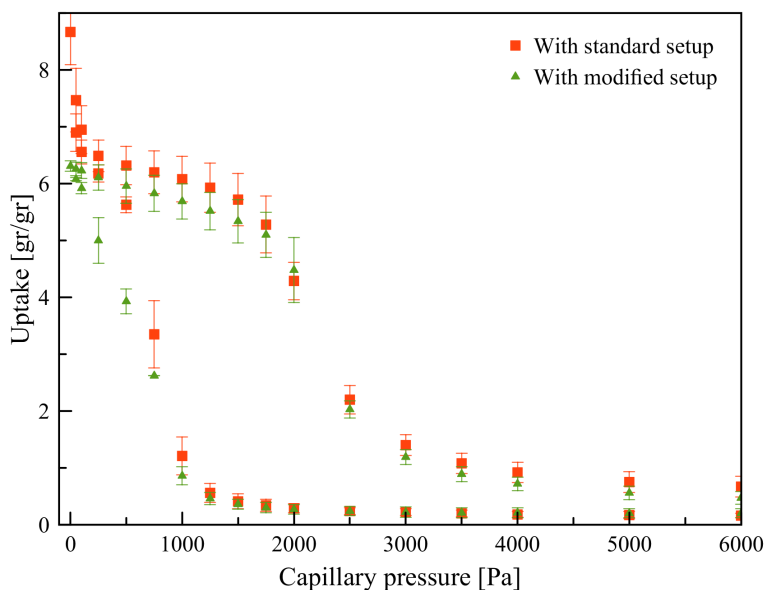


Figure 2.A-3 Liquid volume of a single polyolefin layer, subject to a 0.3 psi overburden pressure, divided by its dry weight as measured at different capillary pressures using standard and modified chambers (the average dry weight of a single layer was about 49 mg).

Measured data using blanks with standard and modified setup are shown in Figure 2.A-3. As can be seen, the experimental artifacts diminished when a modified blank was used. Of course, one can use the curves obtained from a standard setup, provided a correction can be made for water uptakes at pressures close to zero.

For samples with much higher uptake of fluid than the blank, the influence of the blank at the lower pressures becomes unimportant. For instance, although PET layers (discussed in section 2.6) are physically thin (i.e. less than 10 pores their width), the uptake was almost 5 times greater than the maximum blank uptake, which indicates that the blank run artifact at lower pressures is negligible. One can also increase the number of layers to diminish the blank effect for samples with small pore volumes. The problem is that, when using multilayers, the interlayer space pores will be introduced into the system, which may lead to other artifacts. However, we studied the effect of number of layers on capillary pressure-saturation measurements in section 4, and showed it to be negligible.

2.7 Appendix B: Influence of equilibration threshold value

As explained in Section 2.3 on experimental procedures, equilibrium conditions were assumed to be reached when the rate of water mass loss was below a certain threshold value, which was supposed to be the rate of evaporation from the solution reservoir. Unfortunately, the exact evaporation rate was not known. Imposing a very low threshold value would mean that the entire measurement process would take extremely long. A high threshold value on the other hand would affect the saturation measurements. We evaluated the effect of the threshold value on the measured capillary pressure-saturation curve for a single layer of polyolefin subject to overburden pressure. Results are presented in Figure 2.B-1. Based on these results and the evaporation rate of the solution reservoir, we selected a threshold value of 1 mg/min.

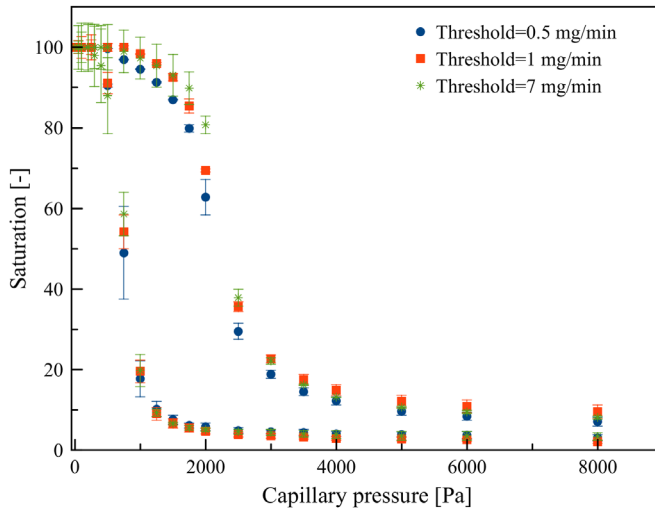


Figure 2.B-1 Liquid Observed capillary pressure-saturation data for a single polyolefin layer under 0.3 psi overburden pressure assuming three different equilibrium threshold values.

2.8 Appendix C: Dynamics of fluid flow during measurements of $P_c(s)$ curves

Figure 2.C-1 shows capillary pressure-saturation data for a single polyolefin layer subject to an overburden pressure during non-equilibrium conditions. The water

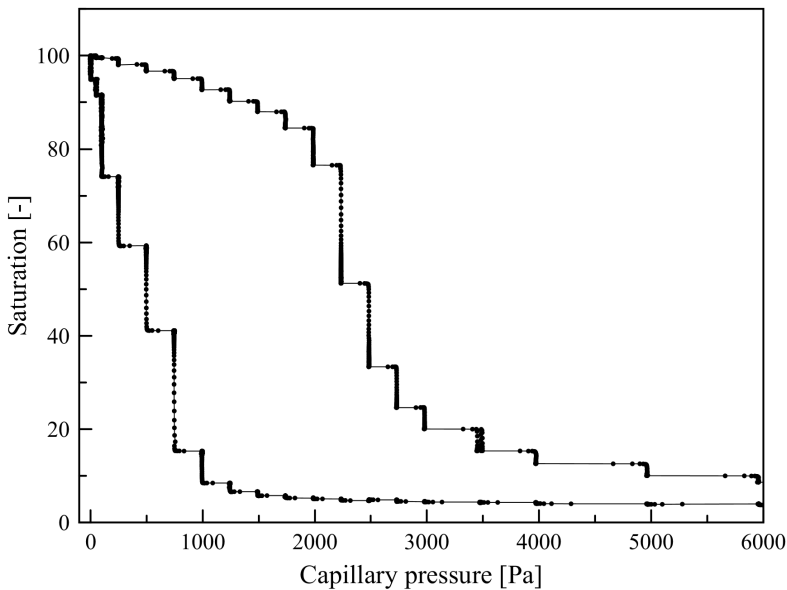


Figure 2.C-1 All measured capillary pressure-saturation data points for a compressed single polyolefin layer.

pressure during imbibition is then expected to be negative and positive during drainage. However, because of the lack of water pressure measurement, we assumed the water pressure to be constant in non-equilibrium states, which was not be the case shown in several earlier studies (Hassanizadeh et al. 2002). The $P_c(S)$ curve shown in Figure 2.C-1 was obtained based on this assumption.

Figure 2.C-2 shows changes in saturation over time for a single layer and a stack of two layers, without an overburden pressure, when the air pressure was reduced from 500 Pa to 250 Pa during imbibition. Clearly, the interlayer pore space had an appreciable impact on the dynamic of unsaturated fluid flow through the stack of layers.

This suggests that one needs to consider also any layer-layer exchange of fluid during non-equilibrium conditions. One way to model this problem would be by using an exchange term of fluid flow between the two layers through the higher porosity part in between the two layers, similarly as is often done when modeling fluid flow in unsaturated fractured rocks of microporous soils (Gerke and van Genuchten 1993). Another approach would be to use a complete two-dimensional

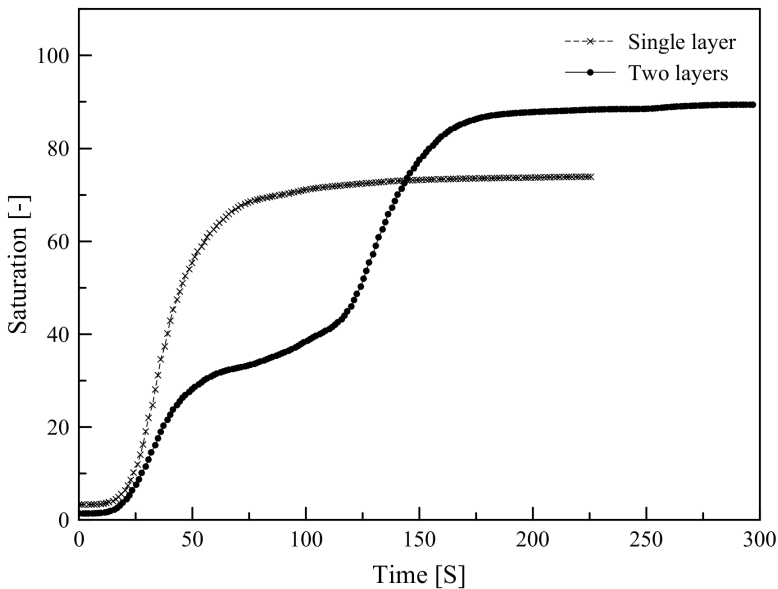


Figure 2.C-2 Dynamics of water infiltration in an uncompressed single and double polyolefin layers (the air pressure decreased from 500 to 250 Pa).

model assuming two layers separated in some continuous fashion by another medium with higher porosity and saturated permeability properties.

References

- Albrecht, W., Fuchs, H., Kittelmann, W.: *Non-woven Fabrics: Raw Materials, Manufacture, Applications, Characteristics, Testing Processes*, Wiley (2003)
- Ashari, A., Tafreshi, H. V.: General capillary pressure and relative permeability expressions for through-plane fluid transport in thin fibrous sheets. *Colloid Surf. A* 346, 114 (2009)
- Aslannejad, H. and Hassanizadeh, S. M.: Study of hydraulic properties of uncoated paper: Image analysis and pore-scale modeling. *Transport in Porous Media*. 120, 67–81(2017)
- Brooks, R. H., Corey, A. T.: Hydraulic properties of porous media. Hydrology Paper No. 3. Colorado State Univ. Fort Collins, Colorado, 27 pp. (1964)
- Ceballos, L., Prat, M., Duru, P.: Slow invasion of a non-wetting fluid from multiple inlet sources in a thin porous layer. *Phys Rev E*. 84, 056311 (2011)
- Durner, W.: Hydraulic conductivity estimation for soils with heterogeneous pore

- structure. *Water Resources Research*. 32(9), 211–223 (1994)
- Fairweather, J. D., Cheung, P., St-Pierre, J., and Schwartz, D. T.: A Microfluidic Approach for Measuring Capillary Pressure in PEMFC Gas Diffusion Layers. *Electrochemistry Communications*. 9(9), 2340-2345 (2007)
- Gerke, H.H., van Genuchten, M.Th.: Evaluation of a first order water transfer term for variably saturated dual-porosity flow models. *Water Resour. Res.* 29, 1225–1238 (1993)
- Gostick, J.T., Fowler, M. W., Ioannidis, M.A., Pritzker, M. D., Volfkovich, Y.M., Sakars, A.: Capillary pressure and hydrophilic porosity in gas diffusion layers for polymer electrolyte fuel cells. *J. Power Sources* 156, 375–387 (2006)
- Gostick, J.T., Ioannidis, M.A., Fowler, M. W., Pritzker, M. D.: Direct measurement of the capillary pressure characteristics of water-air-gas diffusion layer systems for PEM fuel cells. *Electrochemistry Communications* 10, 1520-1523 (2008)
- Hassanizadeh, S.M., Celia, M.A., Dahle, H.K.: Dynamic effects in the capillary pressure-saturation relationship and their impacts on unsaturated flow. *Vadose Zone Journal*, 1. 38-57 (2002)
- Jaganathan, S., Tafreshi, H. V., Pourdeyhimi, B.: A realistic modeling of fluid infiltration in thin fibrous sheets. *J. Appl. Phys.* 105, 113522 (2009a)
- Jaganathan, S., Tafreshi, H.V., Shim, E., Pourdeyhimi, B.: A study on compression-induced morphological changes of non-woven fibrous materials. *Colloids Surf. A* 337(1–3):173–9 (2009b)
- Jena, A.K., Gupta, K.M.: In-plane compression porometry of battery separators. *J. Power Sources* (80). 46–52 (1999)
- Jena, A., Gupta, K.: Characterization of Pore Structure of Fuel Cell Components Containing Hydrophobic and Hydrophilic Pores. 41st Power Sources Conference (2005)
- Kumbur, E. C., Sharp, K. V., and Mench, M. M.: Validated Leverett Approach for Multiphase Flow in PEFC Diffusion Media, I. Hydrophobicity Effect. *Journal of the Electrochemical Society*. 154(12), B1295-B1304 (2007a)
- Kumbur, E. C., Sharp, K. V., and Mench, M. M.: Validated Leverett Approach for Multiphase Flow in PEFC Diffusion Media, II. Compression Effect. *Journal of the Electrochemical Society*. 154(12), B1305-B1314 (2007b)
- Landeryou, M., Eames, I., Cottenden, A.: Infiltration into inclined fibrous sheets. *Journal of Fluid Mechanics*. 529, 173–193 (2005)
- Leverett, M.C.: Capillary Behavior in Porous Solids. *Trans. Sot. Pet. Eng. AIIME*. 142, 152-169 (1941)
- Miller, B., Tyomkin, I.: Liquid porosimetry: new methodology and applications. *J Col Int Sci*. 62,163-170 (1994)
- Nguyen, T. V., Guangyu, L., Heebong, O., Dan, H., David, J., and Muhammad, A.: Measurements of Two-Phase Flow Properties of the Porous Media Used in PEM Fuel Cells. *ECS Transactions*. 3(1), 415-423 (2006)

- Nguyen, T.V., Lin, G., Ohn, H., Wang, X.: Measurement of capillary pressure property of gas diffusion media used in proton exchange membrane fuel cells. *Electrochem. Solid-State Lett* 11, B127–B131 (2008)
- Pasaogullari, U., Wang, C.Y.: Two-phase transport and the role of micro-porous layer in polymer electrolyte fuel cells. *Electrochim.Acta.* 49, 4359–4369 (2004)
- Pinder, G. F., Gray, W. G.: *Essentials of Multiphase Flow in Porous Media*. WileyInterscience (2008)
- Prat, M., Agaësse, T.: Thin porous media. In: Vafai, K. (ed.) *Handbook of Porous Media* (Chapter 4), 3rd edn. Taylor & Francis, London (2015)
- Qin, C. Z. and Hassanizadeh, S. M.: Multiphase flow through multilayers of thin porous media: General balance equations and constitutive relationships for a solid-gas-liquid three-phase system. *International Journal of Heat and Mass Transfer*. 70, 693–708 (2014)
- Qin, C. Z., Hassanizadeh, S.M.: A new approach to modelling water flooding in a polymer electrolyte fuel cell. *International journal of hydrogen energy*. 40, 3348-3358 (2015)
- Sole, J.D.: Investigation of water transport parameters and processes in the gas diffusion layer of PEM fuel cells. PhD dissertation, Virginia Polytechnic Institute and State University (2008)
- Tavangarrad, A.H., Mohebbi, B., Hassanizadeh, S. M., Rosati, R., Clausen, J., Blümich, B.: Continuum-scale modeling of liquid redistribution in a stack of thin hydrophilic fibrous layers. *Transport in Porous Media*. 122, 203-219 (2018)
- Udell, K.S.: Heat transfer in porous media considering phase change and capillarity-the heat pipe effect. *Int. J. Heat Mass Transf.* 28 (2), 485-495 (1985)
- Van Genuchten, M. Th.: A closed-form equation for predicting the hydraulic conductivity of unsaturated soils. *Soil Sci Soc. Am J.* 44, 892-898 (1980)

Chapter 3

Continuum-scale modeling of liquid redistribution in a stack of thin hydrophilic fibrous layers

Published as: Tavangarrad, A.H., Mohebbi, B., Hassanizadeh, S.M., Rosati, R., Clausen, J., Blümich, B.: Continuum-scale modeling of liquid redistribution in a stack of thin hydrophilic fibrous layers. *Transport in Porous Media*. 122, 203-219 (2018).

Abstract

Macroscale three-dimensional modeling of fluid flow in a thin porous layer under unsaturated conditions is a challenging task. One major issue is that such layers do not satisfy the Representative Elementary Volume length scale requirement. Recently, a new approach, called Reduced Continua Model (RCM), has been developed to describe multiphase fluid flow in a stack of thin porous layers. In that approach, flow equations are formulated in terms of thickness-averaged variables and properties. In this work, we have performed a set of experiments, where a wet 260- μm thin porous layer was placed on top of a dry layer of the same material. We measured the change of average saturation with time using a single-sided low-field Nuclear Magnetic Resonance device known as NMR-MOUSE. We have employed both RCM and the traditional Richards equation-based models to simulate our experimental results. We found that the traditional unsaturated flow model cannot simulate experimental results satisfactorily. Very close agreement was obtained by including the dynamic capillary term as postulated by Hassanizadeh and Gray in the traditional equations. The Reduced Continua Model was found to be in good agreement with the experimental result without adding dynamic capillarity term. Moreover, the computational effort needed for RCM simulations was one order of magnitude less than that of traditional models.

3.1 Introduction

Thin non-woven fibrous materials have a wide range of applications in different industries and consumer products. Examples are papers, filters, insulators, fuel cells, fluid absorbent or barrier materials, textiles, diapers, and hygienic pads. An important process of interest is the flow of liquids through a stack of thin porous layers under unsaturated conditions. There are various research questions in the field of thin porous media related to identifying theoretical, numerical, and experimental techniques (see e.g., Prat and Agaësse 2015; Aslannejad and Hassanizadeh 2017).

Thin porous layers behave differently from thicker porous media. Some physical phenomena whose impact is weak or even negligible in an ordinary porous medium can become dominant in a thin medium (Prat and Agaësse 2015). Ceballos et al. (2011) defined a thin porous layer based on the number of pores along the thickness dimension. A discrete representation of the porous layer as a network of interconnected capillaries was used in their work to simulate a pore-scale drainage process in a thin fibrous layer. They showed that number of variables in their thin porous medium, such as the invading phase overall saturation at the end of the displacement and the receding phase saturation profiles are different from those of a thick one for a particular displacement process.

Research on understanding the behavior of thin porous media under unsaturated flow conditions has been done on both continuum and pore scales. Rebai et al. (2009) used traditional continuum models and a pore-network model to predict the water distribution across a thin layer. They stated that traditional continuum-scale modeling cannot be relied on to compute the water distribution along the thickness of thin layers because the pore size is comparable to the thickness. Although the applicability of traditional continuum models, like the Richards equation (1931), to thin fibrous media is questionable, they are commonly used to predict water infiltration (Landeryou et al. 2005; Tafreshi and Bucher 2013; Jaganathan et al. 2009; Landeryou et al. 2003) or drainage (Ashari et al. 2011; Ashari and Tafreshi 2009).

Landeryou et al. (2005) studied in-plane infiltration in horizontal and inclined thin fibrous sheets experimentally and numerically. Results of their continuum Richards modeling for a horizontal sheet, subject to a capillary driven line source

boundary condition, showed that measured saturation profiles were significantly sharper than modeling results. For the inclined sheet experiments, their numerical results for a point source boundary condition overpredicted the rate of water infiltration in cross-slope direction while satisfactory results were obtained for the down slope direction. They proposed that by including a percolation threshold in relative permeability function, one may be able to reduce calculated infiltration rate in lateral direction.

Tafreshi and Bucher (2013) also studied the in-plane absorption of water in a thin fibrous sheet. They showed that simulation results of Richards equation can be verified against an analytical expression given by Marmur (1988). They also reviewed in-plane infiltration experimental studies in the literature that were compared with Marmur equation. They also stated that water infiltrates a thin fibrous sheet preferably in the direction of fibers. Consequently, if fibers are predominantly perpendicular to the direction of flow, their impeding effects should be expressed in relative permeability function.

Among others, Ashari et al. (2011) used Richards equation to model drainage of fluid from thin non-woven fibrous layer in the through-plane direction. They pulled around a partially saturated thin layer over a rough solid surface causing water to leave the layer. They measure average saturation of the layer as a function of time. They used a special boundary condition containing a coefficient which was fitted in order to match measured data.

Qin and Hassanizadeh (2015) proposed two definitions for a thin porous layer: physically thin layer and geometrically thin layer. A ‘physically thin layer’ is a layer that does not satisfy the Representative Elementary Volume (REV) length-scale requirement. According to that requirement, macroscale properties should be defined for an averaging volume (REV) whose size is more than one order of magnitude larger than pore sizes and more than one order of magnitude smaller than overall size of porous material. This means that for macroscale (continuum scale) equations to be valid, the material thickness must be a few orders of magnitude larger than pore or grain sizes. Therefore, a layer whose thickness is only 10 times larger than its mean pore size does not meet REV requirements. So, they argued that the applicability of continuum models to physically thin porous media is questionable. A ‘geometrically thin porous layer’ was defined as a layer that satisfies the REV requirement, but its thickness is much smaller than its planar

dimensions. Recently, Qin and Hassanizadeh (2014) developed a new approach for modeling multiphase flow in a stack of physically thin porous layers, based on thermodynamic considerations. They referred to it as the Reduced Continua Model (RCM). All governing equations in this model are formulated in terms of thickness-averaged properties. Therefore, a 3D system is reduced to a two dimensional domain, which it needs to be discretized only in the lateral directions. Qin and Hassanizadeh (2015) found good agreement between traditional continuum scale models and the RCM for modeling the fluid flow in a thin hydrophobic material. However, their results have not yet been validated against any experimental data.

Experimental techniques for the investigation of fluid distributions in thin layers and their dynamics are challenging. Commonly, gravimetric measurements are used to quantify the amount of liquid in layered textile materials. However, these methods cannot reveal details of the liquid distribution or flow dynamics inside the material.

There are several non-destructive techniques, such as X-ray tomography (Weder et al. 2006) and scanning neutron radiology (Weder et al. 2004; Pel et al. 1993), that have been employed to investigate the movement and distribution of water within porous substrates. However, using these instruments in bench-top setups is difficult and special precautions are required to obtain meaningful information. Magnetic Resonance Imaging (MRI) is another method that enables non-invasive monitoring of fluid flow through porous materials (Leisen et al. 2001). However, MRI has been used mainly for thicker layered materials, such as carpets, to study the evaporation and drying of substrates (Leisen and Beckham 2001; Carr et al. 1998). Alternatively, Nuclear Magnetic Resonance (NMR) has been used for determining liquid distributions inside porous materials, such as soil, concrete, building materials and food (Blümich et al 2011; Blümich et al. 2009).

In this study, a bench-top single-sided NMR device called NMR-MOUSE (**MO**bile-**U**niversal-**S**urface-**E**xplorer) (Perlo et al. 2005) has been used for dynamic measurements of drainage processes through thin porous layers (Figure 3.1). In particular, the change of water saturation in a wet layer draining to an underlying dry layer is monitored. We have also performed continuum-scale modeling of liquid flow from the top to the bottom layer, employing both, traditional Richards equation and the new RCM approach. The two models were

calibrated in order to simulate drainage of a hydrophilic thin fibrous layer. This is the first time that the RCM approach has been compared to experimental results. In addition, in both models, we have accounted for a dynamic capillarity term as postulated by Hassanizadeh and Gray (1993).

3.2 Experimental methods and materials

3.2.1 Materials

The material used in this study was a thin non-woven porous layer made of polyolefin-based fibers. It is thermally bonded in some regions during the fabrication process with a lozenge bonding pattern. A specific surfactant has been added to this material to make it hydrophilic. The layer was about 260 μm thick with around 90% porosity. Other properties including fiber radius and density are given in Table 3.1. A saline solution, made of 0.9% NaCl (by weight) and distilled water, was chosen as the working liquid. The solution has a surface tension of 72.5 mN/m, a density of 1.005 g/cm³, and a viscosity of 1.019 mPa.s. The fibrous material exhibits negligible swelling in such a solution.

3.2.2 NMR instrument

The NMR-MOUSE (Magritek Europe, Aachen, Germany) consists of a surface rf (radio-frequency) coil placed above four permanent magnets (Figure 3.1). Two

Table 3.1 Properties of hydrophilic fibrous layers used in this study

Parameter	Value	Unit
Porosity, φ	0.9	-
Fiber radius, r	10	μm
Fiber density, ρ^f	0.92	gr/cm ³
Permeability, K	2.05×10^{-10}	m ²
Fitting parameters in the VG model of imbibition curve, α	0.00378	1/Pa
Fitting parameters in the VG model of imbibition curve, n	8.53	-
Irreducible Saturation, S_{ir}	0.02	-
Fitting parameters in Durner model of drainage curve, w_f, w_m	0.42, 0.58	-
Fitting parameters in Durner model of drainage curve, α_f, α_m	0.0026, 0.00056	1/Pa
Fitting parameters in Durner model of drainage curve, n_f, n_m	2.07, 6.64	-

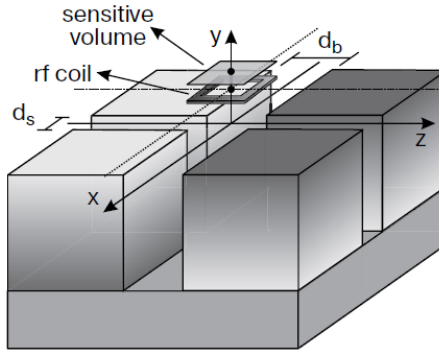


Figure 3.1 Magnet arrangement in a NMR-MOUSE which collect signal from a flat sensitive volume above the sensor. The direction of the polarization of the magnets is indicated by the gray scale.

magnets with the same polarization were separated by a distance d_s . The magnets with opposite polarization were separated by a distance d_b , which was larger than d_s . The NMR-MOUSE used in this work generated a uniform magnetic field gradient of 8 T/m in a magnetic field of 0.32 Tesla (^1H frequency of 13.8 MHz) in a sensitive volume located at 25 mm above the surface of magnets (see Figure 3.1). The sensitive volume had a thickness of 200 μm and lateral dimension of 40 mm by 40 mm. The elevation of sensitive volume could be varied with the help of a high precision lift moving the magnets up and down, while keeping the sample fixed. The NMR signal was acquired with a CPMG multi-echo sequence (Carr and Purcell 1954).

A quadratic 40-mm diameter surface coil was used to excite the NMR signal from the sensitive volume. The sensitive volume thickness Δz , is proportional to the bandwidth of the rf-pulse according to the following formula:

$$\Delta z = 2\pi\Delta\nu/G_z\gamma \quad (3.1)$$

where $\Delta\nu$ is the excitation bandwidth, G_z is the magnetic field gradient, and γ is the gyromagnetic ratio. In the CPMG sequence, the spatial resolution and the thickness of the sensitive volume could be adjusted by changing the number (m) of acquisition points in each echo and the dwell time (dw); this resulted in an acquisition time of $m \cdot dw$ for each echo. A 200- μm thick sensitive volume was

created in our experiments. With each CPMG sequence, 128 echoes were acquired (echo time $t_E = 90 \mu\text{s}$, repetition time $t_R = 200 \text{ ms}$, number of scans = 1500).

3.2.3 Water redistribution experiment

The main objective of this experiment was to monitor the dynamic drainage process of a thin porous material. This was done by placing a fully saturated layer of non-woven fabric on top of a dry layer and monitoring the change of saturation in the wet layer (Figure 3.2). Experiments were performed in a climate control environment, at 24°C and a humidity of 46%.

For the measurements, two identical samples with dimension of $40 \times 40 \text{ mm}^2$ and thickness of $260 \mu\text{m}$ were cut. A glass slide with thickness of $150 \mu\text{m}$ was placed on top of the coil and a dry sample was placed on it. Then, the other sample was saturated with the saline solution and placed over the dry sample. Next, using the high precision lift, the sensitive volume with a thickness of $200 \mu\text{m}$ was positioned inside the upper layer.

In order to account for the evaporation from the wet layer, an additional experiment was done in the same climate-controlled lab. In this experiment, a fully saturated layer was placed on a balance and the weight loss over time was measured. This allowed us to compute the evaporation rate. The experimental results for the drainage were corrected by taking the measured evaporation rate into an account.

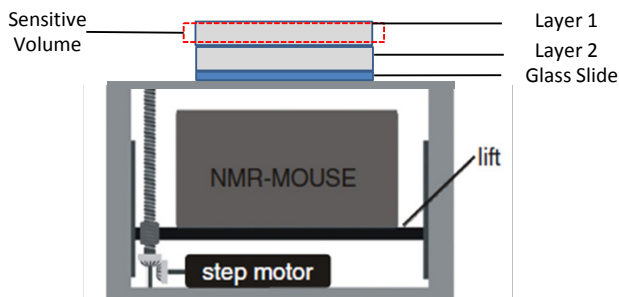


Figure 3.2 Placement of two thin non-woven layers on top of the NMR sensor where layer 1 is fully saturated and layer 2 is dry.

3.3 Modeling approaches

3.3.1 Richards model

Here, we describe two approaches for modeling liquid flow through a stack of thin layers. Most commonly used models for flow of a liquid through a thin porous medium under unsaturated conditions are based on the Richards equation, which assumes that the air phase is infinitely mobile. It is obtained by writing the mass conservation of the wetting phase in following form:

$$\frac{\partial(\rho^w \varphi S^w)}{\partial t} + \nabla \cdot (\rho^w \mathbf{v}^w) = 0 \quad (3.2)$$

where ρ^w is the mass density of wetting phase and φ is the porosity, S^w is the saturation of the wetting phase. When neglecting gravity the Darcy velocity vector \mathbf{v}^w is given by:

$$\mathbf{v}^w = -\frac{k^r K}{\mu^w} \nabla P^w \quad (3.3)$$

where K is the intrinsic permeability, k^r is the relative permeability of the wetting phase, μ^w is the dynamic viscosity of the wetting phase and ∇P^w is the pressure gradient. In our study, gravity is negligible due to the small thickness of the layers.

To finalize the relationships between water pressure, saturation and relative permeability, the macroscopic capillary pressure is commonly assumed to be equal to the difference in fluid pressures:

$$P^a - P^w = P^c(S^w) \quad (3.4)$$

where P^a is the air pressure and $P^c(S^w)$ is the capillary pressure, which traditionally is assumed to be a solely function of saturation. However, based on a rigorous thermodynamic approach, Hassanizadeh and Gray (1990) proposed the existence of a dynamic component that depends on $\frac{\partial S^w}{\partial t}$. Later on, Hassanizadeh and Gray (1993) developed the following linear approximation for the difference in fluid pressures under dynamic conditions:

$$P^a - P^w = P^c(S^w) - \tau \frac{\partial S^w}{\partial t} \quad (3.5)$$

where τ is a material coefficient, which should be determined experimentally. Reviews of issues related to dynamic capillarity effect can be found in Hassanizadeh et al. (2002) and Jokar-Niasar and Hassanizadeh (2012).

A nonlinear relationship suggested by Van Genuchten (VG) can be used for the capillary pressure function as follows:

$$P^c(S_e) = \frac{1}{\alpha} (S_e^{-1/m} - 1)^{1/n} \quad (3.6)$$

where α and n are fitting parameters, $m = 1 - 1/n$, and $S_e = (S^w - S_{ir})/(1 - S_{ir})$ in which S_{ir} is the irreducible water saturation. Due to very large porosity of the samples, no residual air needs to be considered. In some cases, a modified VG equation needs to be used where m is also considered as a fitting parameter. All parameters in this equation have to be determined experimentally.

Furthermore, the relative permeability is assumed to be a function of saturation. One common formula for relative permeability was suggested by Van Genuchten (1980) as:

$$k^r(S^w) = S_e^l (1 - (1 - S_e^{1/m})^m)^2 \quad (3.7)$$

where m is the same parameter that appears in the $P^c - S^w$ relationship and $l = 0.5$.

Another relationship is a power-law model based on the empirical correlation of Brooks and Corey (1964):

$$k^r(S^w) = (S^w)^\delta \quad (3.8)$$

where δ is as a material property and should be determined experimentally. There exist some experimental studies for the determination of δ for a thin fibrous layer (Sole 2008; Hussaini and Wang 2010). For in-plane permeability, Hussaini and Wang (2010) found a value of $\delta=4$ for a thin non-woven fibrous layer, but they report large uncertainties in their measurements (Hussaini and Wang 2010). A wide range of values for this coefficient ($3 \leq \delta \leq 6$) has been used in numerical simulations of thin fibrous layers (Jaganathan et al. 2009; Landeryou et al. 2005; Ashari and Tafreshi 2009).

For the case of a heterogeneous pore structure, a multimodal function proposed by Durner (1994) can be used to define the hydraulic functions. For instance, in the

case of a bimodal retention function, equation (3.6) and (3.7) are replaced by the following two equations (Durner 1994; Van Genuchten and Pachepski 2011):

$$S_e(h) = \frac{w_f}{[1 + |\alpha_f h|^{n_f}]^{m_f}} + \frac{w_m}{[1 + |\alpha_m h|^{n_m}]^{m_m}} \quad (3.9)$$

$$k^r(S_e) = \frac{(w_f S_{e_f} + w_m S_{e_m})^{l_d} \{w_f \alpha_f (1 - (1 - S_{e_f}^{1/m_f})^{m_f}) + w_m \alpha_m (1 - (1 - S_{e_m}^{1/m_m})^{m_m})\}^2}{(w_f \alpha_f + w_m \alpha_m)^2} \quad (3.10)$$

where h is the capillary pressure head, subscripts f and m refer to fracture (macro-pore) and matrix (micro-pore), respectively, $\alpha_f, n_f, \alpha_m, n_m$ are fitting parameters, w_f and w_m are weight factors for overlapping regions ($w_f + w_m = 1$). Further, $l_d = 0.5, m_f = 1 - \frac{1}{n_f}, m_m = 1 - \frac{1}{n_m}$ and $S_e = w_f S_{e_f} + w_m S_{e_m}$.

3.3.2 Reduced continua model (RCM)

Application of Richards equation requires discretization of the modeling domain over the layer thickness. An alternative model is the Reduced Continua Model (RCM), where equations of water flow are formulated in terms of thickness-averaged material properties. Therefore, as mentioned before, the dimensionality of a problem is reduced by one order and needs to be discretized in planar directions only. In this approach, macroscale balance laws are formulated based on measurable thickness-averaged properties. The layer-layer interactions are accounted by a transfer term for mass, heat and momentum. Close form of governing equations are derived based on second law of thermodynamics. The mass conservation for liquid transport in a layer i can be written as (Qin et al. 2015):

$$\left(\frac{\partial (b \rho^w \varphi S^w)}{\partial t} + \nabla_h \cdot (b \rho^w \mathbf{v}_h^w) \right) \Big|_i = Q_T^w \Big|_i + Q_B^w \Big|_i \quad (3.11)$$

where \mathbf{v}_h^w denotes the planar Darcy velocity vector, ∇_h is the planar spatial gradient, $Q_T^w \Big|_i$ and $Q_B^w \Big|_i$ indicate liquid inflow and outflow from the layer i , respectively, and b is the layer thickness.

The planar velocity \mathbf{v}_h^w is given by a Darcy-like equation, which in the case of negligible gravity reads:

$$\mathbf{v}_h^w|_i = \left(-\frac{k^r K}{\mu^w} \nabla_h P^w\right)|_i \quad (3.12)$$

where P_i^w is the thickness-averaged wetting phase pressure.

One major issue in the RCM model is the characterization of the terms $Q_T^w|_i$ and $Q_B^w|_i$. Based on thermodynamic considerations and some simplifying assumptions, Qin and Hassanizadeh (2014) proposed the following equation:

$$Q_B^w|_i = -Q_T^w|_{i+1} = \Pi_m^{i,i+1}(P_{i+1}^w - P_i^w) \quad (3.13)$$

where the subscripts i and $i + 1$ denote two neighboring layers, $Q_B^w|_i$ is the flux leaving the bottom of top layer while $Q_T^w|_{i+1}$ is the water flux entering the upper surface of the bottom layer, and $\Pi_m^{i,i+1}$ is a mass transfer coefficient (Figure 3.3). The coefficient $\Pi_m^{i,i+1}$ is specific to the two layers but also includes the nature of contact surface between the two layers. For example, pressing the two layers together may change the value of this mass transfer coefficient. Assuming continuity of the flow rate at the contact area, the following equation can be obtained for the mass transfer coefficient:

$$\Pi_m^{i,i+1} = \frac{2}{b_i + b_{i+1}} \rho^w \frac{\bar{K}_t}{\mu^w} \quad (3.14)$$

Where \bar{K}_t is an effective through-plane permeability of the two layers and is defined as follows:

$$\bar{K}_t = \left(\frac{b_i + b_{i+1}}{b_{i+1}K_i k_i^r + b_i K_{i+1} k_{i+1}^r} K_i k_i^r K_{i+1} k_{i+1}^r\right) \quad (3.15)$$

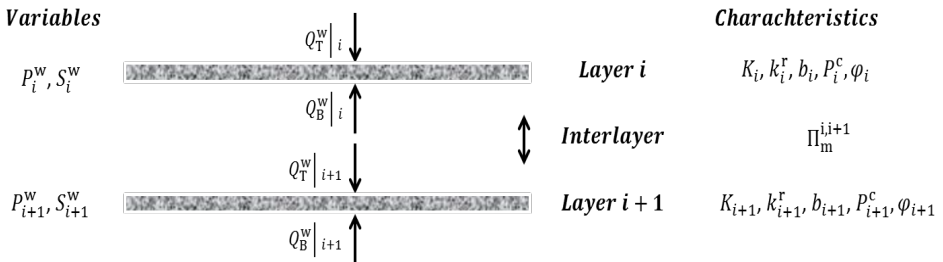


Figure 3.3 A sketch of stack of two layers with their characteristics and variables used in RCM model.

Equation (3.15) is analogous to Kirchhoff's law for electrical resistors. Note that \overline{K}_t is a function of saturations of the two layers through their relative permeability functions k_i^r and k_{i+1}^r . Alternatively, the effective through-plane permeability \overline{K}_t can be written in following form, as proposed by Qin and Hassanizadeh (2015):

$$\overline{K}_t = \frac{b_i + b_{i+1}}{b_{i+1}K_i + b_iK_{i+1}} K_i K_{i+1} f(S_i^w, S_{i+1}^w) \quad (3.16)$$

Here, the function $f(S_i^w, S_{i+1}^w)$ accounts for the role of relative permeability functions of the two layers. Qin and Hassanizadeh (2015) proposed the following equation for this function:

$$f(S_i^w, S_{i+1}^w) = \frac{1}{2} ((S_i^w)^{\gamma_i} + (S_{i+1}^w)^{\gamma_{i+1}}) \quad (3.17)$$

where γ_i and γ_{i+1} are to be determined experimentally. In addition to equations (3.11)-(3.15), equations for capillary pressure and relative permeability are given by (3.6)-(3.7) or (3.9)-(3.10). In our study, equation (3.6) was used to fit measured imbibition data points whereas equation (3.9) was found to fit measured drainage data points more closely.

3.4 Numerical simulations

3.4.1 Values of model parameters

Properties of the layer, including porosity and permeability are listed in Table 3.1. It should be noted that porosity in Table 3.1 was measured using a Textile Research Institute Autoporosimeter (Miller and Tyomkin 1994), and the fiber radius was estimated from CT images of the layer.

The intrinsic permeability of the fibrous layer was measured in the lab with the falling head method (Head 1992). However, because the initial head of 15 cm used in the measurements could have changed the layer porosity, we also used a number of empirical equations for the calculation of the permeability as a function of porosity and fiber radius (Tomadakis and Robertson 2005; Jackson and James 1986; Davies 1973; Spielman and Goren 1968). For example, Jackson and James (1986) developed the following formula based on flow through three-dimensional arrays of cylinders to predict the permeability of a highly porous fabric:

$$K = \frac{3r^2}{20(1-\varphi)} (-\ln(1-\varphi) - 0.931) \quad (3.18)$$

where r is the fiber radius and φ the porosity of the medium. All formulas gave almost the same value of the intrinsic permeability, which was comparable to the measured value. The value reported in Table 3.1 was obtained from the formula of Jackson and James (1968).

A PVD-Autoporosimeter (Pore Volume Distribution Autoporosimeter), from the Textile Research Institute, called TRI-PVD (Miller and Tyomkin 1994), was used to measure capillary pressure-saturation data points from multistep inflow/outflow measurements. Measurements were performed for a circular piece of sample with the diameter of 50 mm. Results are shown in Figure 3.4. The best fit to the drainage data points was obtained with the Durner bimodal formula (3.9), whereas the Van Genuchten formula (3.6) was found to give the best fit for the imbibition data points (Figure 3.4). The corresponding fitted parameters are given in Table 3.1. These parameters were also used in the corresponding relative permeability functions given by equations (3.10) and (3.7).

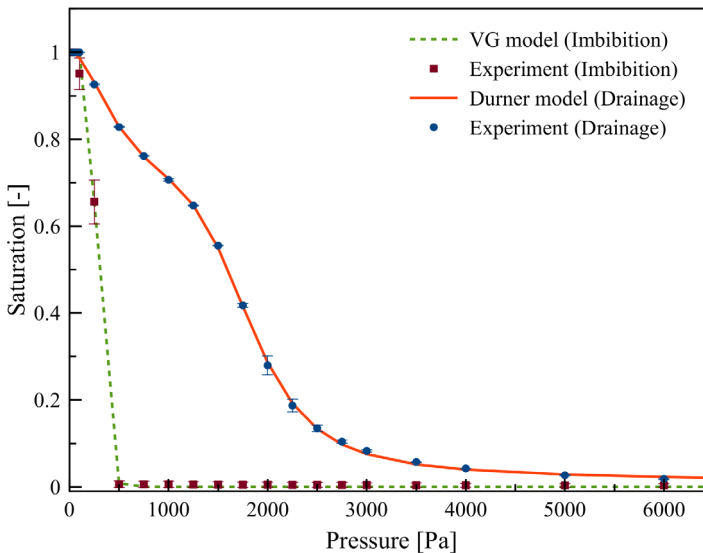


Figure 3.4 Measured capillary pressure-saturation data points for a single layer of fabric. The error bars are based on duplicate measurements. The imbibition data were fitted with the Van Genuchten formula and the drainage data with the Durner formula.

3.4.2 Richards model solution

The governing equations were solved using COMSOL (COMSOL, Burlington, USA), which is a finite element commercial software. For the simulation of the redistribution experiment, the modeling domain consisted of two layers of fabric with the total thickness of 526 μm . Because the layers were homogenous, and the upper layer was fully and uniformly saturated and the bottom layer was dry, we only needed to solve a one-dimensional downward flow problem. Our preliminary simulations using 1D Richards equation showed that 526 elements along the thickness provided mesh-independent results. Equations (3.2)-(3.3) and (3.5) were solved for both layers in this approach.

A no-flux boundary condition was imposed at both, the top and the bottom boundaries of the modeling domain. At the interface between the two layers, continuity of both pressure and flux was assumed for the Richards model.

3.4.3 RCM solution

For the RCM model, the one-dimensional simulation domain reduces to only two grid points, representing the wet and dry layers. Thus governing equations for the RCM approach reduces to an ordinary differential equation. Given the fact that we have a closed system, the sum of average saturation of two layers is constant and equal to unity all times:

$$S_1^w + S_2^w = 1 \quad (3.19)$$

where S_1^w and S_2^w indicate water saturation of top and bottom layer, respectively. Also, equation (3.13) for mass transfer term of the wet layer can be rewritten as:

$$Q_{B1}^w = \Pi_m^{1,2} (P_2^w - P_1^w) = \Pi_m^{1,2} [-P_{imb}^c (S_2^w) + P_{dra}^c (S_1^w)] \quad (3.20)$$

where we make use of the fact that air pressure is constant. As explained in the section 3.2, we can use two different formulations for the mass transfer coefficient $\Pi_m^{1,2}$. Given the fact that two layers were identical, equations (3.14) and (15) for the first formulation reduce to:

$$\Pi_{m1}^{1,2} = \frac{2}{b} \frac{\rho^w}{\mu^w} \frac{K k_1^r k_2^r}{k_1^r + k_2^r} \quad (3.21)$$

For the second formulation, the simplified form of equation (3.17) proposed by Qin et al (2015) was used and mass transfer coefficient was described by combining equations (3.14), (3.16), and (3.17):

$$\Pi_{m2}^{1,2} = \frac{1}{b} \frac{\rho^w}{\mu^w} K \frac{(S_1^w)^\delta + (S_2^w)^\delta}{2} \quad (3.22)$$

where δ is the same parameter as in the relative permeability formula (3.6). Since no measured value of δ for our thin fabric layer was available, this parameter was set equal to 4 based on suggestion of Hussaini and Wang (2010).

Based on the first formulation of mass transfer coefficient $\Pi_{m1}^{1,2}$, the following equation should be solved for the top layer, by combining equations (3.11), (3.19), (3.20) and (3.21):

$$\frac{dS_1^w}{dt} = \frac{2K}{b^2 \mu^w \varphi_1} \frac{k_1^r(S_1^w)k_2^r(1 - S_1^w)}{k_1^r(S_1^w) + k_2^r(1 - S_1^w)} [-P_{imb}^c(1 - S_1^w) + P_{dra}^c(S_1^w)] \quad (3.23)$$

Note that $P_{dra}^c(S_1^w)$ is given by Durner formula and VG model was used for $P_{imb}^c(1 - S_1^w)$ function. Relative permeability functions were determined based on fitted parameters accordingly.

Based on the second formulation for the mass transfer term, the following equation should be solved for the top layer based on equations (3.11), (3.19), (3.20), (3.22):

$$\frac{dS_1^w}{dt} = \frac{K}{b^2 \mu^w \varphi_1} \frac{(S_1^w)^4 + (1 - S_1^w)^4}{2} [-P_{imb}^c(1 - S_1^w) + P_{dra}^c(S_1^w)] \quad (3.24)$$

The third set of simulations with RCM approach was performed where we used equation (3.5) instead of equation (3.4) in order to include dynamic capillarity giving us the following equation:

$$\frac{dS_1^w}{dt} = \frac{K}{b^2 \mu^w \varphi_1} \frac{(S_1^w)^4 + (1 - S_1^w)^4}{2} [-P_{imb}^c(1 - S_1^w) + P_{dra}^c(S_1^w) - 2\tau \frac{dS_1^w}{dt}] \quad (3.25)$$

Despite the fact that we have simple ordinary differential equation, due to the strong nonlinearity of hydraulic functions, it was not possible to solve them analytically. Therefore, solutions of equations (3.23), (3.24), and (3.25) were obtained numerically using COMSOL software.

In the following section, the results for the two different modeling approaches are compared to experimental data generated by the NMR-MOUSE.

3.5 Results

3.5.1 Water redistribution Experiment

The temporal evolution of the corrected water saturation, as measured by the NMR-MOUSE for a 200- μm thick zone within the wet layer is shown by blue symbols in Figure 3.5. The raw data of experimental results were corrected based on measured evaporation rate. The light blue shadow lines represent standard deviations of three replicates. As it can be seen, the saturation of top layer decreased rapidly and reached an equilibrium value within about three minutes. Saturation change was quite small, reaching an equilibrium value of 88%. This means that the dry layer reached an average saturation of 12% only. The fact that a full redistribution does not occur when a wet and dry layer are brought into contact is well known. Similar results were obtained by Zhuang et al. (2016) in experiments involving sandy soil samples. This effect can be attributed to the hysteresis in the capillary pressure-saturation relationship.

3.5.2 Results of simulation with Richards model

We simulated this experiment using Richards and RCM models. The saturation distribution along the thickness of top layer, obtained from Richards model, was used to calculate average saturation of top layer as a function of time. Resulting curve is plotted in Figure 3.5. The model predicts very fast drainage, reaching the equilibrium saturation of about 88% in no time. We see that it is far from measured data points. Note that the equilibrium value obtained from the model is actually dictated by the $P^c(S^w)$ curve, which was measured separately.

By including a dynamic capillarity term in the Richards model, the simulation results improve significantly. Reasonably good agreement is reached between numerical simulation results and measured saturation when the τ value is set to 15000 Pa.s.

Another approach for modifying the model results without including a dynamic effect is to reduce the relative permeability values in the very low saturation range, which is relevant to the bottom layer. We achieved this by changing the value of the coefficient l in equation (3.7). Although this modification slows down the rate of change of saturation (Figure 3.6), it does not reproduce the experimental data satisfactorily. It should be noted that we also changed the value of the coefficient

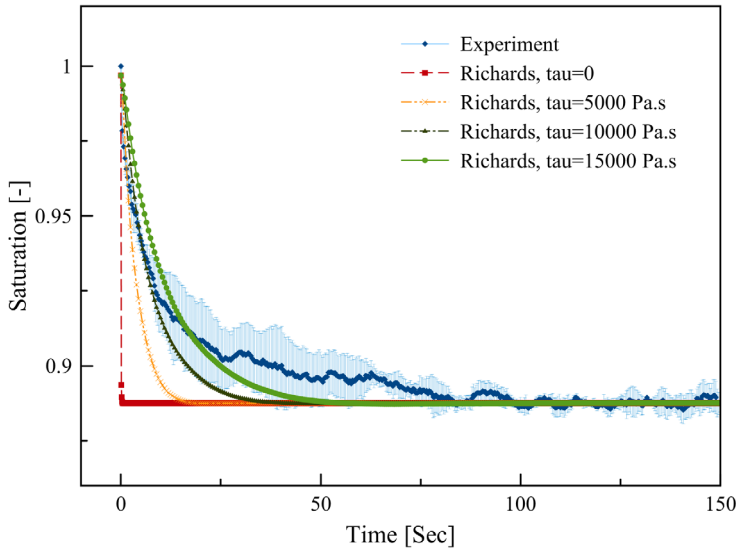


Figure 3.5 Temporal evolution of the average saturation of the top layer obtained from solving the Richards equation in comparison with the experimental NMR data. Shaded area represents standard deviation of three replicates.

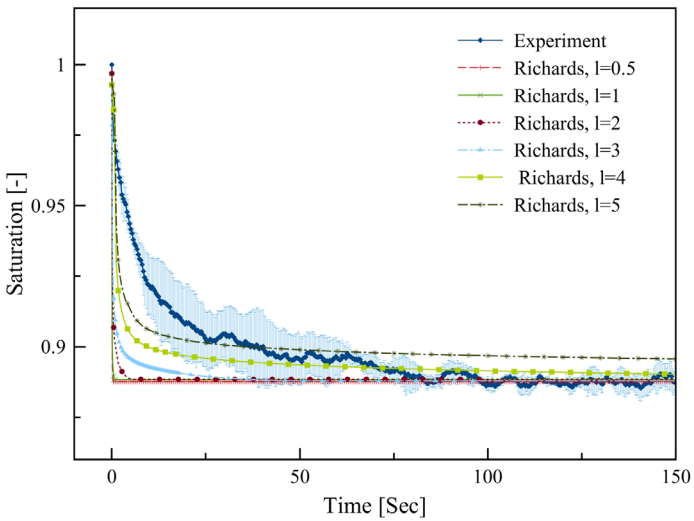


Figure 3.6 Temporal evolution of the average saturation of the top layer obtained from solving the Richards equation for different relative permeability functions and its comparison to experimental NMR data. Shaded area represents standard deviation of three replicates.

l_d in equation (3.10). However, the effect was very negligible, so that no results are shown here.

3.5.3 Results of simulation with RCM

Similar results were obtained with RCM when equations (3.24) and (3.25) were solved. Results of RCM simulations, with and without dynamic capillarity term, are compared to measurements in Figure 3.7. It is clear that including dynamic capillarity term improves simulation results significantly. The temporal evolution of saturation obtained from RCM model is almost identical to that of Richards model in this version of RCM. However, the computational time of RCM model was much smaller than Richards model. It should be noted that increasing the value of δ parameter used in the mass transfer coefficient $\Pi_{m2}^{1,2}$, up to a value of 10, had negligible impact on final results.

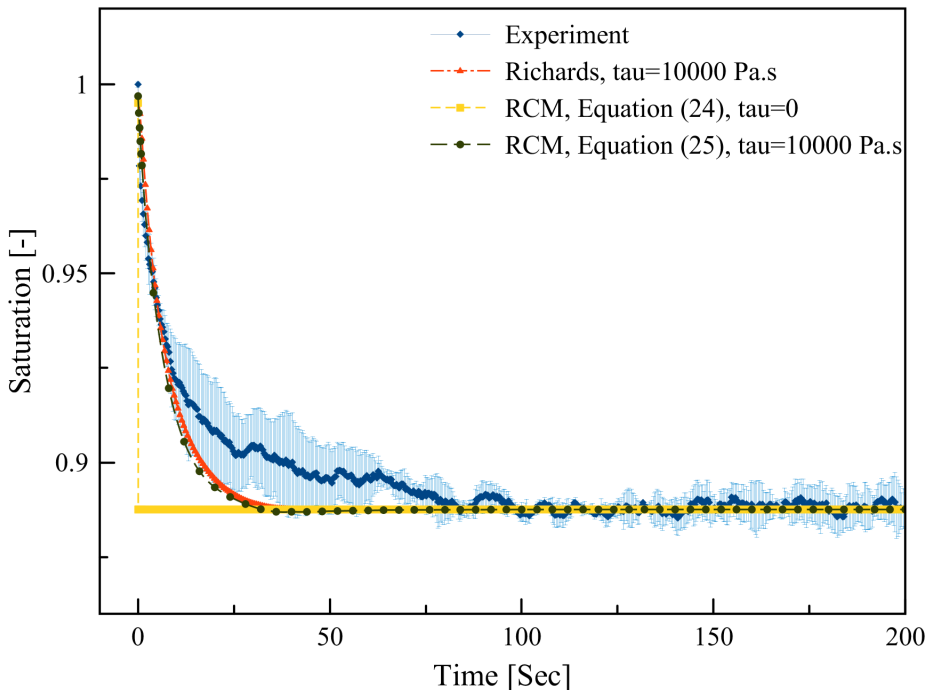


Figure 3.7 Temporal evolution of average saturation of the top layer obtained from solving the Richards equation and RCM equations (24) and (25) and its comparison to experimental NMR data. Shaded area represents standard deviation of three replicates.

Next, we used the other version of RCM, equation (3.23), to simulate the change of average saturation of top layer. Results are compared to measurements data and results from the Richards model in Figure 3.8. Here, we modified the relative permeability function for both models by including a percolation threshold as suggested by Landeryou et al. (2005). Therefore, a different relative permeability function was used for the saturation S^w below $S_e = 0.2$; namely: $k^r(S^w) = \beta S_e^{0.5}$, where β is equal to the value k^r at $S_e = 0.2$ obtained from equation (3.7) with the value of the coefficient l set to 4. It is clear that using equation (3.21) for the mass transfer coefficient in the RCM improves the simulation results remarkably. The temporal evolution of the saturation obtained from the RCM in this scenario is identical to that of the Richards model when τ is set to 8000 Pa.s (see Figure 3.8). Note that it was not needed to include the dynamic effect in the RCM. Furthermore, the computational time of the RCM was one order of magnitude less than for the Richards model. While the CPU time for the Richards model was 469 ± 14 seconds, the RCM model needed a CPU time of 51 ± 12 seconds only.

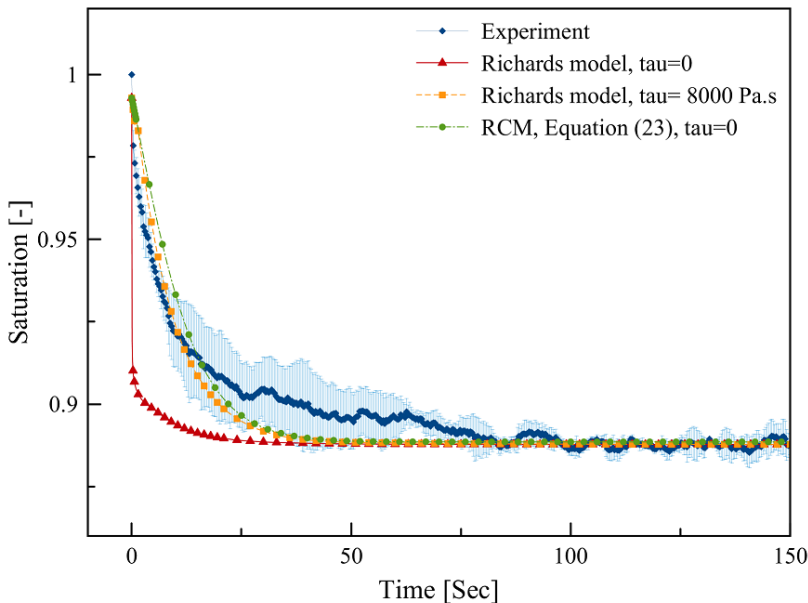


Figure 3.8 Comparison between traditional Richards model and the RCM including percolation threshold in relative permeability function in both models for the redistribution experiment. Shaded area shows standard deviation of three replicates.

3.6 Discussion and conclusions

We have found that when a fully saturated thin porous layer is brought into contact with a dry identical layer, very small water redistribution occurs. The small saturation change occurs relatively fast, in about one minute, and equilibrium saturation is reached within three minutes.

Two models were used for simulating the experiment; the standard unsaturated model, based on Richards equation, and including hysteresis, and a new approach called Reduced Continua Model (RCM). We found that the Richards model shows an unrealistically fast change of saturation. Adding a dynamic capillarity term to the Richards model helped to improve the simulation results drastically.

For the RCM model, we used two different formulations for the mass transfer between the two layers. One formulation is based on harmonic mean of relative permeability functions of two layers. The second formulation is based on simple average of power functions of the two saturations. We found that the simple average formulation behaves similarly to the Richards model; it needs the addition of a dynamic capillarity effect in order to approach the measured data reasonably well. Of course the RCM model required much less (one order of magnitude) computational time than Richards model. However, results of RCM model with the harmonic mean formulation for mass transfer coefficient matched the measurement data reasonably well without including any dynamic effect.

These studies show that a delaying mechanism in the model is needed to reproduce gradual change of saturation with time. This delaying mechanism can be either provided by dynamic capillarity effect within each layer or defining appropriate mass transfer coefficient in between the layers. The physical phenomenon behind this delay mechanism can be better explained when the pore scale experiments will be performed. A current challenge remains in performing a dynamic measurement to determine the dynamic capillarity effect in thin fibrous layers. Another challenge is to conduct experiments to better observe the effect of layer-layer exchange in both imbibition and drainage processes. Furthermore, the RCM was computationally more efficient with its computational time one order of magnitude less than that of the Richards model.

References

- Ashari, A., Tafreshi, H.V.: A two-scale modeling of motion-induced fluid release from thin fibrous porous media. *Chemical Engineering and Science*. 64, 2067–2075 (2009)
- Ashari, A., Bucher, T.M., Tafreshi, H.V.: Modeling motion-induced fluid release from partially-saturated fibrous media onto surfaces with different hydrophilicity. *Int. J. Heat Fluid Flow*. 32, 1076–1081 (2011)
- Aslannejad, H. & Hassanizadeh, S.M.: Study of Hydraulic Properties of Uncoated Paper: Image Analysis and Pore-Scale Modeling. *Transport in Porous Media*. pp 1-15 (2017)
- Blümich, B., Casanova, F., Appelt, S.: NMR at low magnetic fields. *Chem. Phys. Lett.* 477, 231–240 (2009)
- Blümich, B., Casanova, F., Dabrowski, M., Danieli, E., Evertz, L., Haber, A., van Landeghem, M., Haber-Pohlmeier, S., Olaru, A., Perlo, J., Sucre, O.: Small scale instrumentation for nuclear magnetic resonance of porous media. *New J. Phys.* 13, 1–15 (2011)
- Brooks, R. H., Corey, A. T.: Hydraulic properties of porous media. *Hydrology Paper No. 3*. Colorado State Univ. Fort Collins, Colorado, 27 pp. (1964)
- Carr, H. Y. & Purcell, E. M.: Effects of Diffusion on Free Precession in Nuclear Magnetic Resonance Experiments. *Phys. Rev.* 94,630-638 (1954)
- Carr, W.W., Beckham, H.W., Spiess, H.W., Fülber, C., Blümich, B.: Nuclear magnetic-resonance imaging of water distributions in loop-pile nylon carpet tiles. *J. Text. Inst.* 89, 436–440 (1998)
- Ceballos, L., Prat, M., Duru, P.: Slow invasion of a non-wetting fluid from multiple inlet sources in a thin porous layer. *Phys Rev E*. 84, 056311 (2011)
- Davies, C.N.: *Air Filtration*. Academic Press, London (1973)
- Durner, W.: Hydraulic conductivity estimation for soils with heterogeneous pore structure. *Water Resources Research*. 32(9), 211–223 (1994)
- Hassanizadeh, S.M., Gray, W.G.: Mechanics and thermodynamics of multiphase flow in porous media including interphase boundaries. *Adv. Water Resour.* 13, 169-186 (1990)
- Hassanizadeh, S.M., Gray, W.G.: Thermodynamic basis of capillary pressure in porous media. *Water Resour. Res.* 29, 3389–3405 (1993)
- Hassanizadeh, S.M., Celia, M.A., Dahle, H.K.: Dynamic effects in the capillary pressure-saturation relationship and their impacts on unsaturated flow. *Vadose Zone Journal*, 1. 38-57 (2002)
- Head, K.H.: *Manual of Soil Laboratory Testing*, Vols 1–3. Pentech Press, London (1992)
- Hussaini, I.S., Wang, C.Y.: Measurement of relative permeability of fuel cell diffusion media. *J Power Sources*. 195, 3830-3840 (2010)

- Jackson, G. W., James, D. G.: The permeability of fibrous porous media. *Can. J. Chem. Eng.* 64, 362-374 (1986)
- Jaganathan, S., Vahedi Tafreshi, H., Pourdeyhimi, B.: A realistic modeling of fluid infiltration in thin fibrous sheets. *J. Appl. Phys.* 105, 113522 (2009)
- Joekar-Niasar, V., Hassanizadeh, S.M.: Analysis of Fundamentals of Two-Phase Flow in Porous Media Using Dynamic Pore-Network Models: A Review. *Critical Reviews in Environmental Science and Technology*, 42:18. 1895-1976 (2012)
- Landeryou, M.A., Eames, I., Frampton, A., Cotienden, A.: Modelling Strategies for Liquid Spreading in Medical Absorbents. *Int. J. Ctothinn Sci. TechnoL.* 16, 163-172 (2003)
- Landeryou, M., Eames, I., Cottenden, A.: Infiltration into inclined fibrous sheets. *Journal of Fluid Mechanics.* 529, 173–193 (2005)
- Leisen, J., Hou, L., Beckham, H. W., and Carr, W. W.: Observation of the Water Distribution during Drying of Textiles. In: Bliimler, P., Bliimich, B., Botto, R., Fukushima, E. (eds.) *Spatially Resolved Magnetic Resonance: Methods, Materials, Medicine, Biology, Rheology, Geology, Ecology, Hardware*, pp. 265-272. Wiley-VCH, NY (1998)
- Leisen, J., Beckham, H.W.: Quantitative magnetic resonance imaging of fluid distribution and movement in textiles. *Text. Res. J.* 71, 1033–1045 (2001)
- Marmur, A.: The radial capillary, *J. Colloid Interf. Sci.* 124,301-308 (1988)
- Miller, B., Tyomkin, I.: Liquid porosimetry: new methodology and applications. *J Col Int Sci.* 62,163-170 (1994)
- Pel, L., Ketelaars, A.A.J., Odan, O.C.G., Well, A.A.: Determination of Moisture Diffusivity in Porous Media using Scanning Neutron Radiography. *International Journal of Heat and Mass Transfer.* 36, 1261–1267 (1993)
- Perlo, J., Casanova, F., Blümich, B.: Profiles with microscopic resolution by single-sided NMR. *J. Magn.Reson.* 176, 64–70 (2005)
- Prat, M., Agaësse, T.: Thin porous media. In: Vafai, K. (ed.) *Handbook of Porous Media (Chapter 4)*, 3rd edn. Taylor & Francis, London (2015)
- Qin, C. Z. and Hassanizadeh, S. M.: Multiphase flow through multilayers of thin porous media: General balance equations and constitutive relationships for a solid-gas-liquid three-phase system. *International Journal of Heat and Mass Transfer.* 70, 693–708 (2014)
- Qin, C. Z., Hassanizadeh, S.M.: A new approach to modelling water flooding in a polymer electrolyte fuel cell. *International journal of hydrogen energy.* 40, 3348-3358 (2015)
- Rebai, M., Prat, M.: Scale effect and two-phase flow in thin hydrophobic porous layer. Application to water transport in gas diffusion layers of proton exchange membrane fuel cells. *Journal of Power Sources.* 192, 534-543 (2009)
- Richards, L.A.: Capillary conduction of liquids through porous mediums. *Physics.* Vol. 1, 318-333 (1931)

Chapter 3

- Sole, J.D.: Investigation of water transport parameters and processes in the gas diffusion layer of PEM fuel cells. PhD dissertation, Virginia Polytechnic Institute and State University (2008)
- Spielman, L., and Goren, S. L.: Model for predicting pressure drop and filtration efficiency in fibrous media. *Environ. Sci. Technol.* 2, 279-287 (1968)
- Tafreshi, H.V., Bucher, T.M.: Modeling Fluid Absorption in Anisotropic Fibrous Porous Media. In: Masoodi, R., Pillai, K.M. (eds.) *Wicking in Porous Materials*, pp. 131-159. Boca Raton, CRC Press (2013)
- Tomadakis, M.M., Robertson, T.J.: Viscous permeability of random fiber structures: comparison of electrical and diffusional estimates with experimental and analytical results. *J. Compos. Mater.* 39, 163–188 (2005)
- Van Genuchten, M. Th.: A closed-form equation for predicting the hydraulic conductivity of unsaturated soils. *Soil Sci Soc. Am J.* 44, 892-898 (1980)
- Van Genuchten, M.Th., Pachepsky, Y.: Hydraulic properties of unsaturated soils. In: Gliński, J., Horabik, J., Lipiec, J. (eds.) *Encyclopedia of Agrophysics*. Springer Press, Dordrecht-Heidelberg-London-New York 2011
- Weder, M., Bruhwiler, P.A., Herzig, U., Huber, R., Frei, G., Lehmann, E.: Neutron radiography measurements of moisture distribution in multilayer clothing systems. *Text. Res. J.* 74, 685–700 (2004)
- Weder, M., Bruhwiler, P.A., Laib, A.: X-ray tomography measurements of the moisture distribution in multilayered clothing systems. *Textile. Res. J.* 76(1), 18-26 (2006)
- Zhuang, L., Hassanizadeh, S.M., van Genuchten, M.Th., Leijnse, A., Raoof, A., Qin, C.: Modeling of horizontal water redistribution in an unsaturated soil. *Vadose Zone J.* 15(3), 1 – 11 (2016)

Chapter 4

Continuum-scale modeling of water infiltration in a stack of two thin fibrous layers and their inter-layer space

Abstract

The layer-layer interface impacts through-plane liquid infiltration into a stack of thin porous layers. So, it is essential to better understand how to model unsaturated fluid flow process in such media. Our main objective is to investigate spreading of water in planar direction as well as exchange between two thin fibrous layers. In our previous work, water was injected into the center of two 43 gsm polyester layers with different constant flow rates and was visualized across layers by Fourier-transforming the Nuclear Magnetic Resonance (NMR) signal. In this study, we testify two different models against experimental data. Numerical simulations are performed using the traditional Richards model as well as a new approach called reduced continua model (RCM). In RCM approach, fluid exchange between the two layers is simulated by introducing a piecewise mass transfer coefficient. Effect of imperfect contact is taken into an account using this transfer coefficient. Results of simulations with both approaches are compared to measurements of saturations in stack of two thin polyester layers. Results of RCM simulations show reasonable agreement with laboratory data.

4.1 Introduction

Stacked thin fibrous layers are encountered in many applications, such as, hygiene products (Diersch et al. 2011), polymer electrolyte fuel cells (Qin and Hassanizadeh 2015) and many other productions (Albrecht et al. 2003; Prat and Agaësse 2015). Management of water flow through those thin layers and across their layer-layer interface are of great importance for their performance. Although a thin fibrous layer usually has only a few (10 to 15) pores along its thickness, it is highly porous. Therefore, it is difficult to define representative elementary volume (REV) along the thickness. Most thin fibrous layers are soft. Their pore structures can change considerably under compression (Leisen et al. 2009). Furthermore, the interlayer condition strongly depends on compression pressure. The interlayer condition could dominate mass exchange between layers. Additionally, a clear layer boundary with its neighboring layers cannot be identified easily in stack of fibrous layers. These factors have given rise to many challenges in characterization and modeling of thin fibrous layers.

In the modeling of a thin fibrous layer, it is commonly discretized into a three-dimensional (3D) computational grid, on which 3D flow equations are solved. However, there are several problems with this methodology, such as the failure of the representative elementary volume (REV) concept (García-Salaberri et al., 2018), heavy computational efforts (Hao et al., 2016), and the neglect of layer-layer interfacial effect (Hizir et al., 2010). Since REV cannot be defined for thin fibrous layers, it is difficult to obtain the distribution of “macroscopic” material properties over the thickness and ambiguity arises in interpretation of modeling results. Moreover, for thin layers, with lateral dimension much larger than thickness, discretization of modeling domain leads to high mesh density and accordingly high computational effort. Besides, in multilayer structures, the layer-layer interface could dominate the flow and it is unclear how to incorporate this effect into macroscale equations.

The effect of the interlayer pore space on continuum-scale modeling of unsaturated fluid flow in stacked thin fibrous layers has not received enough attention up to now [Hizir et al., 2010]. To illustrate the concept of interlayer space, side view of μ CT images of fibers of two adjacent thin fibrous layers are shown in Figure 4.1. The gap between two layers is referred to as the interlayer space or interface region

that can be distinguished from the two layers in the enlarged section of this image. Prat and Agaesse (2015) proposed the concept of a third layer that is the transition region forming interface between neighboring layers. They used a pore-network model to investigate influence of interface morphology on invasion patterns in a bilayer porous system. Their results showed that interface region properties lead to completely different fluid distributions at equilibrium in the bilayer system. The third layer concept can be implemented in the traditional continuum scale

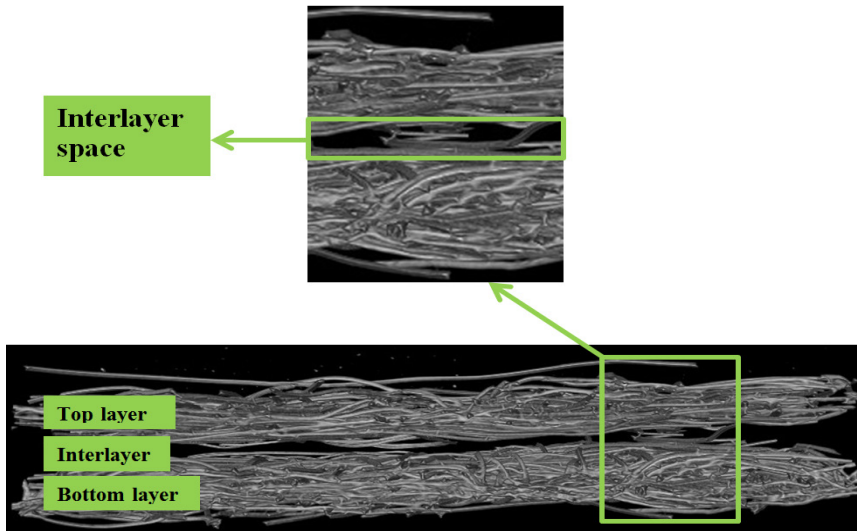


Figure 4.1 μ CT images of two 43-gsm layers on top of each other without compression.

modeling as an additional layer between two thin layers. However, determining the hydraulic properties of a virtual third layer introduces additional complexity. Not only the REV concept doesn't hold for such an interface, but also the virtual third layer thickness cannot be clearly identified.

To resolve the above-mentioned shortcomings, Qin and Hassanizadeh (2014) reformulated the governing equations of multiphase flow and solute transport for a stack of thin fibrous layers. A new model called Reduced Continuum Model (RCM) has been developed in which thin porous layers are treated as a number of 2D continua. Macroscale balance laws are formulated in terms of thickness-averaged properties, which are experimentally measurable. The exchanges of mass, momentum, and energy between two adjacent layers are modeled explicitly.

RCM approach can account for presence of interlayer region in a robust fashion. Its effect is modelled by means of terms for exchange of mass, momentum and energy between the two layers [Qin and Hassanizadeh 2014]. The mass exchange term is assumed to be linearly depending on the pressure difference between two adjacent layers. Furthermore, the mass transfer coefficient appearing in RCM is assumed to depend on saturations as well as material properties of the two layers. This function is very similar to the concept of relative permeability and therefore was linked to saturations of neighboring layers (Qin and Hassanizadeh 2015; Tavangarrad et al. 2018). In general, this function should be determined by laboratory experiments.

In a previous study, we applied RCM to the modeling of liquid transfer from a fully saturated thin layer to a dry layer of identical material (Tavangarrad et al. 2018). The advantages of RCM were demonstrated, in terms of both the treatment of layer-layer interface and computational efficiency. However, in that work, a very small liquid redistribution occurred and the saturation range was limited. Furthermore, saturation distribution profile over the thickness was not measured and local saturation information was not provided. In this study, we employ the RCM to simulate an experiment with a wide range of saturation changes and detailed information about water distribution over the thickness of layers.

The main objective of this study is to test both traditional Richards model and RCM against experimental data obtained in our previous work (Mohebbi et al. 2018) from through-plane liquid infiltration in a stack of two thin fibrous layers. In those experiments, water was fed at a small region in the middle of top layer of a stack of two fibrous layers. Liquid ingress through the two thin fibrous layers and their interface was observed over time. Additionally, one of our research objectives is to characterize the thin fibrous layers and determine their material properties numerically.

This paper is organized as follows. We start with describing measurement method, experimental results, and materials used in our previous work (Mohebbi et al. 2018). Next, we describe characterization of thin fibrous layers, which are used in the modeling study. Analysis of μ CT images from the stack of two layers is also presented in this section. We also show the effect of overburden pressure on the pore structure of stack of two layers and their interface. Additionally, measured hydraulic properties of a single layer and a stack of two layers are compared with

results of pore morphology simulation method. In section 3, two continuum-scale modeling approaches, RCM and Richards model, are introduced briefly. Results of both modeling techniques are presented and compared to measurement data in section 4, which is followed by conclusions in section 5.

4.2 Materials and experiments

In order to investigate the effect of layer-layer interface on unsaturated fluid flow, two identical spunbonded non-woven fibrous layers were stacked together under 0.3 psi overburden pressure. Both were produced in a similar way from polyethylene terephthalate (polyester) fibers. The areal mass density of each fabric is 43 gram per square meter (gsm), and its porosity is around 0.89. Properties of a single 43gsm polyester layer under 0.3 psi overburden pressure are given in Table 4.1.

In our previous study (Mohebbi et al. 2018), two square thin polyester layer samples with dimension of 10 by 10 mm² were placed on top of each other. A Plexiglas plate with a hole in the center was placed on the top of the upper layer in order to impose an overburden pressure of 0.3 psi. The hole had a diameter of 1 mm. It was used for delivering a normal saline solution (consisting of 0.9% NaCl and distilled water) at a constant rate to the top layer using a syringe pump. Two different experiments were performed: i) high flow rate of 30 $\mu\text{l}/\text{min}$ for 60 seconds, ii) low flow rate of 11.4 $\mu\text{l}/\text{min}$ for 160 seconds.

The distribution of saline solution over the thickness of layers and its variation with time was determined from images obtained using mobile single-sided nuclear magnetic resonance (NMR) instrument. The measurement window of NMR had a thickness of 44 μm over the whole layer area. In other words, the signal were averaged over a volume of 4 mm \times 4 mm \times 44 μm . Results are shown in Figure 4.2. There are 15 data points, each assigned to the center of 44- μm slice. The amplitude of NMR signal was assumed to be linearly proportional to the liquid content. As it can be seen in Figure 4.2, the interface region between layers has a lower amount of liquid compared to the two layers. Based on signal intensity profiles, we can identify three different phases of the water infiltration process over time. In the first phase, which takes 12 seconds, water accumulates in the top layer only, with no water entering the interface region and the bottom layer. In the second phase, until about 24 seconds, while water content remains very low in the

Table 4.1 Properties of a compressed single 43-gsm polyethylene terephthalate fibrous layer used in this study

Fiber density [g/cm ³]	Porosity [-]	Fiber radius [μm]	VG formula α [1/Pa]	VG formula n [-]	Thickness [μm]
1.36	0.89	16	0.00197	4.8	310

interface region (centered around 340 μm through the depth), the water saturation increases in the bottom layer. In the last phase, more water pathways are created in the interlayer space and water accumulates in this region too.

We calculated the average saturation of each layer based on the calibration of signals acquired from all slices of a layer and its porosity. Obviously, average saturations of top and bottom layers increase with time, as shown in Figure 4.3a. For the high flow rate experiment, results displayed in this figure show that time lag of saturation buildup in the lower layer is more than 11 seconds. For experiments with lower constant flow rate of 11.4 μl/min, time lag was much

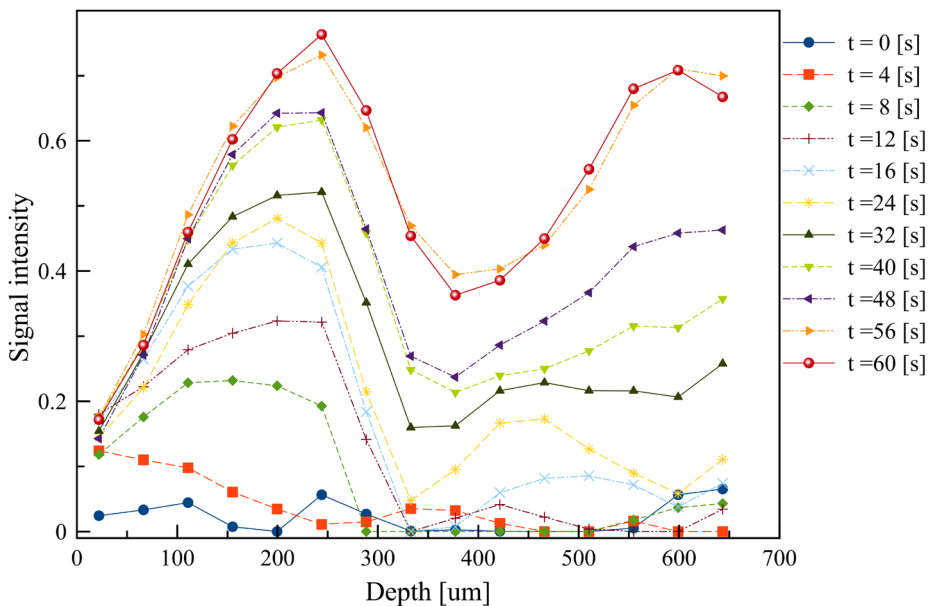


Figure 4.2 Temporal evolution of signal profiles over depth of stack of two polyester layer obtained from NMR measurements when a constant flow rate of 30 μl/min was applied for 60 seconds.

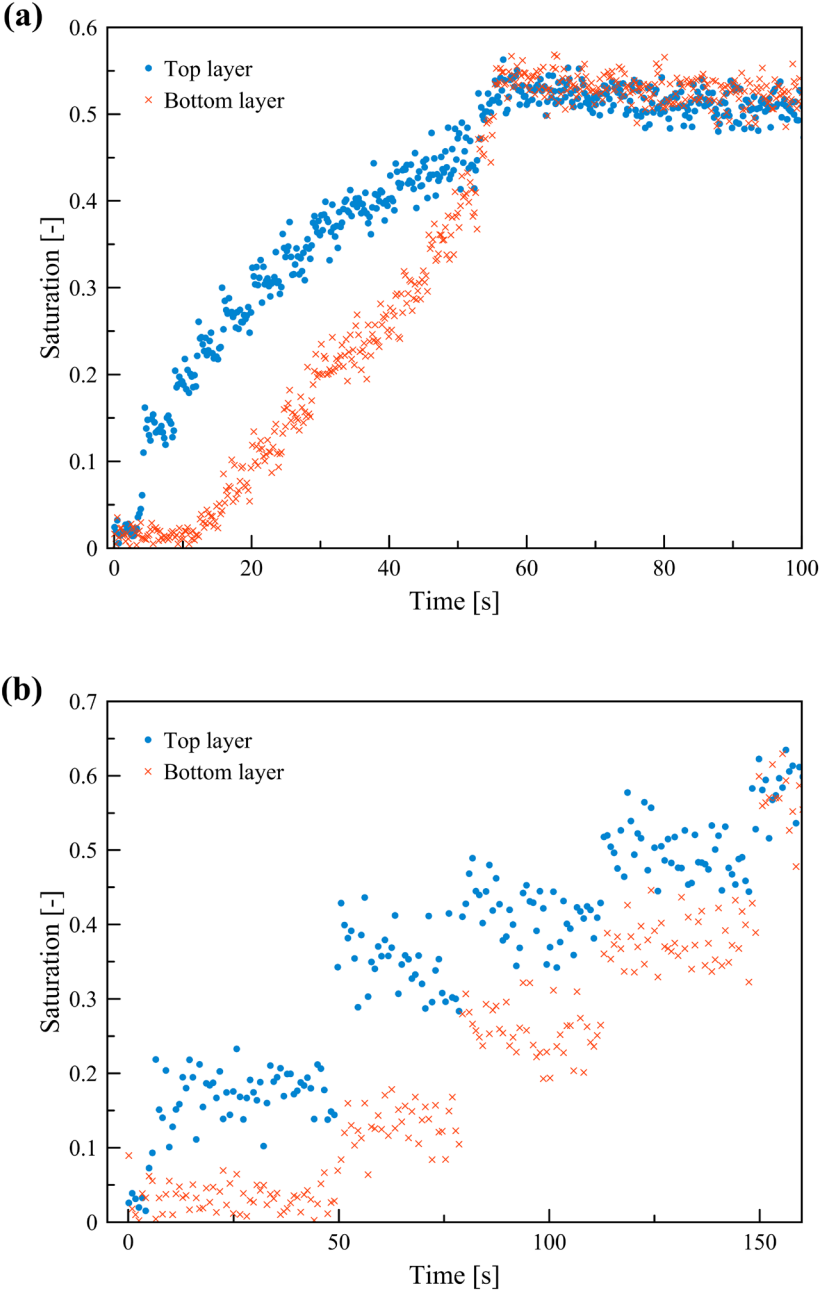


Figure 4.3 Evolution of average saturation of each layer over time obtained from NMR measurements in two different experiments: (a) a constant flow rate of 30 $\mu\text{l}/\text{min}$ applied for 60 seconds (b) a constant flow rate of 11.4 $\mu\text{l}/\text{min}$ applied for 160 seconds.

larger, as expected (Figure 4.3b). This means a longer time is required for saturation build up in the upper layer with this boundary condition. Note that experimental data are more scattered in the lower flow rate experiment, due to the precision of injection pump.

It was qualitatively shown in previous studies on woven fibrous materials (Zhuang et al. 2002) that a saturation-build-up threshold can be defined for the layer-layer mass exchange. Zhuang et al. (2002) stated that this threshold is smaller for a larger overburden pressure. Similarly, Birrfelder et al. (2013) observed longer time delays for water movement from one woven layer to its identical layer when overburden pressure decreased. Among other factors, the saturation-build-up threshold depends on entry pressure of interface region between layers. In other words, nature of interface region imposes a minimum limit for liquid saturation on top layer before entering the bottom layer.

Results shown in Figure 4.3 give us an indication of saturation threshold for the combination of two 43-gsm polyester layers under 0.3 psi pressure. Average saturation of upper layer must reach to approximately 0.25 prior to liquid movement to the lower layer.

Connectivity of two layers is also a critical factor on movement of liquid in the interface region. For instance, our experimental result of water injection into two polyester layers without compression (not presented here) showed that the liquid accumulated in the top layer because only few connection points existed between the two layers. This can be seen in an image of two polyester layers without compression, shown in Figure 4.1. Experimental results discussed briefly in this section are evidences of the role of interface region on the transfer of liquid to the lower layer.

4.3 Characterization approaches

The pore structure of the two layers, with and without overburden pressure, was obtained from images acquired by μ CT scanner (Scanco μ CT50) with an isotropic voxel resolution of four micron. The μ CT images were imported into ImageJ software for thresholding and noise filtration. Figure 4.4 shows top view of a 4×4 mm² section of the stack of two layers after image processing. The dashed red circle shows one of bonding points where fibers are pressed together during

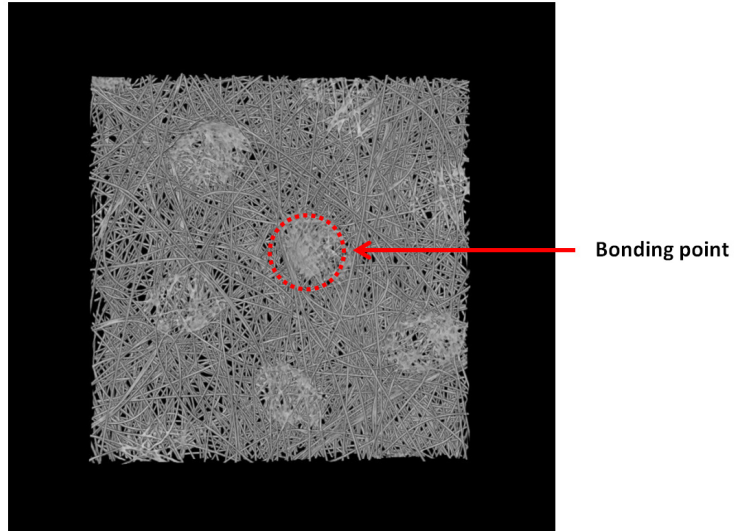


Figure 4.4 Top view image of a $4 \times 4 \text{ mm}^2$ section of a stack of two polyester layers under 0.3 psi overburden pressure. One of bonding points is marked with dashed red circle.

production process. Bonding points are distributed all over the layer in regular pattern. In Figure 4.5, the layer-layer interface can be seen in cross-sectional view of stack of two layers with and without compression. We see a large gap between the two layers in the case of uncompressed layers (Figure 4.5a). Imposing 0.3 psi overburden pressure causes the gap to close, as shown in Figure 4.5b. The large difference between compressed and uncompressed cases are evident in 2D binary

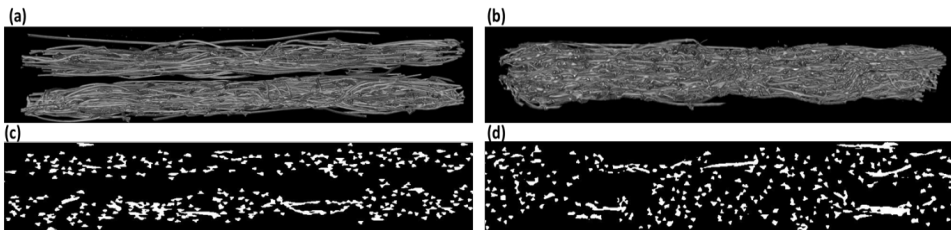


Figure 4.5 Side view of a stack of two polyester layers: (a) without overburden pressure, (b) with 0.3 psi overburden pressure. A 2D binary image of cross sectional cut of stacked layers: (c) without overburden pressure, (d) with 0.3 psi overburden pressure.

images (Figure 4.5c and 4.5d). However, there are still large pores in the interface region even after compression (Figure 4.5d).

The variation of fiber content along the layers thickness was determined using a MATLAB code developed in-house. The code uses binary images as an input and results are shown in Figure 4.6. As it can be seen, the fiber content varies non-uniformly along the thickness of layers. It has a bell shaped form for both layers.

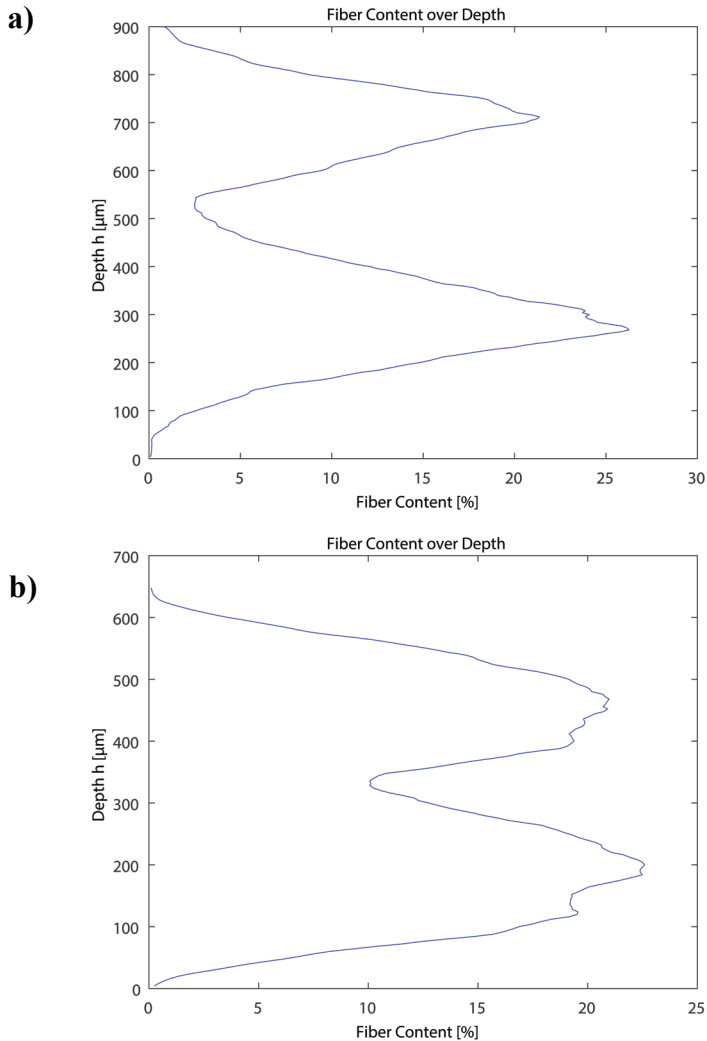


Figure 4.6 Fiber content variation over thickness of two polyester layers: (a) without overburden pressure, (b) with 0.3 psi overburden pressure.

The data is used to calculate the variation of porosity over the thickness. As a result of overburden pressure, both porosity and thickness of stack are reduced. This is because of the layer deformability, which results in a decrease in porosity of layers and reducing interface region.

The thin 43-gsm polyester layer used in this study consists of small pores in its middle regions and larger pores near surfaces. This results in a smooth variation of the fiber content from zero to its maximum value along the thickness (Figure 4.6). The bonding points (marked in Figure 4.4) contributes to a higher fiber content in the middle. The very low fiber content at the surface of each layer corresponds to a few fibers sticking out of the layer. This will raise a question about the exact thickness of a thin layer. Among other factors, the nominal thickness of a single layer of fabric depends on the layer surface roughness, fabric wrinkles, and bonding points. One simple way to approximate average thickness of a fabric under overburden pressure is to place it between two flat surfaces, and then measure the distance between them. The average thickness of a single 43gsm polyester layer and a stack of two layers were obtained in this fashion under different overburden pressures (Figure 4.7). In our numerical studies, the stack of two layers is exposed to 0.3 psi pressure. Estimated thickness for the stack of two

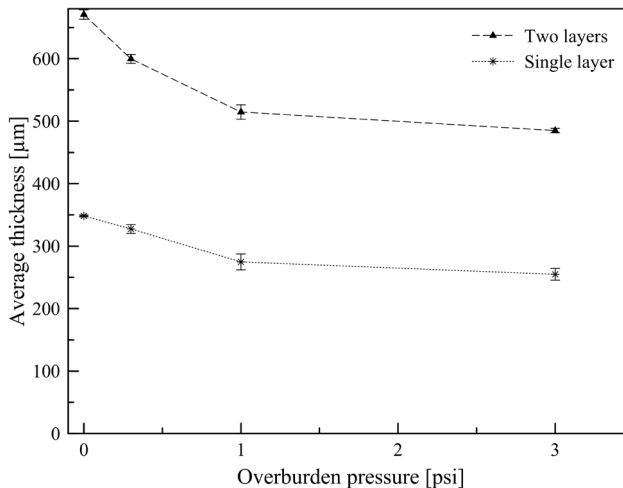


Figure 4.7 Comparison between average thickness of single and two polyethylene terephthalate layers under different overburden pressures. Standard deviation represents duplicate measurements.

layers under this condition is $600 \pm 6 \mu\text{m}$. Alternatively, one can determine the thickness of two layers from image analysis results provided in Figure 4.6. Assuming the layer surface to start at fiber content of zero, the thickness of stack of two layers is equal to $640 \mu\text{m}$ under compressed conditions. Difference in above-mentioned values of stack's thickness is less than 10%, which is within material production variability.

Hydraulic properties of the thin fibrous layers in this study were determined both numerically and experimentally. The capillary pressure-saturation relationship for a single 43-gsm polyester layer was measured with the autoporosimetry technique developed for fibrous layers by Miller and Tomkin (1994). Measurements were performed on a circular piece of a sample with the diameter of 5 cm. Only imbibition experiments were performed. Measured data points were fitted using van Genuchten (1980) formula (Figure 4.8). The error bars are based on the duplicate measurements. Fitting parameters and other measured properties are listed in Table 4.1. Based on our previous experimental study on capillary

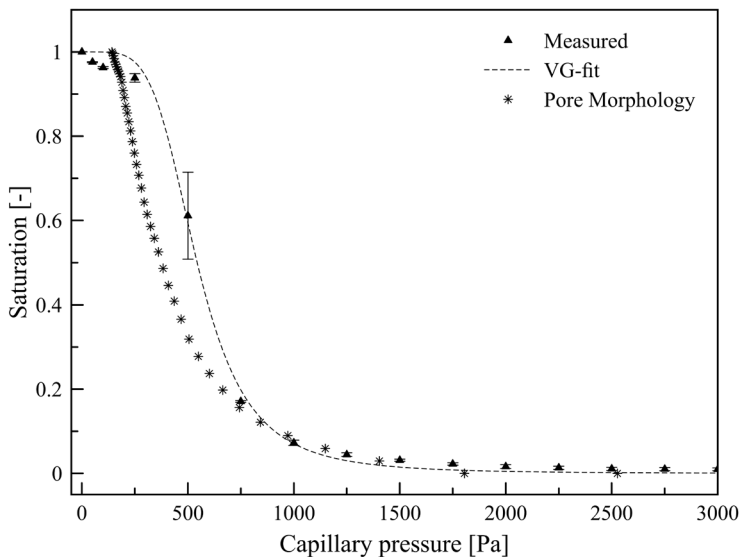


Figure 4.8 Measured and calculated imbibition capillary pressure-saturation data points for a single compressed polyethylene terephthalate layer. Experimental data points are fitted with VG formula. Error bars represent standard deviation in duplicate measurements.

pressure-saturation ($P_c(s)$) relationship for thin fibrous layers, doubling the number of layers had little impact on this relationship. Clearly, with the current measurement setup, we were not able to characterize the interface region separately. One possible way to obtain the $P_c(s)$ relationship of interface region is to combine the single sided low-field NMR device with the autoporosimetry in order to measure the water content variation over the thickness of a stack of layers and their inter-layer space at any given pressure step, at equilibrium. But, this characterization technique is out of the scope of current study.

As an alternative to measurements, we have used the pore morphology simulation method to obtain capillary pressure-saturation relationship for a single layer, sub-regions of a layer or the interface region between two layers. Pore morphology method is a quasi-static geometric approach that was developed by Hazlet (1995) and improved later by Hilpert and Miller (2001). It has been used for obtaining capillary pressure-saturation relationship for fibrous materials in previous studies (Tafreshi and Bucher 2013).

The μ CT images shown in Figure 4.5b were used as input for specifying the pore space. The pore morphology method was used to determine material properties of a stack of two polyester layers based on their μ CT images. Characterization of the stack is based on three different modeling approaches. In first modeling approach, model 1, we assume two identical homogeneous domains are in contact with each other. So, in this case, it is sufficient to find properties of a single layer only. In model 2, the modeling domain consists of three homogeneous domains: in addition to upper and lower layers, we consider the interface as a third virtual layer. In the third approach, the modeling domain is divided into 14 different subdomains with equal thicknesses. The main goal is to see how variation of properties along the thickness of two layers can affect numerical simulation results. Moreover, measurement results of each sensitive slice can be compared with numerical results. We use all three modeling approaches with traditional Richards model while the model 1 is the only subdivision approach employed for RCM.

A quasi-static imbibition simulation was run for each modeling subdomain using pore morphology technique. Top and bottom boundaries of the subdomain were set to be in contact with wetting and non-wetting reservoirs, respectively. Properties of fluid phases as well as their surface tension and contact angle with the solid phase were given as input parameters in the Geodict (Math2Market

GmbH). It should be noted that the contact angle was assumed to be 80 degrees and constant in this approach. The surface tension between water and air was considered to be constant and equal to 0.072 N/m.

In the model 1 approach, we cut the stack of two layers images into two subdomains with equal thickness namely top and bottom layer. Computed capillary pressure-saturation data points for top and bottom layers are shown in Figure 4.9. Also shown in this figure are pore morphology results of the whole stack of two layers. The pore morphology method gives similar curves for top layer, bottom layer, and double layers. Consequently, doubling the number of layers did not seem to affect the curves drastically. Discrepancies between the numerical and experimental results in this case study (Figure 4.8) are due to physical phenomena that are missed in pore morphology method. For instance, the effect of surfactant wash-off during imbibition process, and corresponding changes in surface tension and contact angle, could not be taken into account by the current model. Other hydraulic properties of top and bottom layers are listed in Table 4.2. Both intrinsic permeability and relative permeability are determined using Geodict software package. Results of intrinsic permeability values obtained from solving Stokes equation are in good agreement with values of Jackson and James (1986) empirical equation (Table 4.2). Calculated relative permeability data points match satisfactorily with suggested formula of Van Genuchten (1980) for relative permeability function (See Appendix A). Hence, we used van Genuchten fitting parameters to specify relative permeability function in this study.

Next, according to the model 2 approach, a virtual third layer with the thickness of 44 μm was cut from the middle part of the stack of images and characterized using pore morphology method. Results are shown in Figure 4.10 and compared with experimental data points. Lower capillarity and higher porosity for virtual third layer were computed comparing to the above-mentioned results for top and bottom layers (Table 4.2).

For the model 3, the modeling domain was divided into fourteen subdomains in order to investigate variation of capillary pressure-saturation curve along the thickness of a stack of two layers. These subdomains are numbered from upper surface of top layer to lower surface of bottom layer. As listed in Table 4.3, the porosity varies non-uniformly from top subdomain to bottom one. The values of α parameter of VG fits, and thus, entry pressures of subdomains correlate with

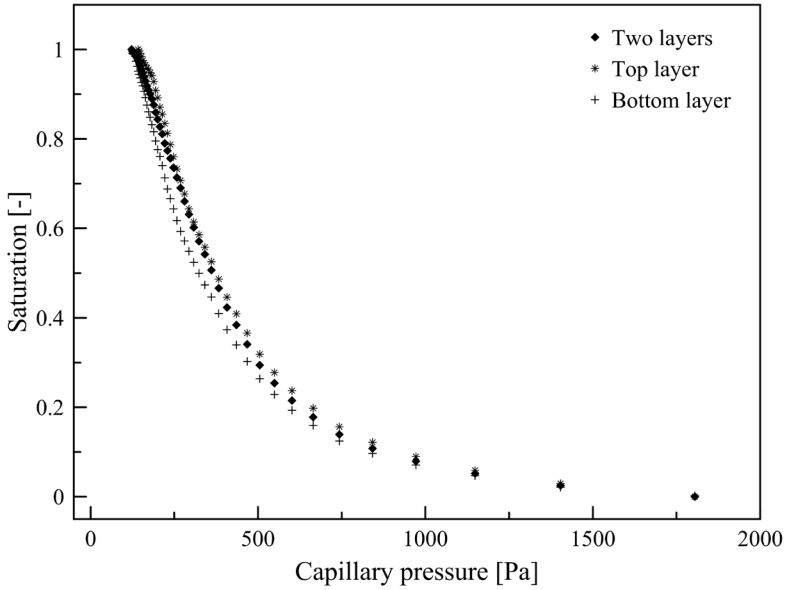


Figure 4.9 Capillary pressure-saturation data points obtained from pore morphology method for top layer and interface region of compressed stack of two polyethylene terephthalate layers.

Table 4.2 Properties two polyethylene terephthalate fibrous layers used in this study obtained from simulations with Geodict

Parameter	Top layer	Bottom layer	Stack	Interface region
Porosity, φ [-]	0.889	0.902	0.895	0.924
K [m^2], Jackson & James	4.4e-10	5.5e-10	4.9e-10	8.3e-10
K_{xx} [m^2], Geodict	5.0e-10	7.7e-10	8.7e-10	1.8e-10
K_{zz} [m^2], Geodict	2.7e-10	3.5e-10	3.1e-10	3.03e-9
VG model, α [1/Pa]	0.0026	0.0026	0.0026	0.0043
VG model, n [-]	4	4	4	3.2
Thickness [μm]	316	316	632	44

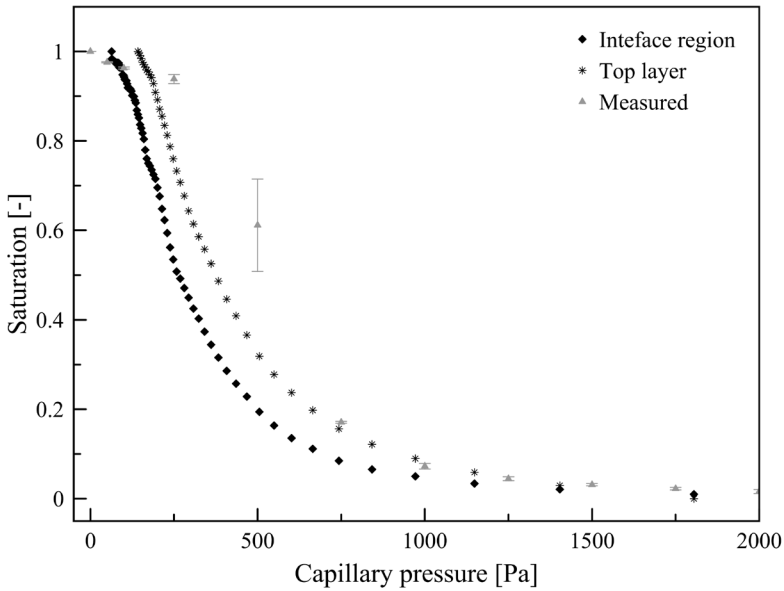


Figure 4.10 Capillary pressure-saturation data points obtained from pore morphology method for top layer and interface region of a compressed stack of two polyethylene terephthalate layers. Measured data points are shown too.

Table 4.3 Properties of different 44- μm thick subdomains of two polyethylene terephthalate fibrous layers used in this study.

# Domain	Porosity [-]	K [m^2] Jackson & James	Kxx [m^2] Geodict	Kzz [m^2] Geodict	VG formula α [1/Pa]	VG formula n [-]
1	0.97	4.9e-09	4.9e-9	2.9e-8	0.0144	3.2
2	0.91	6.9e-10	1.7e-10	2.9e-9	0.0043	2.7
3	0.87	3.2e-10	7.8e-11	1.3e-9	0.0027	2.9
4	0.85	2.4e-10	5.6e-11	6.9e-10	0.0024	2.9
5	0.84	2.2e-10	5.6e-11	8e-10	0.0023	2.9
6	0.86	3.0e-10	7.3e-11	1.4e-9	0.0027	2.9
7	0.90	5.5e-10	1.4e-10	3.5e-9	0.004	2.7
8	0.92	7.8e-10	1.8e-10	2.4e-9	0.0045	2.7
9	0.87	3.6e-10	8.3e-11	1.4e-9	0.0034	2.7
10	0.85	2.6e-10	5.8e-11	7.3e-10	0.0034	2.7
11	0.85	2.4e-10	5.3e-11	8e-10	0.0026	2.9
12	0.88	3.6e-10	7.9e-11	1.4e-9	0.0029	2.9
13	0.93	8.6e-10	2e-10	5.1e-9	0.0048	2.7
14	0.98	5.2e-09	4.4e-9	2.8e-8	0.0144	3.2

porosity variations over subdomains. Intrinsic permeability of all subdomains are summarized in Table 4.3.

4.4 Numerical approaches

4.4.1 Governing equations

We present equations for traditional Richards model and Reduced continua model (RCM). In this study, gravity is assumed to be negligible due to the small thickness of the layers. Thus, Richards equation can be written as:

$$\frac{\partial(\varphi S^w)}{\partial t} - \nabla \cdot \left(\frac{k^r K}{\mu^w} \nabla P^w \right) = 0 \quad (4.1)$$

where φ is porosity, S^w is saturation of the wetting phase, K is intrinsic permeability, k^r is relative permeability of the wetting phase, μ^w is dynamic viscosity of the wetting phase, and P^w is the wetting phase pressure, which can be linked to capillary pressure P^c as follows:

$$P^w = -P^c(S^w) \quad (4.2)$$

This $P^c(S^w)$ relationship and unsaturated relative permeability functions are given by van Genuchten (1980) formulas as follows:

$$\begin{cases} P^c(S^w) = \frac{1}{\alpha} (S^{w-1/m} - 1)^{1/n}, \\ k^r(S^w) = S^{w0.5} (1 - (1 - S^{w1/m})^m)^2 \end{cases} \quad (4.3)$$

where α and n are fitting parameters, $m = 1 - 1/n$. Note that in this formulation, due to the very large porosity of the samples, no residual air saturation has been considered.

In standard Richards model, the computational domain needs to be discretized in both in-plane and through-plane directions. This implies existence of Representative Elementary Volume (REV) in all directions. However, since the number of pores along thickness of a thin porous layer is not sufficient to define REV in its through-plane direction, the applicability of Richards model for such layers is questionable. Alternatively, Reduced Continua Model was developed based on thermodynamical approach to resolve this shortcoming (Qin and Hassanizadeh 2014). In this model, all properties are averaged over the thickness

and REV is defined in in-plane direction only. For RCM, the mass conservation equation for water transport in layer i of a stack of layers can be written as follows:

$$\frac{\partial(b\rho^w\varphi S^w)}{\partial t}\Big|_i - \nabla_h \cdot \left(b\rho^w \frac{k^r K}{\mu^w} \nabla_h P^w \right)\Big|_i = Q_T^w|_i + Q_B^w|_i \quad (4.4)$$

where $Q_T^w|_i$ and $Q_B^w|_i$ denote influx and outflux of water for layer i , respectively and b is the layer thickness. Flux between top and bottom layers are assumed to be related to the difference in pressures as follows:

$$Q_B^w|_1 = - Q_T^w|_2 = \Pi_m(P_2^w - P_1^w) \quad (4.5)$$

where Π_m is the coefficient of mass transfer between two adjacent layers. This coefficient is specific to the two neighboring layers but also accounts for the nature of contact between them. It is considered to be a function of saturations via their relative permeability. More information about the exchange coefficient is provided below.

4.4.2 RCM approach

One of the main challenges in modeling multiple layers arrangement is how to consider the effect of layer-layer interstices space during fluid flow. This is due to the fact that the properties of that region depend not only its porosity but also on the fiber connectivity of two neighboring layers, particularly in low saturation. This factor can be determined based on interpenetration of fibers, fabrics setting and fibers orientation of the two layers. connectivity of fibers is a function of external pressure applied on layers. It will facilitate water movement from one layer to another one. Moreover, fluid flow movement dominates in favor of fiber direction. For fabrics with planar fibers direction, there is less chance for water exchange between the two layers at low saturation. Additionally, for fabrics with bonding points, how fabrics face each other results in different fluid flow conditions. A comprehensive sensitivity study needs to be done to evaluate significance of each factor. Based on previous experimental results in the literature [Mohebbi et al.2018], the saturation should build up in one layer to overcome the interlayer space resistance. In RCM approach, we lump all interface effect in mass transfer coefficient, which is assumed to be a function of effective permeability of both layers. In particular, we propose the following formula:

$$\Pi_m = \begin{cases} 0 & S_1^w < S_{th}^w = 0.25 \\ \frac{2}{b_1 + b_2} \rho^w \frac{\overline{K}_t}{\mu^w} \lambda & S_1^w > S_{th}^w = 0.25 \end{cases} \quad (4.6)$$

$$\overline{K}_t = \left(\frac{b_1 + b_2}{b_2 K_1 k_1^r + b_1 K_2 k_2^r} K_1 k_1^r K_2 k_2^r \right) \quad (4.7)$$

Here λ is a dimensionless factor that accounts for the condition of interface region. It varies depending on over burden pressure. S_{th}^w is a local saturation threshold that should be built up in the upper layer before liquid penetration into the lower layer can start. This value was chosen based on experimental observation in our earlier study [Mohebbi et al.2018] explained in section 2. After conducting pathways between the two layers are established, the mass transfer coefficient is assumed to be related to the harmonic mean of effective permeabilities of the two layers weighted by their thickness, as given by equation 4.7. This empirical formula was proposed by Tavangarrad et al (2018). As they suggested, a percolation threshold was assumed for relative permeability function in which values of this functions was reduced significantly in saturations below 0.25. The coefficient λ is introduced to account for speed of fluid exchange between the two layers and takes values between 0 and 1. As an example, our preliminary experimental result for two polyester layers without compression showed that liquid remained on top layer. In that experiment, $S_{th}^w = 1$ and $\lambda = 0$. Increasing overburden pressure leads to lower saturation threshold and higher λ values.

Alternatively, we can break the second-piece of exchange function (equation (4.6)) into two parts as follows:

$$\Pi_m = \begin{cases} 0 & S_1^w < 0.25 \\ 1.8 * 10^{-8} & S_1^w > 0.25, S_2^w < 0.25 \\ \frac{2}{b_1 + b_2} \rho^w \frac{\overline{K}_t}{\mu^w} \lambda & S_1^w > 0.25, S_2^w > 0.25 \end{cases} \quad (4.8)$$

Here, we treat the lower layer differently before S_2^w reaches 0.25. This means for saturations up to 0.25 in the bottom layer the exchange coefficient was assumed to be a constant value before the harmonic mean can be activated.

4.5 Numerical implementation

4.5.1 Richards model

In this study, Feflow software (DHI Wasy, Berlin) was used to solve Richards equation for liquid flow in a stack of two thin layers. The two-layer 3D domain was discretized in three different ways, as explained earlier in section 3. First, they were considered to be two homogeneous subdomains, corresponding to the two layers, with properties given in Table 4.2. They were discretized into a mesh of 10890 hexahedral elements. Auxiliary computations showed that we had mesh-independent results. In the second approach, we considered three homogeneous layers, with the 44 μm third layer representing the interface region. In the third approach, the two layers and their interface region were subdivided into 14 homogeneous slices, with properties given in Table 4.3. A mesh of 199962 hexahedral elements was generated for this computational domain. Equations (4.1-4.3) together with applied boundary condition were solved numerically for all above-mentioned cases using finite element solver with standard iterative schemes.

4.5.2 Reduced continua model

Equations (4.2), (4.4)-(4.7) were coded in COMSOL. The two layers were discretized into two 2D domains using a total of 400 tetrahedral mesh elements. Obviously, one major advantage of the RCM approach is that the computational effort is significantly reduced.

4.5.3 Boundary conditions

For traditional Richards model, the stack of two layers was simulated as a three dimensional domain. All boundaries were considered to be no flux boundaries except a circular area of 1 mm in diameter in the middle of top surface of upper layer, where water was introduced at a constant rate. There, a uniform liquid velocity of 0.6 mm/s normal to the boundary was specified.

For the RCM approach, the stack of two layers was modeled as two interacting two dimensional domains. The inlet was specified as the source term $Q_T^W|_1$, but of course only over circular area of 1 mm in diameter in the middle of top layer.

Everywhere else $Q_T^W|_1$ was set equal to zero. Also, $Q_B^W|_2$ was set to zero for all (x, y) points.

4.6 Results and discussion

Results of 3D Richards model is averaged for each mesh layer through the thickness to obtain 1D depth profiles for the high flow rate experiment (30 $\mu\text{l}/\text{min}$). Solving traditional Richards equation result in large differences in the 1D saturation depth profiles of three subdivision approaches at $t=10$ seconds as plotted in Figure 4.11. As the two layers are basically the same in model 1, the Richards model predicts the water infiltration to be like a front and everywhere reaching an almost uniform low saturation in 10 seconds. Result of model 3 approach, consisting 14 subdomains, is the only one that preserves bell shape form similar to experimental results. But, water is distributed almost equally between two layers in this modeling approach while the measurement data shows the top layer saturation is much higher than the bottom layer after 10 seconds.

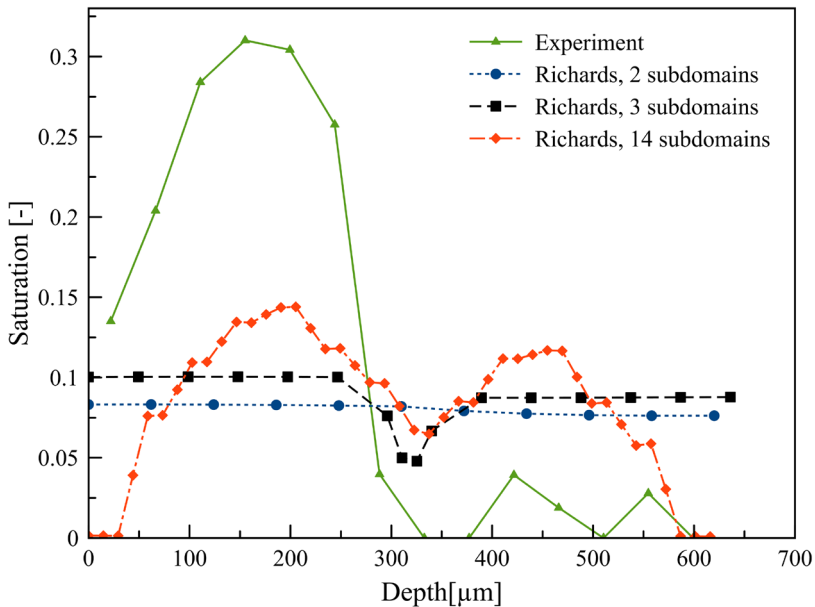


Figure 4.11 Saturation profiles at $t=10$ seconds over the depth of two layers. NMR measurement and the Richards model results are compared for a case that constant flow rate of 30 $\mu\text{l}/\text{min}$ was applied in inlet boundary.

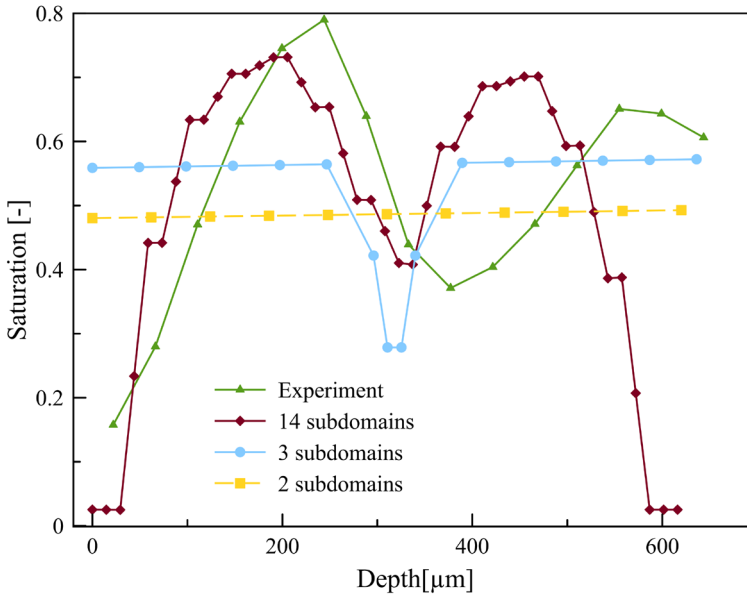


Figure 4.12 Saturation profiles at $t=60$ seconds over the depth of two layers. NMR measurement and the Richards model results are compared for a case that constant flow rate of $30 \mu\text{l}/\text{min}$ was applied in inlet boundary.

Results of Richards model for high flow rate experiment ($30 \mu\text{l}/\text{min}$) at the end of fluid injection ($t=60$ seconds) are shown in Figure 4.12. The model 3 is the only one that can predict satisfactorily the saturation profile of the top layer at $t=60$ seconds.

Next, we compare modeling and experimental results for the change of average saturation of top and bottom layer with time, as shown in Figure 4.13. We can see that results of Richards model for all three characterization schemes are drastically different. In all cases the average saturations of both layers start to increase as soon as the experiment starts. Including heterogeneity of layers has only marginal effect on the results.

Results of RCM for saturation averaged over each layer are shown in Figure 14. We can see that experimental data are very well simulated. We found negligible difference in results for the two different formulations of the mass transfer coefficients as given by Equations 4.6 and 4.8 (compare Figure 4.14.a and 4.14.b). This is because RCM enables us to define mass transfer coefficient between layers. Clearly, the threshold defined in first piece of mass transfer functions controls time

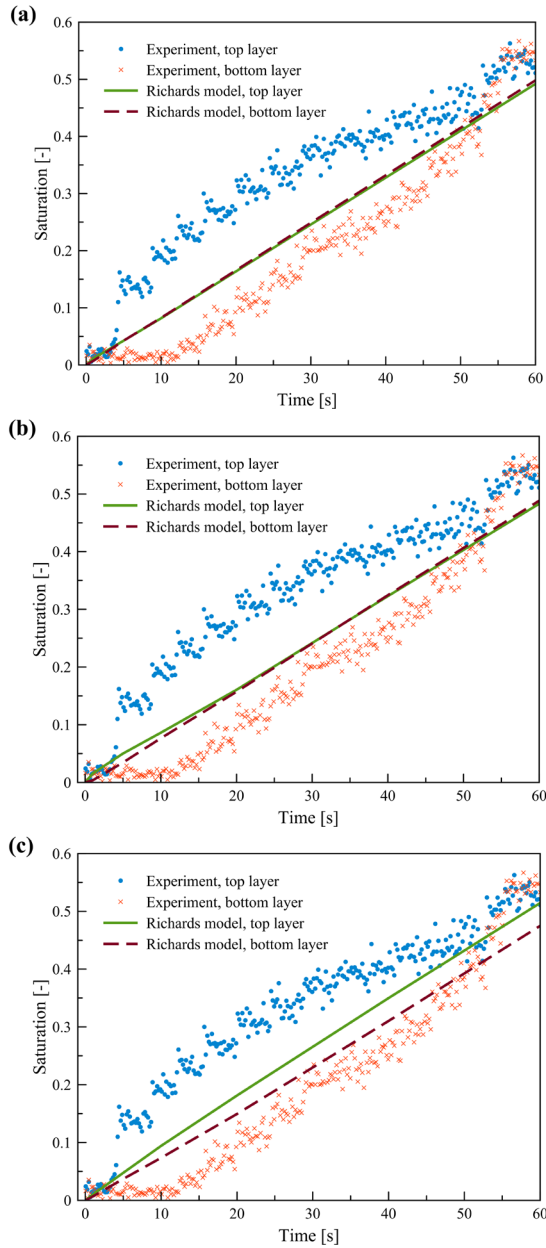


Figure 4.13 Comparison of evolution of average saturation of each layer over time obtained from NMR measurements and Richards model with three different characterization approaches: (a) two homogeneous subdomains, (b) three homogeneous subdomains (with the middle domain representing interface region), (c) fourteen homogeneous subdomains.

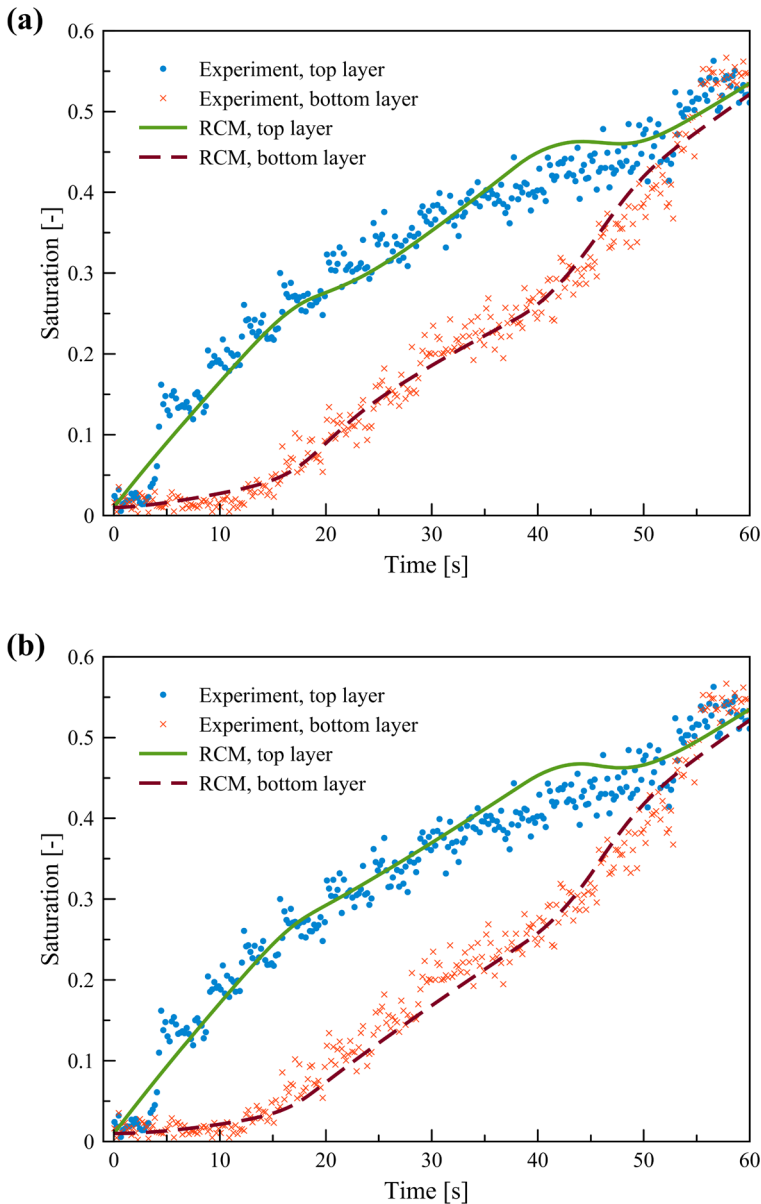


Figure 4.14 evolution of average saturation of each layer in a stack of two thin layers over time obtained from NMR measurements result and Reduced continua model when constant flow rate of $30 \mu\text{l}/\text{min}$ was applied for two cases: (a) first formulation for mass exchange (Equation 4.6) was used in RCM and (b) second formulation for mass exchange (Equation 4.8) was used in RCM.

delay of liquid movements towards the bottom layer. Once water reaches the bottom layer, water saturation of both layers is increased in parallel with time up to 40 seconds. In the last phase, if saturation goes beyond 0.25 for both layers, defined harmonic mass transfer speeds up exchange of liquid in between the layers.

The ability of RCM approach for simulating flow in stack of two layers was further confirmed by simulating experiment that was performed a flow rate of $11.4 \mu\text{l}/\text{min}$, without changing values of material coefficients. In Figure 4.15, RCM results of variation of average saturation of each layer with time are compared to experiment. Good agreement was reached between RCM and experimental results. The time lag increases for the saturation build-up in the lower layer with this lower flow rate experiment. This study evidenced role of interface on impeding water transport to lower layer, which is reproduced in numerical solution by implementing saturation buildup threshold and λ coefficient in mass transfer coefficient. Imperfect contact was included in exchange coefficient by setting $\lambda = 0.01$. This value works perfectly for the current layer-layer setting for different inlet boundary flowrates.

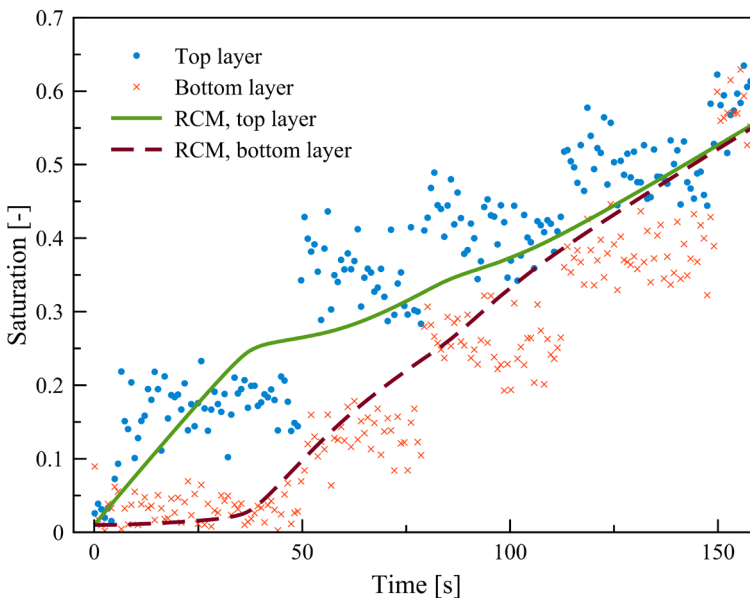


Figure 4.15 evolution of average saturation of each layer in a stack of two thin layers over time obtained from NMR measurements result and Reduced continua model when constant flow rate of $11.4 \mu\text{l}/\text{min}$ was applied.

4.7 Conclusion

In this study, water infiltration into a stack of two thin fibrous layers is investigated numerically. Traditional Richards model and Reduced Continua Model are employed to simulate evolution of saturation with time and depth. Results are compared to experimental data.

Traditional Richards model results cannot reveal depth saturation distribution profile when measured properties of each single layer assigned to its mesh layers. More importantly, impeding water movement due to the interface effect cannot be determined by using the traditional Richards model. However, in RCM, effect of interface is embedded in mass transfer coefficient. This feature enabled the RCM to reproduce experimental results under different boundary conditions. Results of this research proves the ability of RCM in trans-planar fluid flow in a stack of thin fibrous layers compared to the traditional Richards model in terms of layer-layer mass exchange effect and computational effort.

4.8 Appendix A: Relative permeability function of a thin fibrous layer using pore morphology method and van Genuchten fitting parameters

To find relative permeability function, we first implemented pore morphology method to obtain wetting phase distribution in each capillary pressure. Then, a single-phase simulation ran by solving stokes equation in those voxels occupied by wetting phase. Relative permeability data points obtained by this approach are compared with van Genuchten function, which is calculated based on parameters appear in $P^c(S^w)$ relationship. As shown in Figure 4.A-1, a good agreement was achieved between calculated data points and estimated VG function. Although results of the capillary pressure-saturation for a single 43-gsm layer were not depending on flow direction, the relative permeability function varies from in-plane to through-plane direction. However, this discrepancy had negligible effect on final simulation results. Therefore, we decided to consider VG formula for relative permeability in equation 4.3 for all of the modeling case studies in this chapter.

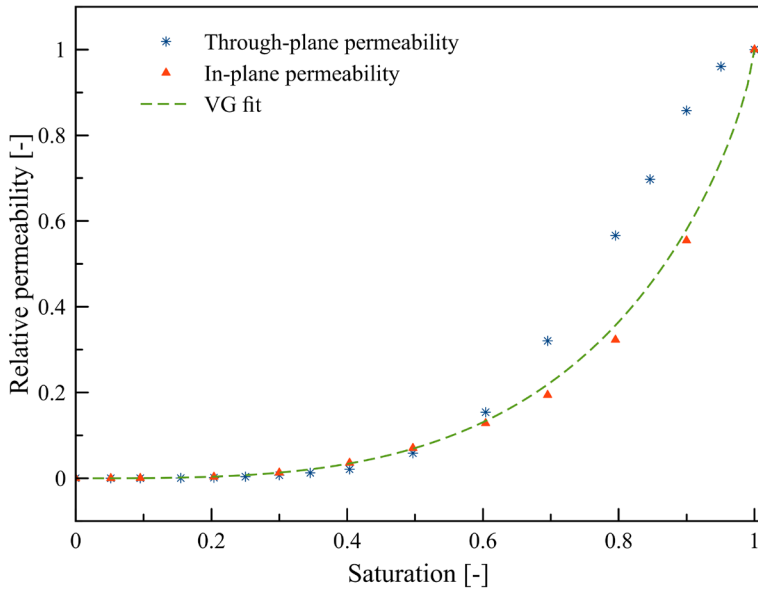


Figure 4.A-1 relative permeability data points obtained from pore morphology method combined with Stokes equation for a compressed polyethylene terephthalate layer. VG-fit curve is based on Muallem-van Genuchten formula and calculated out of fitting parameters appear in the capillary pressure saturation relationship.

References

- Albrecht, W., Fuchs, H., Kittelmann, W.: *Non-woven Fabrics: Raw Materials, Manufacture, Applications, Characteristics, Testing Processes*. Wiley (2003)
- Ceballos, L., Prat, M., Duru, P.: Slow invasion of a non-wetting fluid from multiple inlet sources in a thin porous layer. *Phys Rev E*. 84, 056311 (2011)
- Diersch, H. J. G., Clausnitzer, V., Myrnyy, V., Rosati, R., Schmidt, M., Beruda, H., Ehrnsperger, B. J., Virgilio, R.: Modeling Unsaturated Flow in Absorbent Swelling Porous Media: Part 2. Numerical Simulation, *Transport in Porous Media*, 86(3) (2011)
- Hao, L., K. Moriyama, W. Gu, and C.-Y. Wang: Three Dimensional Computations and Experimental Comparisons for a Large-Scale Proton Exchange Membrane Fuel Cell, *Journal of The Electrochemical Society*, 163(7) (2016)
- Hazlett, R.D.: Simulation of capillary-dominated displacements in microtomographic

- images of reservoir rocks. *Transport in Porous Media*. 20-21 (1995)
- Hilpert, M., and Miller, C. T.: Pore-morphology-based simulation of drainage in totally wetting porous media. *Advances in Water Resources*. 24 (3/4), 243–255 (2001)
- Hizir, F. E., S. O. Ural, E. C. Kumbur, and M. M. Mench: Characterization of interfacial morphology in polymer electrolyte fuel cells: Micro-porous layer and catalyst layer surfaces, *Journal of Power Sources*, 195(11), 3463–3471 (2010)
- Jackson, G. W., James, D. G.: The permeability of fibrous porous media. *Can. J. Chem. Eng.* 64, 362-374 (1986)
- Leisen, J., Beckham, H.W.: Fluid Distribution and Movement in Engineered Fibrous Substrates by Magnetic Resonance Microscopy *Magnetic Resonance Microscopy: Spatially Resolved NMR Techniques and Applications*. 399-419 (2009)
- Miller, B., Tyomkin, I.: Liquid porosimetry: new methodology and applications. *J Col Int Sci*. 62,163-170 (1994)
- Mohebbi, B., Tavangarrad, A.H., Clausen, J., Blümich, B., Hassanizadeh, S. M., Rosati, R.: Revealing how interfaces in stacked thin fibrous layers affect liquid ingress and transport properties by single-sided NMR. *Journal of Magnetic Resonance*. 294, 16-23 (2018)
- Prat, M., Agaësse, T.: Thin porous media. In: Vafai, K. (ed.) *Handbook of Porous Media* (Chapter 4), 3rd edn. Taylor & Francis, London (2015)
- Qin, C. Z. and Hassanizadeh, S. M.: Multiphase flow through multilayers of thin porous media: General balance equations and constitutive relationships for a solid-gas-liquid three-phase system. *International Journal of Heat and Mass Transfer*. 70, 693–708 (2014)
- Qin, C. Z., Hassanizadeh, S.M.: A new approach to modelling water flooding in a polymer electrolyte fuel cell. *International journal of hydrogen energy*. 40, 3348-3358 (2015)
- Tafreshi, H.V., Bucher, T.M.: Modeling Fluid Absorption in Anisotropic Fibrous Porous Media. In: Masoodi, R., Pillai, K.M. (eds.) *Wicking in Porous Materials*, pp. 131-159. Boca Raton, CRC Press (2013)
- Tavangarrad, A.H., Mohebbi, B., Hassanizadeh, S. M., Rosati, R., Clausen, J., Blümich, B.: Continuum-scale modeling of liquid redistribution in a stack of thin hydrophilic fibrous layers. *Transport in Porous Media*. 122, 203-219 (2018)
- Van Genuchten, M. Th.: A closed-form equation for predicting the hydraulic conductivity of unsaturated soils. *Soil Sci Soc. Am J*. 44, 892-898 (1980)
- Zhuang, Q., Harlock, S.C., Brook, B.D.: Transfer Wicking Mechanisms of Knitted Fabrics Used as Undergarments for Outdoor Activities. *Textile. Research. Journal*. 72, No. 8, 727–734 (2002)

Chapter 5

Experimental and numerical study of dynamic non-equilibrium in a thin non-woven fibrous layer

Abstract

In this study, the applicability of statically measured hydraulic properties of a compressed single thin non-woven fibrous layer is investigated under dynamic fluid flow conditions. For this purpose, autoporosimetry techniques were used to perform both quasi-static and dynamic inflow/outflow experiments. In the quasi-static experiments, the pressure gradient was changed incrementally to identify static water retention parameters. The applicability of these measured hydraulic parameters under static condition was examined for modeling dynamic inflow/outflow experiments in which a large pressure step was applied instantaneously. Six homogeneous non-woven fibrous layers with different structure and hydraulic properties were selected, with three of the layers being bonded mechanically or thermally at selected points (bonding points). Results of modeling dynamic inflow using a traditional two-phase flow Darcy model were in good agreement with laboratory data for materials without bonding points (without calendar bonding), which had perfect contact with a saturated hydrophilic membrane. However, for materials with bonding points, the starting time of the inflow experiment had a clear time delay comparing to the two-phase flow modeling results. A recently developed model for a stack of thin fibrous layers, called the Reduced Continua Model (RCM), was employed to account for the effects of interlayer space between a thin fibrous layer and a hydrophilic membrane. The interlayer effect, which is embedded in a mass transfer function for flow between the membrane and thin layers, can explain the above-mentioned time shift. A perfect match between the experimental and modeling results of layers with bonding points was achieved using a low interface transfer rate coefficient for the mass transfer function in the reduced continua model. Results of dynamic outflow experiments satisfactory matched the two-phase flow calculations without including a dynamic term or modifications of the relative permeability for all layers. We used the same mass transfer function as defined for the inflow simulations to model the outflow experiments. The RCM modeling approach produced good agreement with measured outflow data, while being computationally more affordable than traditional models.

5.1 Introduction

Non-uniqueness of fluid retention curves under dynamic and static conditions has been studied extensively in soil physics (e.g., Topp et al. 1967; Stauffer 1977; Schultze et al. 1999). Soil water retention curves have been measured under static conditions as well by means of transient one-step inflow/outflow experiments. Such experiments have shown that capillary pressure-saturation curves depend upon the rate of change of saturation (Hassanizadeh and Gray 1993; Hassanizadeh et al. 2003). These issues, however, have not received much attention in the study of fibrous materials. Previous investigations mostly used measured or calculated hydraulic properties of fibrous materials under static condition as input for modeling transient flow problem (e.g., Landeryou et al. 2005; Jaganathan et al. 2009; Diersch et al. 2011).

One and multi-step inflow/outflow experiments have been used routinely in soil physics for identifying hydraulic parameters by inverse modeling (Durner et al. 1999; Hopmans et al., 2002). In this study we used the one-step outflow method to characterize the hydraulic properties of thin fibrous layers. The approach allowed us to estimate both the relative permeability and dynamic capillarity of a group of six different fibrous layers.

One major difference between soil column experiments and fibrous layer tests is the thickness of the sample as explained below. In our one-step (dynamic) experiments, a thin layer with only a few pores along its thickness is placed on a membrane with a comparable thickness. This creates two issues that are not relevant in the case of soil samples. First, a Representative Elementary Volume (REV) cannot be defined for thin fibrous layer (Qin and Hassanizadeh (2014); Prat and Agaësse 2015). Second, the dynamics of flow in the membrane and in the interface between the membrane and the sample can have a major effect on flow in the thin layer and thus cannot be neglected. This is why we analyzed the inflow/outflow experiments using a recently developed modeling approach by Qin and Hassanizadeh (2014) called the Reduced Continuum Model (RCM). In this approach, a 3D thin fibrous layer is reduced to a 2D continuum, for which the REV extends in the in-plane direction only while having the same thickness as the layer. Thus, all properties of the thin porous material in the RCM are averaged in the through-plane direction. Additionally, mass exchange between two thin layers

is parametrized by considering transfer coefficients that account for the characteristics of the interface region (Qin and Hassanizadeh 2015; Tavangarrad et al. 2018)

Our objective in this study is to perform continuum-scale simulations of transient inflow/outflow experiments using a two-phase flow model, the standard Richards model, and the RCM approach. Results are compared to experimental data and the relative weaknesses and strengths of each modeling approach are discussed.

5.2 Experimental methods and materials

5.2.1 Materials

We selected six hydrophilic thin non-woven fibrous layers for this study. Properties of all layers are listed in Table 5.1. Each layer was assigned a code based on its basis weight. A layer with a specific weight of 25 gsm (gram per square meter), denoted as PP-25, was made of polypropylene fibers, and thermally bonded with bonding points in a lozenge pattern. The non-woven fibrous layer had a thickness of about 200 μm and a porosity of 0.84 when subjected to a 0.3 psi overburden pressure. Another layer made of polypropylene fibers, PP-10, was a 10 gsm spunbonded thin layer with a circular bonding points pattern and had a porosity of 0.88 and a thickness of 130 μm . Surfactant was added to the material of both layers to make them hydrophilic. Two layers were made of polyester fibers and had specific weights of 60 gsm and 86 gsm designated as P-60 and P-86, respectively. The 86 gsm polyester layer was bonded with bonding points in some regions in a circular pattern, while the single 60 gsm layer had no bonding points (fibers of the 60 gsm layer were bonded with chemical resin). We further tested a 120 gsm fibrous layer made of micro glass fibers, denoted by G-120, and a 155

Table 5.1 Properties of hydrophilic fibrous layers used in this study

Material	Porosity [-]	Permeability [m^2]	Thickness [mm] at 0.3 kPa	Basis weight [gsm]	#Code
polypropylene	0.84	8.3 e-11	0.20	25	PP-25
polypropylene	0.88	2.9 e-11	0.13	10	PP-10
Polyester	0.93	1.5 e-9	0.90	60	P-60
Polyester	0.83	1.2 e-10	0.46	86	P-86
cellulose	0.9	9.0 e-11	1.10	155	C-155
Glass fiber	0.95	9.1 e-12	1.00	120	G-120

gsm cellulosic layer, C-155, both of which had bonding point. Other differences in properties of these layers can be found in Table 5.1.

A hydrophilic membrane made of mixed cellulosic esters with a porosity of 0.82, a thickness of 138 μm , and a permeability of $6.1\text{e-}14$ was used in our setup under the samples of fibrous layers. Due to the pore size of 1.2 μm , this strongly fibrous membrane had a very high entry pressure for air, and hence remained saturated at all time in all experiments.

To better visualize the effect of bonding points on pore structure of a fibrous layer, two different polyester samples, P-60 (without bonding points) and P-86 (with bonding points) were imaged under 0.3 psi overburden pressure using μCT scanner (Scanco $\mu\text{CT}50$) with 4-micron isotropic voxel resolution. The μCT images were imported into ImageJ software for thresholding and noise filtration. Figure 5.1 shows the top view of a $4 \times 4 \text{ mm}^2$ section of a P-86 sample after image processing. The dashed red circle shows one of bonding points where fibers were compressed during the production process. Bonding points (Calendar bonding) were distributed all over the layer in regular pattern. A binary image of a cross-

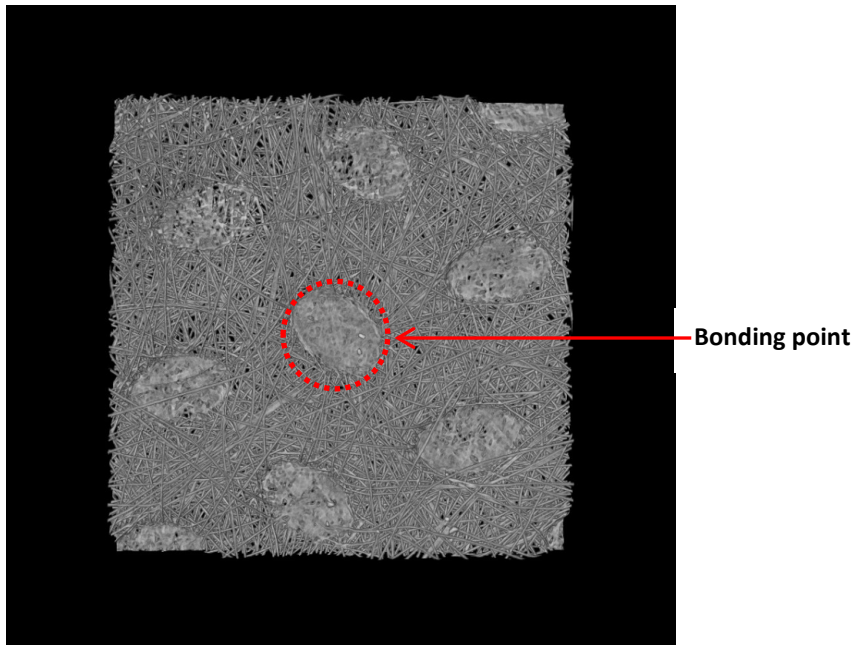


Figure 5.1 Top view image of a $4 \times 4 \text{ mm}^2$ section of the P-86 sample under 0.3 psi overburden pressure. One of bonding points is marked with dashed red circle.

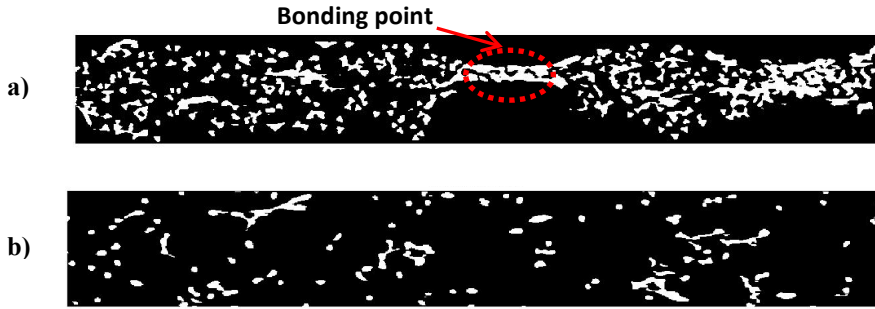


Figure 5.2 A 2D binary image of cross-sectional cut of a fibrous layer: (a) P-86 with bonding points (b) P-60 layer without bonding points.

sectional view of the P-86 sample (Figure 5.2a) displayed a bonding point in the through-plane direction (marked with red circle). However, binary image of a cross sectional view of a P-60 (without bonding points) showed a uniform fiber distribution along the thickness (Figure 5.2b). The variation of fiber content along the sample thickness was determined using a MATLAB code, developed in-house, which used binary images as input. Results are shown in Figures 5.3 and 5.4. The fiber content varied non-uniformly along the thickness of the P-86 layer from less than 5% to 35%. The profile had the bell-shaped form. However, as it can be seen

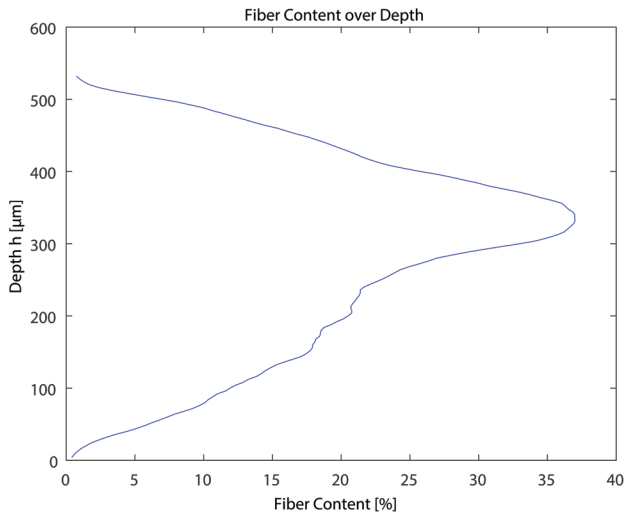


Figure 5.3 Fiber content variation over the thickness of a P-86 sample, which was bonded with bonding points.

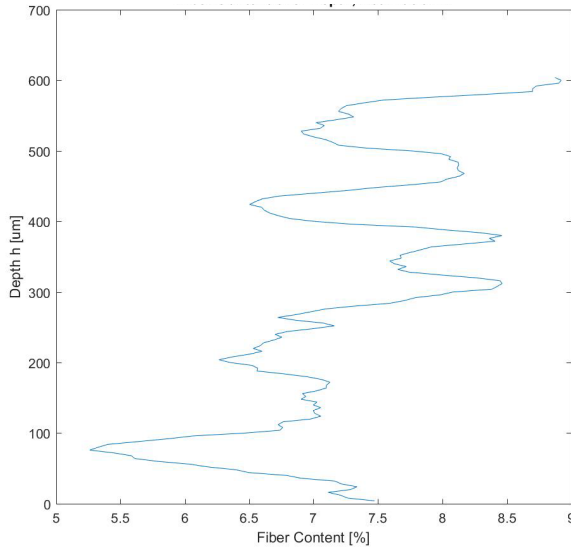


Figure 5.4 Fiber content variation over the thickness of P-60 layer without bonding points.

in Figure 5.4, the fiber content varied from 5% to 9% along the thickness of P-60 sample.

A saline solution, made of 0.9% NaCl (by weight) and distilled water, was chosen as the working liquid. The solution has a surface tension of 72.5 mN/m, a density of 1.005 g/cm³, and a viscosity of 1.019 mPa.s. All synthetic fibrous materials exhibit negligible swelling in such a solution. The 155 gsm cellulosic layer is the only natural material with absorbent fibers.

5.2.2 Autoporosimeter setup

The experimental setup was similar as for our previous study (Chapter 2) as shown in Figure 5.5. A PVD-Autoporosimeter (Pore Volume Distribution) developed by Miller and Tyomkin (1994) was used in this setup. It has a sample chamber and solution reservoir. The sample chamber contained a saline solution and was placed on a high precision balance. The two chambers were connected to each other with a tube, with water movement between them controlled by a valve. The reservoir was covered with a lid to minimize evaporation, while still being connected to atmospheric air. The water level in the reservoir was set equal to the same

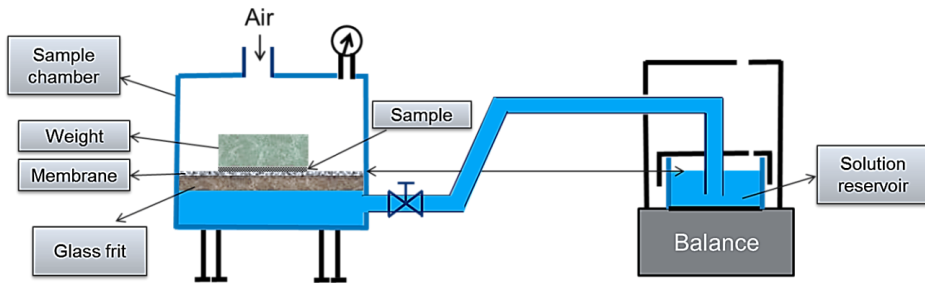


Figure 5.5 Schematic view of experimental setup used in this study.

elevation as the top surface of the membrane. Changes in the water level due to drainage or imbibition of the sample could be considered to be negligible since the reservoir surface area was relatively large.

5.2.3 One-step and multistep inflow/outflow experiment

The autoporosimeter setup shown in Figure 5.5 was designed primarily for multistep experiments in which the imposed air pressure could be varied in several small increments. Saturations of the sample were measured gravimetrically at equilibrium states using a high precision balance. In this way, saturation data points were measured at a given capillary pressure assuming that the water pressure remained equal to atmospheric pressure at equilibrium. Since the sample was placed directly on the membrane, where water pressure was atmospheric, and because gravity is negligible for such thin layers, the water pressure in the sample could be assumed to be atmospheric at equilibrium. At each step, the air pressure was kept constant until equilibrium was reached and capillary flow had ceased. Because of the weight on top of the sample, air could enter or leave the sample only from its edges. It generally took a few minutes for equilibration of the sample. In total, a few hours were needed to perform a full imbibition-drainage experiment. In our previous study (Chapter 2), more details were provided on multistep experiments for thin fibrous layers and possible artefacts.

By imposing one large air pressure step on the sample chamber in the one-step inflow/outflow experiments, one can simulate transient conditions of unsaturated fluid flow in a thin fibrous layer. The autoporosimeter software recorded air pressures in the sample chamber as well as water weight in the reservoir at different times. Saturation in the layer could be computed from changes in the

water weight of the reservoir. Capillary pressures, however, could not be determined, although the air pressure was known, but not the water pressure. Under dynamic conditions, the water pressure did not remain equal to atmospheric pressure and changes during both the inflow and outflow experiments. We investigated whether the hydraulic properties measured in the multistep experiments under static conditions could simulate water saturations also in dynamic one-step inflow/outflow experiments.

5.3 Modeling approaches

5.3.1 Two-phase flow model and the Richards equation

Application of mass conservation to a Darcy-scale representative elementary volume (REV) yields the governing equation for two-phase flow in a porous medium. This mass conservation principle means that changes in the total mass of a fluid phase within this REV must be balanced by its total mass flux over the REV boundary. Mass balance equations for water and air phases, combined with the Darcy equation, was used to model two-phase flow in a thin porous medium. Neglecting gravity due to the small thickness of the very thin layers, and assuming that both phases were incompressible, the governing equations can be written as:

$$\varphi \frac{\partial S^w}{\partial t} - \nabla \cdot \left(\frac{K k_r^w}{\mu^w} \nabla P^w \right) = 0 \quad (5.1)$$

$$\varphi \frac{\partial S^a}{\partial t} - \nabla \cdot \left(\frac{K k_r^a}{\mu^a} \nabla P^a \right) = 0 \quad (5.2)$$

where φ is the porosity, the superscripts w and a denote water and air phases, S is saturation, K is the intrinsic permeability, k_r is the relative permeability coefficient, μ is the viscosity and P is the pressure.

Air and water saturation must sum up to unity:

$$S^w + S^a = 1 \quad (5.3)$$

The macroscopic capillary pressure is commonly used to couple the water and air pressures in the following way:

$$P^a - P^w = P^c(S^w) \quad (5.4)$$

where P^c is the capillary pressure. Commonly air pressure is at atmospheric pressure and can be considered as a passive phase. In such cases, equations (5.1) and (5.4) can be combined to obtain a single equation for water saturation, which is known as the Richards equation.

In this traditional approach, the difference in pressure between the phases is assumed to be equal to the capillary pressure. However, it has been shown that the fluid phases pressure difference also depends on the flow dynamics. Hassanizadeh and Gray (1993) proposed a linear approximation for the difference in fluid pressures under dynamic conditions as a function of the time derivative of the water phase saturation:

$$P^a - P^w = P^c(S^w) - \tau \frac{\partial S^w}{\partial t} \quad (5.5)$$

where τ is a material coefficient that should be determined experimentally.

A well-known nonlinear relation, introduced by van Genuchten (1980), describes the capillary pressure as a function of saturation:

$$P^c(S_e^w) = \frac{1}{\alpha} (S_e^{w-1/m} - 1)^{1/n} \quad (5.6)$$

where the α , m , and n are fitting parameters. The value of $1/\alpha$ approximately corresponds to the inflection point of the P^c - S^w curve. The parameters n and m are fitting parameters that are commonly assumed to be related as $m=1-1/n$. Effective water saturation, S_e^w , is defined as:

$$S_e^w = (S^w - S_r^w) / ((1 - S_r^a) - S_r^w) \quad (5.7)$$

where S_r^w is the residual water saturation and S_r^a is the residual air saturation.

The following Mualem-van Genuchten equations (van Genuchten, 1980; Luckner et al., 1989) were used to describe the water and air relative permeabilities as a function of saturation:

$$k_r^w = S_e^{wl} \left(1 - \left(1 - S_e^{w \frac{1}{m}} \right)^m \right)^2 \quad (5.8)$$

$$k_r^a = (1 - S_e^w)^k \left(1 - S_e^{w \frac{1}{m}} \right)^{2m} \quad (5.9)$$

where $l = 0.5$ and k is equal to $1/3$.

5.3.2 Reduced continua model (RCM)

In the RCM approach, a 3D domain reduces to a 2D domain. The main reason for reducing the dimensionality of the modeling domain is that the Representative Elementary Volume (REV) cannot be defined for a thin porous medium. This is due to the fact that only a few pores exist along the thickness. Qin and Hassanizadeh (2014) formulated the governing equations for the RCM approach based on material properties averaged along the whole thickness (the through-plane direction). Another advantage of RCM over traditional models is that the effect of interlayer space can be taken into account in the form of a mass exchange term. In the RCM approach, the mass conservation equations of water and air in a layer i , combined with Darcy velocity formula, are given by:

$$\left. \frac{\partial(b\rho^w\varphi S^w)}{\partial t} \right|_i - \nabla_h \cdot \left(b\rho^w \frac{k_r^w K}{\mu^w} \nabla_h P^w \right) \Big|_i = Q_T^w|_i + Q_B^w|_i \quad (5.10)$$

$$\left. \frac{\partial(b\rho^a\varphi S^a)}{\partial t} \right|_i - \nabla_h \cdot \left(b\rho^a \frac{k_r^a K}{\mu^a} \nabla_h P^a \right) \Big|_i = Q_T^a|_i + Q_B^a|_i \quad (5.11)$$

in which quantities on the left-hand side are thickness-averaged and those on the right-hand side account for mass transfer between layer i and its neighboring layers. In these equations, b is the layer thickness, ∇_h is the two-dimensional gradient in the in-plane direction; $Q_T^w|_i$ and $Q_B^w|_i$ denote influx and outflux of water from the top and bottom of layer i respectively, and $Q_T^a|_i$ and $Q_B^a|_i$ indicate air fluxes.

For our experiments, in which a layer of fabric with a weight on top is placed on a fully saturated membrane, the governing equations reduce to the following three:

$$\left. \frac{\partial(b\rho^w\varphi S^w)}{\partial t} \right|_f - \nabla_h \cdot \left(b\rho^w \frac{k_r^w K}{\mu^w} \nabla_h P^w \right) \Big|_f = Q_B^w|_f \quad (5.12)$$

$$\left. \frac{\partial(b\rho^a\varphi S^a)}{\partial t} \right|_f - \nabla_h \cdot \left(b\rho^a \frac{k_r^a K}{\mu^a} \nabla_h P^a \right) \Big|_f = Q_E^a|_f \quad (5.13)$$

$$-\nabla_h \cdot \left(b\rho^w \frac{k_r^w K}{\mu^w} \nabla_h P^w \right) \Big|_m = Q_T^w|_m + Q_B^w|_m \quad (5.14)$$

where the subscripts f and m refer to fabric and membrane, respectively. $Q_E^a|_f$ indicates air flux at the edges of a fabric. The air flux boundary, $Q_E^a|_f$, applies on

the nodes at the edge of the fabric only. Water fluxes between the membrane and the fabric are assumed to be related to their pressure difference in the following form:

$$Q_B^w|_f = -Q_T^w|_m = -\Pi_m(P_f^w - P_m^w) \quad (5.15)$$

where Π_m is the coefficient of mass transfer between membrane and fabric. This coefficient depends on the characteristics of the interface region between the two layers. We have to account for two major effects in this coefficient. First, water saturation must build up in one of the layers and the interlayer pore space in order to create a fluid connection between the two layers. Second, the water transfer rate in the connected pores of the interlayer space controls the flux between the layers. As an example, for a system of two layers with a very large gap between them, saturation must build up to approximately unity before any mass transfer is possible and the transfer rate becomes significant. By decreasing the gap and as more and more contact points are created, the saturation threshold reduces and the transfer rate coefficient increases. In our case study, the membrane is fully saturated, while the application of a 0.3 psi overburden pressure created additional contact points between the layers. For this system, we propose the following formula for the exchange coefficient:

$$\Pi_m = \begin{cases} \lambda C & S_f^w < S_{rf}^w \\ \frac{2}{b_m + b_f} \rho^w \frac{\bar{K}_t}{\mu^w} \lambda & S_f^w > S_{rf}^w \end{cases} \quad (5.16)$$

$$\bar{K}_t = \left(\frac{b_m + b_f}{b_f K_m + b_m K_f k_{rf}^w} K_m K_f k_{rf}^w \right) \quad (5.17)$$

where S_{rf}^w is the residual saturation of the fibrous layer, C is a constant equal to 3.35e-5 and assumed to be the same for all layers, and λ is the transfer rate coefficient. For the case of perfect contact between the membrane and the sample, λ takes value of 1. For saturations less than the residual saturation of the sample, connected pathways are not created and the flux only depends on the interface properties. Once residual saturation is reached, the harmonic mean of the relative permeabilities determines the exchange between the two layers. Equations (5.6) to (5.9) are then used for the hydraulic properties in the RCM model.

5.4 Numerical simulations

5.4.1 Values of input parameters

Values of the porosity and intrinsic permeability of various fibrous layers used in this study are reported in Table 5.1. Porosities were calculated based on maximum water uptake of each layer. Permeabilities were measured using the falling head method. We note that the permeability of a single thin fibrous layer depends not only on the porosity but also the fiber radii of that layer, among other characteristics. As mentioned earlier, the retention curves of fibrous layers were measured by performing multistep inflow/outflow experiments using the PVD-Autoporosimeter. The fitted VG parameters of all layers are tabulated in Table 5.2.

Figure 5.6 compares measured imbibition capillary pressure-saturation curves for all material layers used this study. The P-60 layer had the lowest capillarity, while C-155 layer showed highest capillarity among all sample layers. The relative permeability function of each layer was calculated based on the fitting parameters obtained from retention curves reported in Table 5.2. For the dynamic inflow simulations, we investigated the role of relative permeability at low saturation levels of each phase by performing a sensitivity analysis. Moreover, the effect of dynamic capillarity (τ) was taken into account by considering either $\tau=1000$ Pa.s or a value estimated using Stauffer formula (1977). Figure 5.7 shows different combinations of relative permeability and the dynamic capillarity values that were used in the one-step inflow analyses. For water saturations higher than 0.2 and air saturations higher than 0.5, relative permeability functions given in equations (1.8) and (1.9) were employed in all modeling approaches.

Table 5.2 VG fitted parameters of the fibrous layers for both imbibition and drainage

#Code	α	n	α	n	S_r^w
	imbibition [1/Pa]	imbibition [-]	drainage [1/Pa]	drainage [-]	
PP-25	0.0014	5.15	0.0005	7.16	0.06
PP-10	0.00096	2.68	0.00024	3.76	0.1
P-60	0.073	4.32	0.0017	7.71	0.01
P-86	0.0012	5.06	0.00046	4.52	0.09
C-155	0.00058	3.62	0.00019	3.68	0.08
G-120	0.00022	4.98	0.00009	2.04	0.2

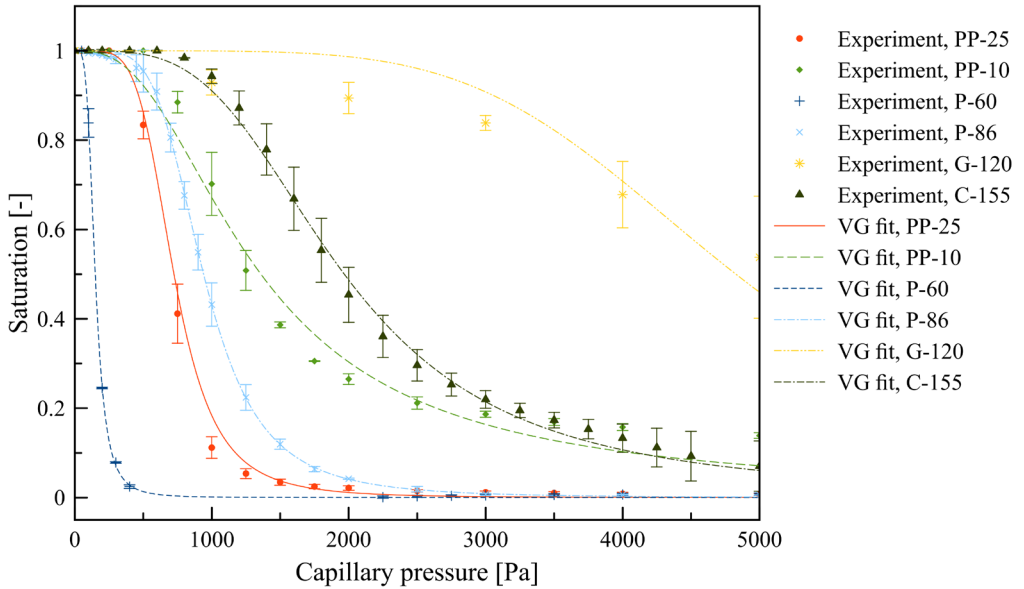


Figure 5.6 measured data points and VG fitted curves of capillary pressure-saturation relationship for non-woven fibrous layers used in this study.

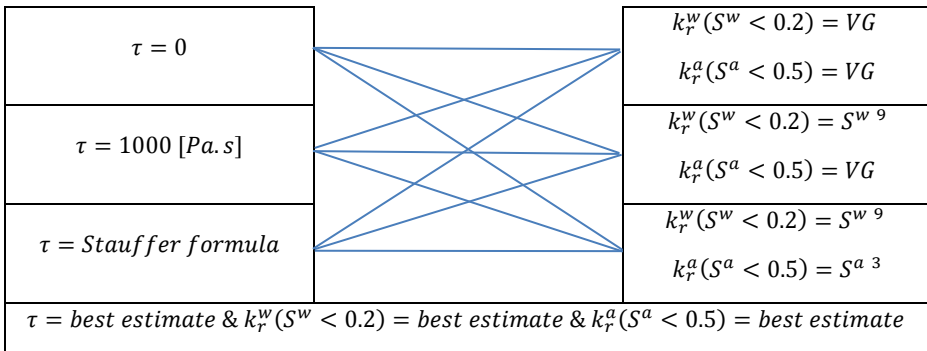


Figure 5.7 Scheme of combination of dynamic capillarity and relative permeability functions used in our sensitivity analysis.

5.4.2 Two-phase flow solutions

In the two-phase fluid flow simulations, the top fibrous layer and the bottom membrane were modeled as a 2-D axisymmetric domain. A schematic view of the

modeling domain can be seen in Figure 5.8. The domain was discretized with rectangular elements. A preliminary study showed that 44,522 elements were sufficient to obtain mesh independent results. Equations (5.1) and (5.10) were solved for the top domain. Since the membrane was fully saturated with water, the water pressure was the only variable of the bottom domain and hence only equation (5.1) without the saturation derivative term needed to be solved. Since a metal weight was placed on the sample layer, a no flux boundary condition was specified for the top surface of the modeling domain (Boundary 1). Air could enter and leave the fibrous layer through the lateral edges of the top domain only (Boundary 2). Continuity of the water flux and pressure as well as a zero air flux were considered for the contact surface of the membrane and the sample (Boundary 3). No-flux boundary conditions for both phases were assumed on the edge of the membrane (Boundary 4). A Dirichlet boundary condition with a zero water pressure was specified along the bottom surface of the membrane (Boundary 5).

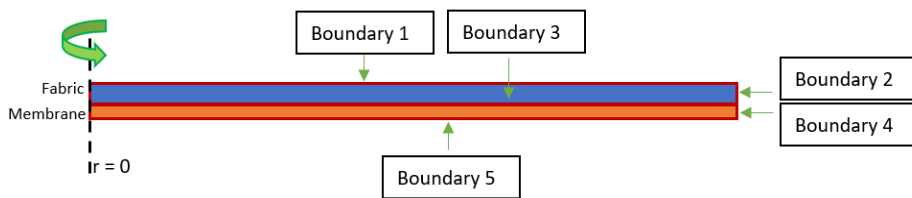


Figure 5.8 Schematic view of the 2-D axisymmetric domain used in this study.

5.4.3 Solution of the Richards model

For the Richards model, equation (5-1) was solved for a fibrous layer and a membrane. Since water was the only fluid phase in this equation, the geometry of modeling domain can be reduced to a 1D domain with vertical flow of water. Our preliminary Richards simulation results showed no differences for the inflow and outflow tests assuming 1D or 2D domains. Additionally, the air pressure boundary applied to the edge of sample for two-phase flow model should be transformed to a water pressure and applied to the boundary underneath the membrane. The water pressure specified along the lower surface of membrane is then positive for imbibition and negative for drainage.

5.4.4 Solution of the Reduced Continua Model (RCM)

The RCM computational domain was consisted of two circular 2D domains positioned on top of each other. Each domain was discretized using a total of 2170 triangular mesh elements. Equations (5-12) and (5-13) correspond to the top fibrous layer and 5-14 to the bottom membrane. The sink/source terms of the wetting phase in the constitutive equations were calculated based on equations (5-15) to (5-17). An air pressure boundary, which is a function of time, was applied to the edge boundaries of the sample. All equations were solved using the COMSOL software.

5.5 Results and discussion

5.5.1 Dynamic inflow experiments

Variations in the air pressure inside the chamber and the wetting saturation over time for PP-10 layer are plotted in Figure 5.9. Differences in the evolutions of the water saturation of the two different replicates are attributed to differences in the

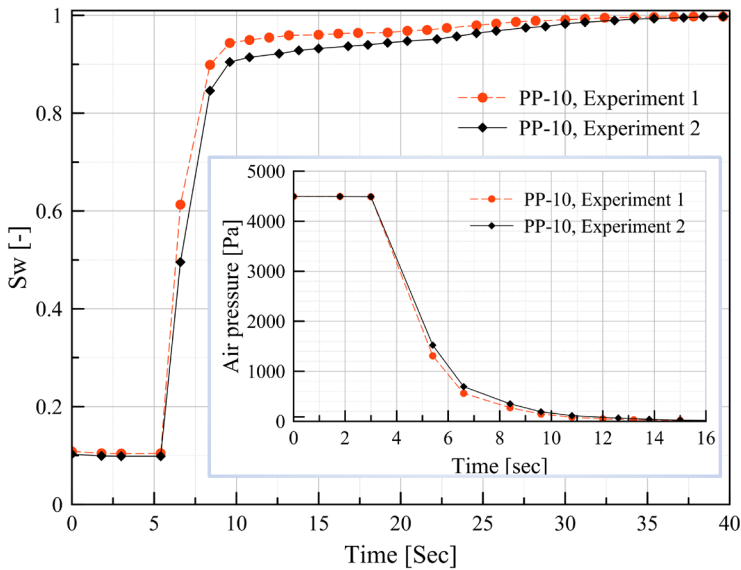


Figure 5.9 Water saturation evolution of PP-10 material when air pressure dropped from 4500 Pa to zero within 10 seconds. Experimental results of second repetition shows higher air pressure at the boundary result in slower change of saturation over time.

air pressure boundary condition applied to the edges of the PP-10 samples. The air pressure was reduced from 4500 Pa to zero at $t=3$ seconds. The air pressure inside the sample chamber reached zero in less than 15 seconds. Water started wetting the fibrous substrate after 5 seconds. It took more than 30 seconds for the sample to become fully saturated with water. The initial water saturation of 0.1 corresponded to the initialization stage when an air pressure of 4500 Pa was imposed along the boundary for enough time to reach equilibration. The last 3 seconds of this initialization stage is shown in Figure 5.9.

For other materials, except G-120, the same air pressure drop (4500 Pascal) was imposed at the boundary of the fibrous layer inside the sample chamber (Figure 5.10). Since the capillarity of G-120 was much higher than the other materials, and in order to start the inflow experiments with an initially low water saturation and cover a wider range of saturations, we started with an air pressure of 20,000 Pa,

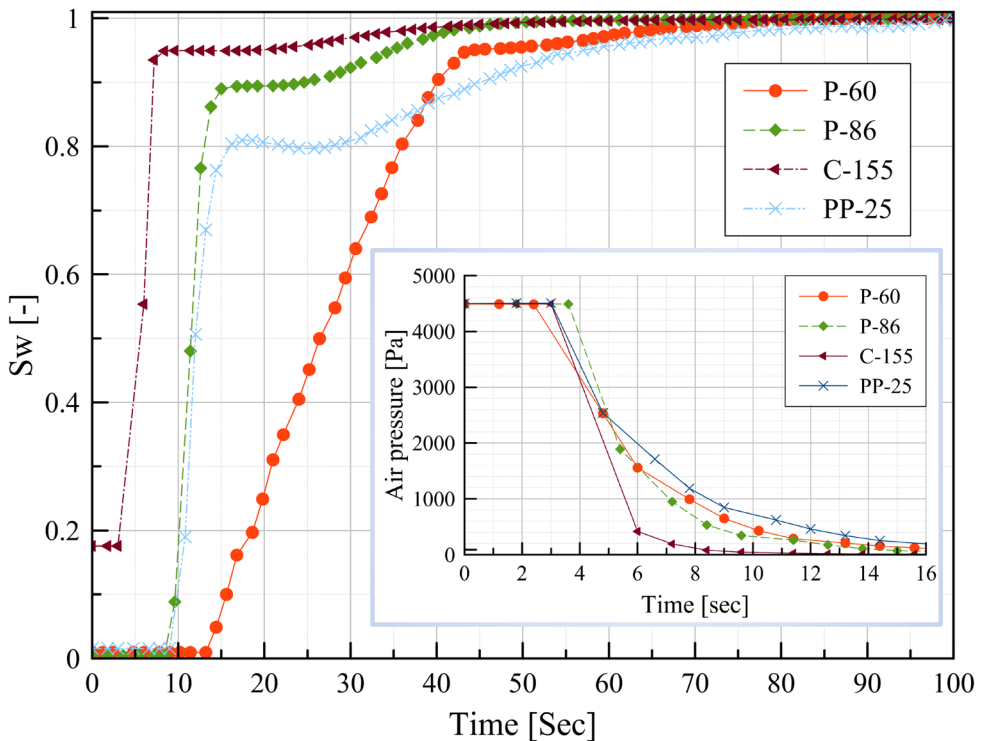


Figure 5.10 Evolution of water saturation of four different materials when the air pressure was decreased from 4500 Pa to zero within 10 seconds.

which was reduced to zero in less than 10 seconds. The outcome of gravimetric water saturation measurements for the G-120 layer is depicted in Figure 5.11. For this material, water moved rapidly to the fibrous layer and reached equilibrium in about 60 seconds. Applied boundary air pressures and measured water saturations over time are plotted in Figure 5.10 for PP-25, P-86, P-60, and C-155. Water saturation started to increase at different times depending upon initial water saturation values and air entry pressures. For example, the low air entry pressure of P-60 caused water to infiltrate later into this sample comparing to the other materials.

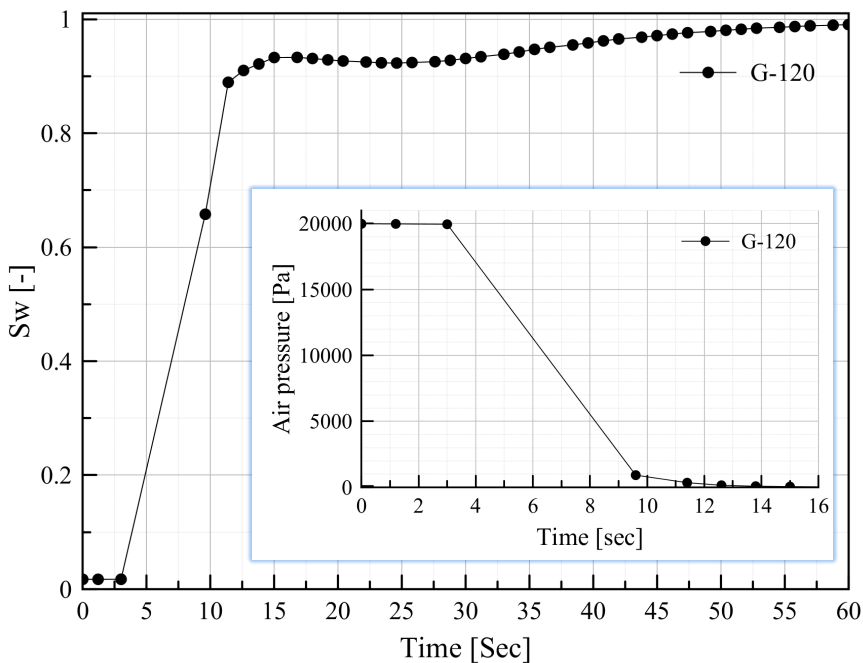


Figure 5.11 Evolution of water saturation of G-120 layer when the air pressure was decreased from 20000 Pa to zero within 10 seconds.

5.5.2 Dynamic inflow simulation results using the two-phase flow and Richards models

The applicability of the standard Richards equation for modeling dynamic inflow experiments was investigated by comparing its results with a two-phase flow model and laboratory data for the P-86 fibrous sample layer (Figure 5.12). Both

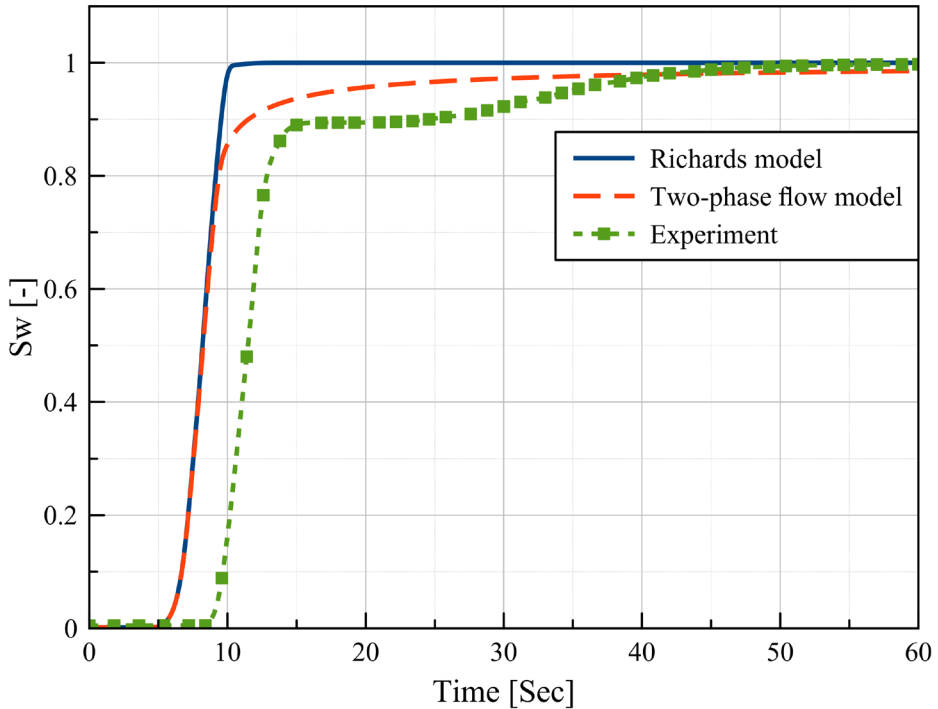


Figure 5.12 Comparison of the Richards and two-phase fluid modeling results with dynamic inflow experimental data for the P-86 layer.

modeling approaches employed VG functions for relative permeability without further modifications. Moreover, the effect of dynamic capillarity was neglected in these simulations. Although both models predicted more rapid water infiltration into the sample as compared to the experimental results, the effect of including air dynamics at low air saturations could be achieved only with the two-phase flow modeling approach. Therefore, the two-phase flow approach was selected for the inflow simulations.

Two-phase flow modeling results for the two other materials with bonding points (i.e., PP-25 and PP-10) are shown in Figure 5.13. A common feature of the results for these two materials is that the average saturation in the layer started to increase earlier than the experimental data. The measured starting time of the saturation increase lagged behind the modeling results for PP-10, PP-25, and P-86.

Two-phase flow modeling results for materials without bonding points (P-60, C-155, G-120) showed good agreement with the laboratory data for the simulated starting time of water infiltration (Figure 5.14). However, discrepancies can be seen between the simulated and experimental data at relatively high saturations for P-60.

Note that C-155 and PP-10 are the only materials which were not initially dry. For one of them, PP-10, a delay was observed while the simulated starting time of saturation build-up for C-155 very closely matched the measurement data. However, the initial saturation value estimated from the Pc-S curve was different from its measured value using the dynamic test for C-155. This can be explained based on sample variation and, accordingly, the large standard deviation in water saturations obtained for a capillary pressure of 4500 Pa of this layer (see Figure 5.6).

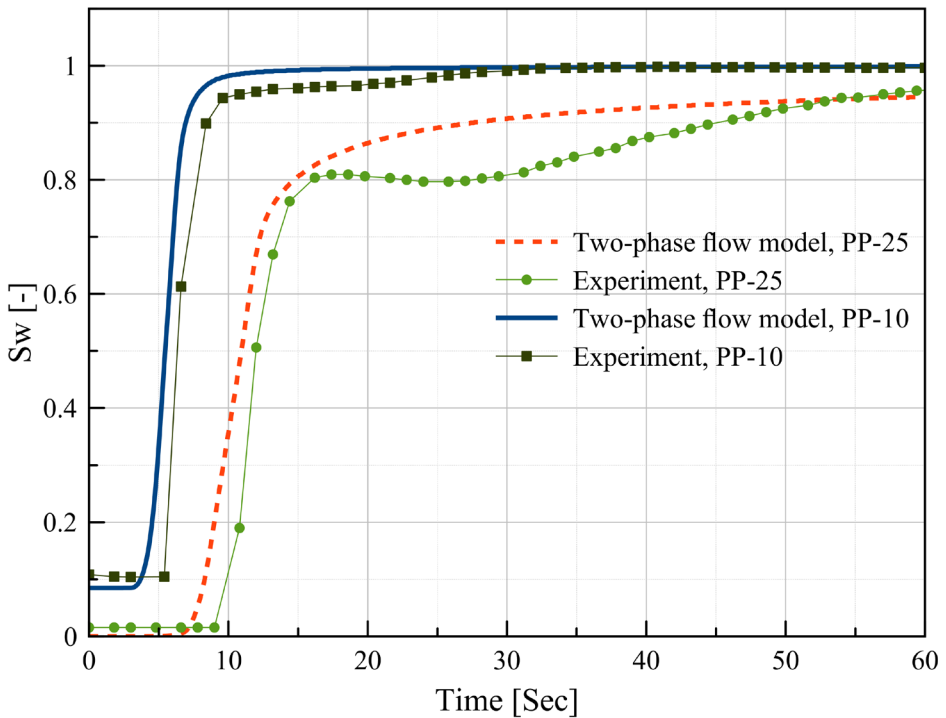


Figure 5.13 Two-phase flow modeling results of the dynamic inflow experiments for PP-25 and PP-10.

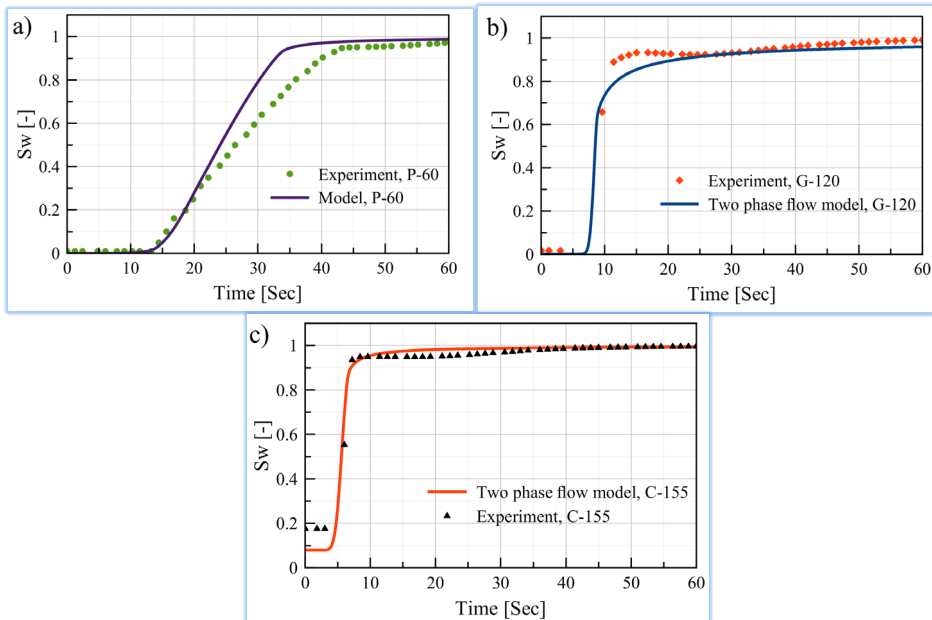


Figure 5.14 Temporal evolution of water saturation obtained with the two phase flow model compared to measured data.

The effect of the dynamic capillarity term for different materials is shown in Figures 5.15 and 5.16. For all materials, the value of the coefficient τ changed the slope of the water saturation curve, but had no significant effect on the starting point of water infiltration.

A sensitivity study of the effects of the relative permeability function for materials with bonding points confirmed the importance of the wetting phase relative permeability at low water and air saturations (Figure 5.17). The relative permeability function needed to be modified at low water and air saturations. Basically, the permeability function at low water saturations was modified such that the time delay could be reproduced correctly for nonwovens with bonding points. We note that although the water saturation of PP-10 was initially 0.1, its permeability values for water saturations lower than 0.2 still needed to be reduced significantly. As opposed to these materials, the VG function did not need to be modified for materials without bonding points. This suggests another possible explanation for the time shift between simulated and experimental results for materials with bonding points. The delay time could be attributed to the interlayer-

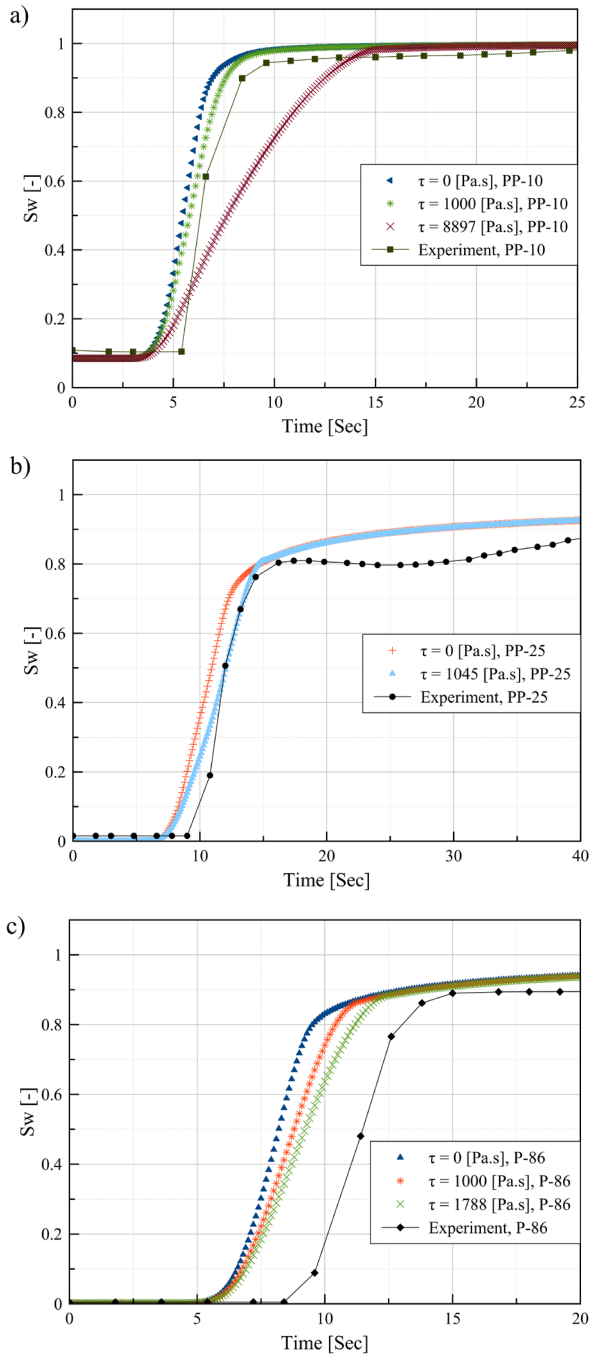


Figure 5.15 Effect of the dynamic capillarity on simulated water saturations of three samples with bonding points: PP-10 (top), PP-25 (middle), and P-86 (bottom).

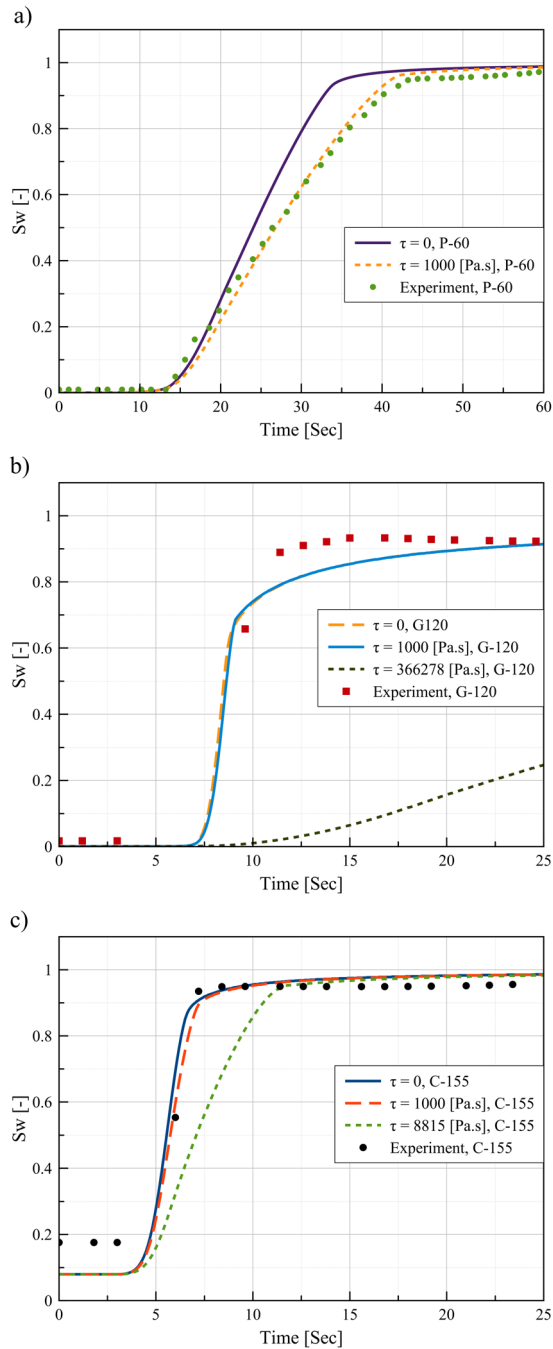


Figure 5.16 Effect of the dynamic capillarity on simulated water saturations of three samples without bonding points: P-60 (top), G-120 (middle), and C-155 (bottom).

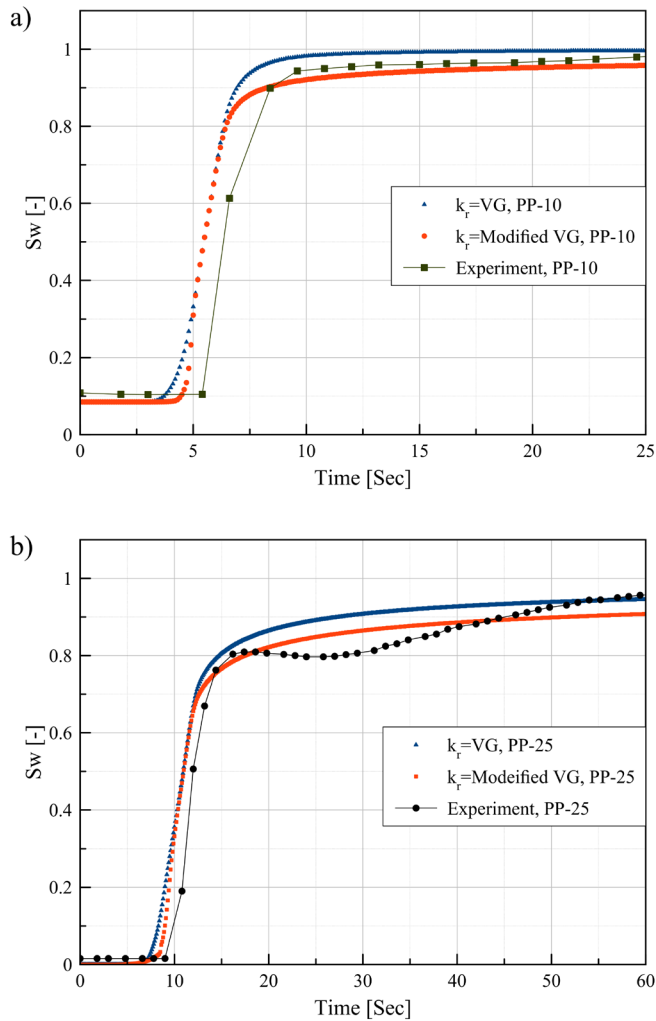


Figure 5.17 Effect of varying relative permeability functions at low air and water saturations on simulated water saturations of samples with bonding points: PP-10 (top), and P-25 (bottom).

space between the membrane and the samples with bonding points (calendar bonding). We accounted for this effect in the RCM approach, and compared results with the experimental data (next section). Finally, based on results of our simulations, we did select parameters for the dynamic capillarity and relative permeability in order to obtain the best fit to the observed data for six non-woven samples. Optimal fits for C-155 and G-120 were obtained with the two-phase flow

model without any further modifications of the VG relative permeability and without including the dynamic term. For P-60, the starting time of water infiltration was predicted very well, and also the slope of the water saturation curve, by setting $\tau=1000$ Pa.s. Best-fit simulation results for three nonwoven materials with bonding points are compared with experimental results in Figure 5.18. For all of these materials, modification of both the relative permeability function and the dynamic capillarity produced satisfactory matches with the experimental data.

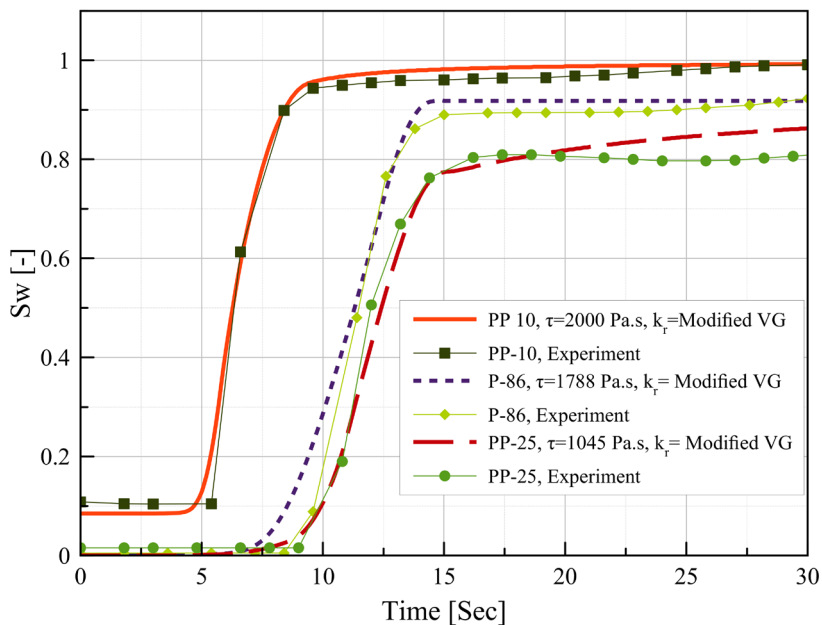


Figure 5.18 Best-fit simulation curves for the evolution of water saturation with time for materials with- bonding points following adjustments in the coefficient τ and the relative permeability function at low saturations.

5.5.3 Results of one-step inflow simulations using the Reduced Continua Model (RCM)

Figure 5.19 shows RCM dynamic inflow simulation results for layers without bonding points (P-60, C-155 and G-120). The value of the mass transfer coefficient λ (Equation 5.16) was assumed to be unity for these layers since the

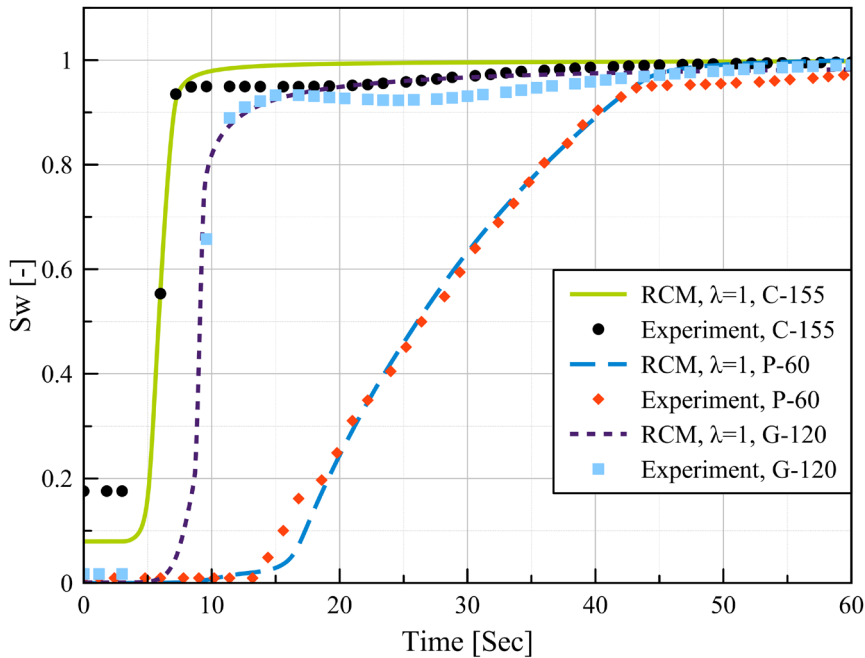


Figure 5.19 RCM results for dynamic inflow for a group of materials without bonding points (without calendar bonding).

membrane and the layers were perfectly connected. Very good agreements with the measured saturation data points are achieved.

For materials with bonding points, however, the value of λ had to be much smaller in order to account for the imperfect contact between the sample and the membrane. Results for PP-10 suggested a value of 0.08 for λ , while much higher values of 0.23 and 0.18 were needed for P-86 and PP-25, respectively (Figure 5.20). The effect of the interface was very significant for the layers with bonding points due to the fact that relatively large space was present between the sample and the membrane.

RCM results for PP-10 shown in Figure 5.20 perfectly matched the measured data for the entire saturation range when λ was fixed at 0.08. For the PP-25 and P-86 materials, very good agreement was obtained for saturations up to 0.8 by reducing the value of λ . But some disagreement is apparent between the RCM results for PP-25 and P-86 and the laboratory data at water saturations above 0.8.

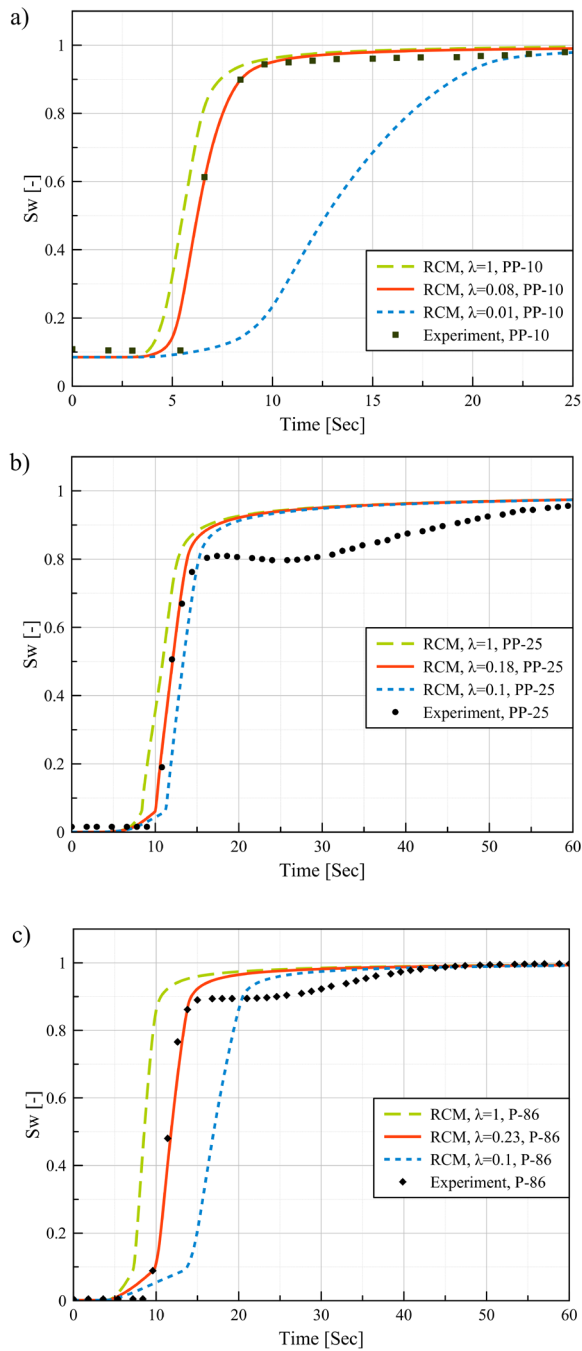


Figure 5.20 RCM simulation results for the dynamic inflow experiments for the group of materials with bonding points.

5.5.4 Dynamic outflow experiments

Results for the outflow experiments are plotted in Figures 5.21 and 5.22. The transient air pressure data is shown also for each material. Since the capillarity range differed between materials, different air pressure increases were applied in each experiment. We performed multiple experiments with different air pressures for each sample. Results of the experiments at a pressure of 4500 Pa are plotted in Figure 5.21 for PP-10, PP-25, P-86, P-60, and C-155.

The experimental outflow results of G-120 when exposed to pressures of 10000 and 20000 Pa are shown in Figure 5.22. Water saturations at equilibrium decreased to 0.67 and 0.31 when the pressures were 10000 and 20000 Pa, respectively.

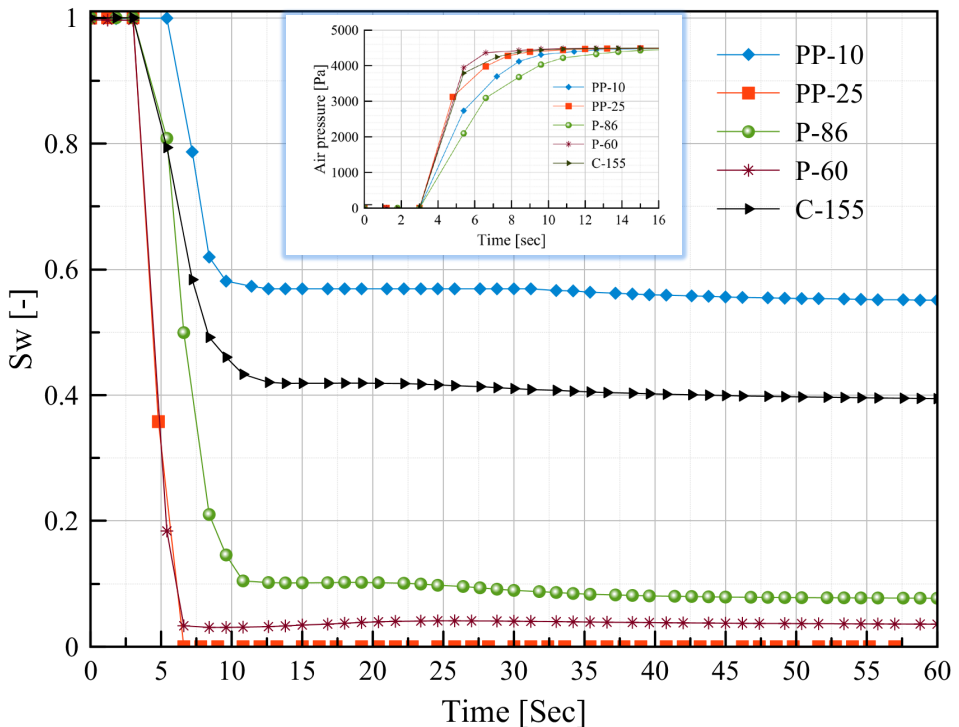


Figure 5.21 Results of the outflow experiments for PP-10, PP-25, P-86, P-60, C-155.

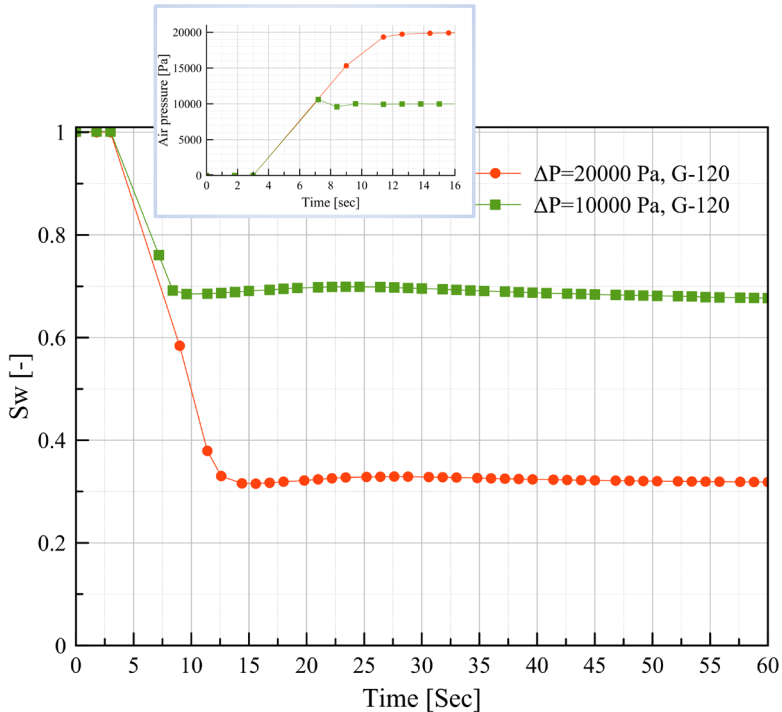


Figure 5.22 Results of outflow experiments for G-120 when exposed to pressures of 20000 and 10000 Pa.

5.5.5 Dynamic outflow simulations using the two-phase flow model and Reduced Continua Model (RCM)

The outcome of the dynamic outflow simulation results is shown in Figures 5.23, 5.24, and 5.25. The two-phase flow and RCM approaches both could predict the measurement data satisfactorily for all samples. Note that we used the same exchange coefficient as for the inflow simulations for all samples. A good match could be obtained with the same values for λ that were chosen for the inflow simulations, i.e., a λ value of 1.0 for G-120, P-60, and C-155, while the λ values were 0.08 for PP-10, 0.18 for PP-25, and 0.23 for P-86 (see Figures 5.23 to 5.25). The effect of variations in λ is also included in these figures. When a value of 1.0 was used for λ , the saturation curves of RCM and the two-phase model matched very well, as expected. Since the saturation simulation results for two-phase flow

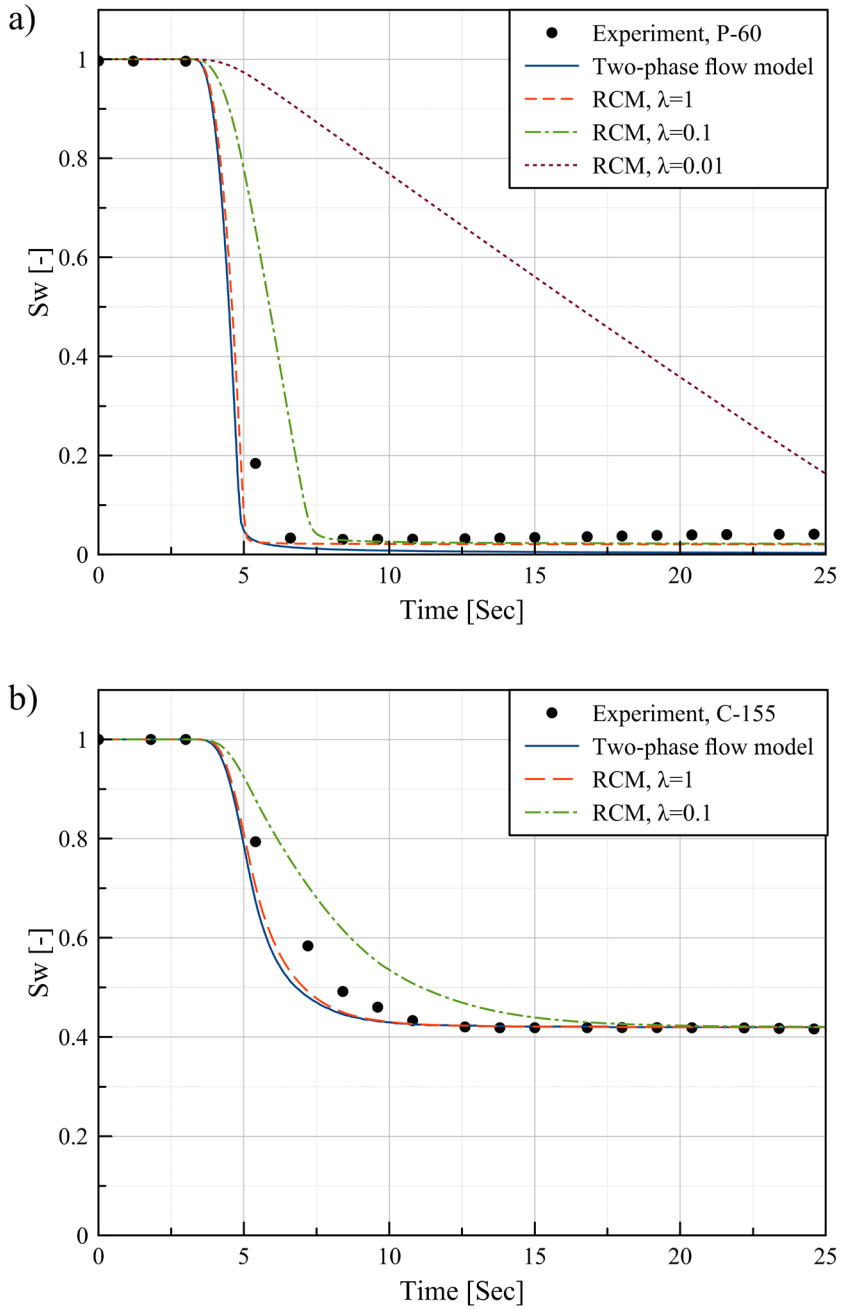


Figure 5.23 Comparison of the two-phase Darcy flow and RCM outflow simulations with the experimental data for P-60 (top) and C-155 (bottom).

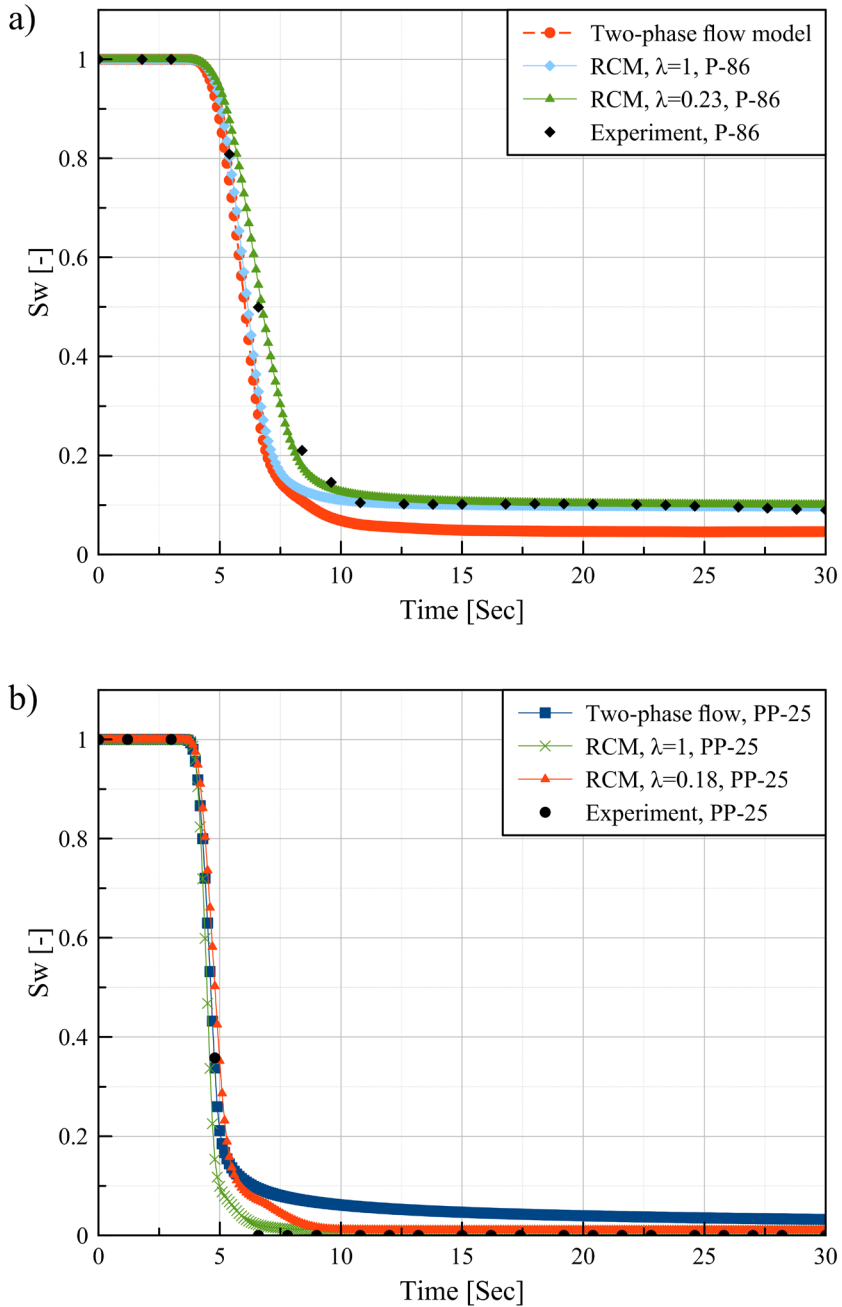


Figure 5.24 Comparison of the two-phase Darcy flow and RCM outflow simulations with the experimental data for PP-86 (top) and P-25 (bottom).

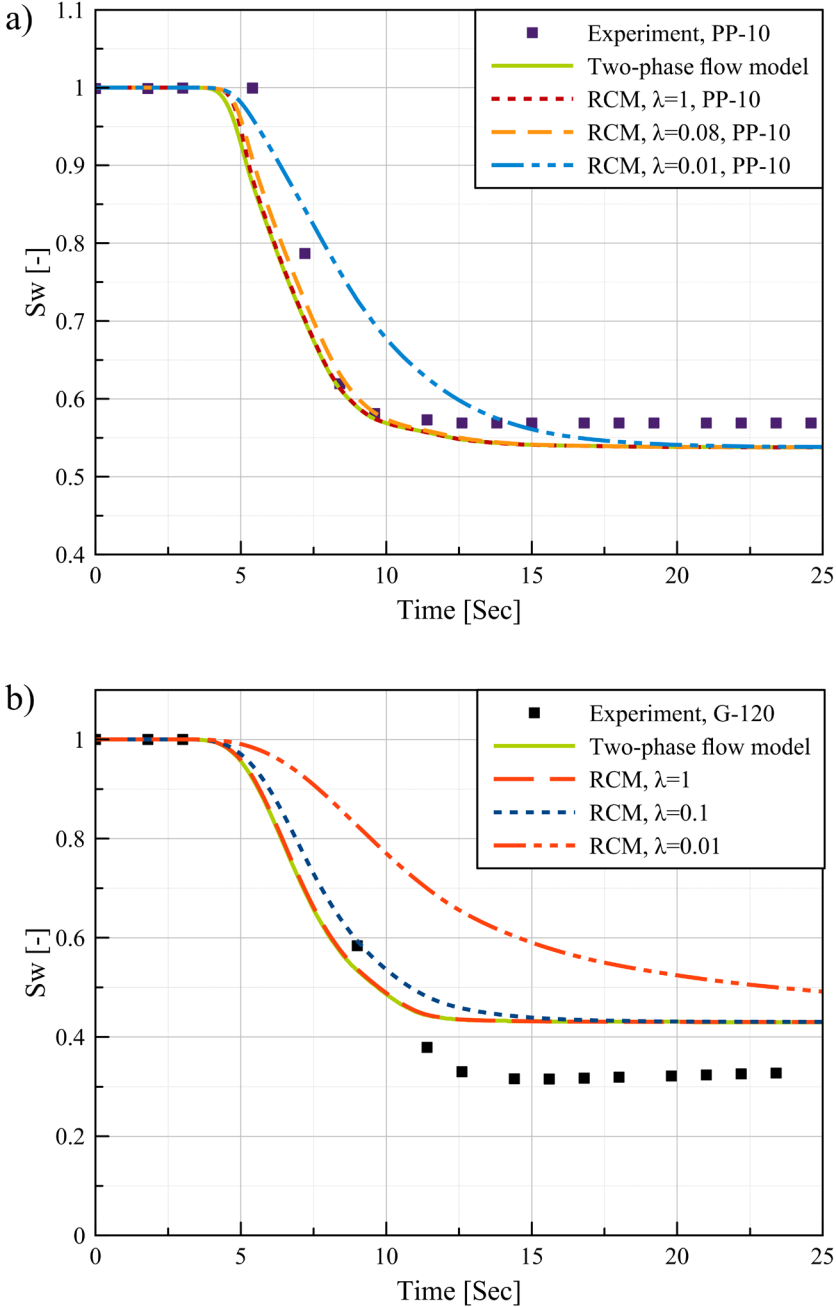


Figure 5.25 Comparison of the two-phase Darcy flow and RCM outflow simulations with the experimental data for PP-10 (top) and G-120 (bottom).

were close to the experimental data, the λ value of 1 could reproduce similarly good results. However, as can be seen in Figure 5.24, slightly better results were obtained when λ was set equal to 0.23 for P-86, which is the same value as used for the inflow simulations. In summary, the RCM approach could simulate both inflow and outflow experiments with the same set of equations and parameter values.

5.6 Conclusions

We performed quasi-static and dynamic inflow and outflow experiments for thin samples of a group of six different non-woven materials using autoprosmetry technique. Measured quasi-static data points were employed to find the capillary pressure saturation curves that were fitted using the VG equations. Fitting parameters were used as an input for modeling the dynamic experiments. For the inflow tests, the air pressure at the edges of the sample was suddenly decreased from a large value to zero in about 10 seconds, whereas for the outflow tests, the air pressure was increased rapidly in approximately same time. This resulted in very fast wetting or drainage processes of the sample in less than one minute.

Two-phase Darcy flow modeling and a new approach using a Reduced Continua Model were employed to simulate the dynamic experiments. The two-phase Darcy flow approach approximated the measured saturation inflow data satisfactorily for non-woven samples without bonding point. However, for three non-woven samples with bonding points (calendar bonding) showed a time shift between numerical results of the two-phase Darcy model and laboratory data. Results of simulations with the RCM approach, on the other hand, agreed very well with the experimental results. This is mainly because the RCM approach could account for imperfect contact between the sample and the membrane through a mass exchange term. Moreover, the computational effort of the RCM approach was one order of magnitude less than that of the Darcy approach.

The outflow simulation results were very close to the experimental data for both modeling approaches. Slightly better agreement was reached with RCM employing the same parameter values for the outflow and inflow experiments. The RCM is a robust and powerful thermodynamic-based technique for prediction of unsaturated fluid flow in thin porous media. Not only is this new technique computationally efficient and preserves the REV concept for thin porous layers,

but also accounts for the effects of interlayer space between two neighboring layers in a stack of multiple thin layers (Mohebbi et al. 2018) through a mass exchange coefficient.

References

- Diersch, H. J. G., Clausnitzer, V., Myrnyy, V., Rosati, R., Schmidt, M., Beruda, H., Ehrnsperger, B. J., Virgilio, R.: Modeling Unsaturated Flow in Absorbent Swelling Porous Media: Part 2. Numerical Simulation, *Transport in Porous Media*, 86(3) (2011)
- Durner, W., Schultze, B., Zurmühl, T.: State-of-the-art in inverse modeling of inflow/outflow experiments. In: van Genuchten, M.T., Leij, F.J., Wu, L. (Eds.), *Proceedings of the International Workshop on Characterization and Measurement of the Hydraulic Properties of Unsaturated Porous Media*, University of California, Riverside, CA, pp. 661–681(1999)
- Hassanizadeh, S.M., Gray, W.G.: Thermodynamic basis of capillary pressure in porous media. *Water Resources Journal. Res.* 29, 3389–3405 (1993)
- Hassanizadeh, S.M., Celia, M.A., Dahle, H.K.: Dynamic effects in the capillary pressure-saturation relationship and their impacts on unsaturated flow. *Vadose Zone Journal*, 1. 38-57 (2002)
- Head, K.H.: *Manual of Soil Laboratory Testing*, Vols 1–3. Pentech Press, London (1992)
- Jaganathan, S., Vahedi Tafreshi, H., Pourdeyhimi, B.: A realistic modeling of fluid infiltration in thin fibrous sheets. *J. Appl. Phys.* 105, 113522 (2009)
- Landeryou, M., Eames, I., Cottenden, A.: Infiltration into inclined fibrous sheets. *Journal of Fluid Mechanics.* 529, 173–193 (2005)
- Luckner, L., van Genuchten, M. Th., Nielsen, D. R.: A consistent set of parametric models for the two-phase flow of immiscible fluids in the subsurface. *Water Resour. Res.*, 25(10): 2187-2193 (1989)
- Miller, B., Tyomkin, I.: Liquid porosimetry: new methodology and applications. *J Col Int Sci.* 62,163-170 (1994)
- Mohebbi, B., Tavangarrad, A.H., Clausen, J., Blümich, B., Hassanizadeh, S. M., Rosati, R.: Revealing how interfaces in stacked thin fibrous layers affect liquid ingress and transport properties by single-sided NMR. *Journal of Magnetic Resonance* (2018)
- Prat, M., Agaësse, T.: Thin porous media. In: Vafai, K. (ed.) *Handbook of Porous Media* (Chapter 4), 3rd edn. Taylor & Francis, London (2015)
- Qin, C. Z. and Hassanizadeh, S. M.: Multiphase flow through multilayers of thin porous media: General balance equations and constitutive relationships for a solid-gas-liquid three-phase system. *International Journal of Heat and Mass*

- Transfer.70, 693–708 (2014)
- Qin, C. Z., Hassanizadeh, S.M.: A new approach to modelling water flooding in a polymer electrolyte fuel cell. *International journal of hydrogen energy*. 40, 3348-3358 (2015)
- Richards, L.A.: Capillary conduction of liquids through porous mediums. *Physics*. Vol. 1, 318-333 (1931)
- Schultze, B., O. Ippisch, B. Huwe, and W. Durner: Dynamic nonequilibrium during unsaturated water flow. In: M. Th. van Genuchten, F. J. Leij and L. Wu (eds.) *Proc. Int. Workshop, Characterization and Measurement of the Hydraulic Properties of Unsaturated Porous Media*. p. 877-892 (1999)
- Stauffer, F: Einfluß der kapillaren Zone auf instationäre Drainagevorgänge. Ph. D. Thesis, ETH Zürich, Switzerland (1977)
- Tavangarrad, A.H., Mohebbi, B., Hassanizadeh, S. M., Rosati, R., Clausen, J., Blümich, B.: Continuum-scale modeling of liquid redistribution in a stack of thin hydrophilic fibrous layers. *Transport in Porous Media*. 122, 203-219 (2018)
- Topp, G. C., A. Klute, and D. B. Peters: Comparison of water content–pressure head data obtained by equilibrium, steady state, and unsteady–state methods. *Soil Sci. Soc. Am. Proc.* 31, 312–314 (1967)
- van Genuchten, M. Th.: A closed-form equation for predicting the hydraulic conductivity of unsaturated soils. *Soil Sci Soc. Am J.* 44, 892-898 (1980)

Chapter 6

Summary and conclusions

6.1 Conclusions

We have performed experimental and numerical studies of unsaturated fluid flow in a stack of thin non-woven fibrous layers. The main objective was to investigate the validity of a traditional Darcy scale model and a Reduced Continua Model (RCM), which is a new macroscopic approach, by comparison with observed data. To do so, we first characterized the physical and hydraulic properties of the non-woven layers. Next, a number of infiltration and drainage experiments were performed and compared to the modeling results.

In Chapter 2, we presented our results of a series of experiments for obtaining the capillary pressure-saturation relationship of a thin hydrophilic non-woven fibrous layer. The effects of overburden pressure imposed on a layer, the use of consecutive imbibition-drainage cycles, and increasing the number of layers were investigated for two different materials: a thermally bonded non-woven polyolefin layer with bonding points and a chemically bonded polyester layer without bonding points. The polyolefin layer was used later for liquid redistribution tests and dynamic inflow/outflow experiments.

The overburden pressure imposed on a single thin layer had a significant effect on the measured capillary pressure-saturation curves. This is because of deformability of the non-woven fibrous layers. As a result of applying overburden pressure, the porosity and permeability also changed notably. These two parameters were employed for scaling the capillary pressure-saturation curves based on Leveret's J function. Experimental results could be matched satisfactorily with this scaling approach.

Increasing the number of layers had only minor effects on the measured capillary pressure-saturation curves. However, the dynamic process was totally different for a single layer compared to two layers. The effect of consecutive imbibition-drainage cycles was also reported in the second chapter. The main imbibition curves moved toward higher saturations and higher capillarities compared to primary imbibition because the polyolefin layer contained some fluid at the beginning of main imbibition and had higher surface energy.

We also improved the experimental setup to reduce the artefacts in the measurement of a single thin fibrous layer due to the small volumes involved in

such experiments. The modified setup was used later in measurements of dynamic inflow/outflow experiments. Additionally, we characterized other non-woven fibrous layers used in different research studies of this project with the above-mentioned approach. This characterization method provided suitable input for the unsaturated fluid flow simulations.

Next, in Chapter 3, a study on liquid redistribution of a stack of two thin non-woven fibrous layers was performed, both experimentally and numerically. A single sided NMR-MOUSE was used to monitor the change in water saturation of a wet fibrous layer due to water transfer to an underlying identical dry layer. Very little water redistribution occurred in about three minutes. The small change in water saturation was attributed to hysteresis in the capillary pressure-saturation curves. Indeed, the final equilibrium saturations in the layers corresponded with the hysteretic capillary pressure-saturation curves that were measured for that fibrous layer. However, transient changes in saturations that were calculated using the Richards model were found to be much faster than the observations. Differences could be minimized by either changing the relative permeability function to very small values or including a dynamic capillarity term, which led to better results.

A major problem with employing traditional Darcy-based models for a thin porous layer is that representative elementary volume requirements are not satisfied for such a layer due to the fact that only few pores exist along its thickness. Furthermore, since perfect contact is assumed between two thin layers in traditional models, the interface effect was neglected. To resolve the above-mentioned issues, RCM was employed to simulate the liquid redistribution experiment. This model allowed us to include the interlayer space effect through a mass transfer term. Temporal evolution of the average water saturation was predicted satisfactorily when the mass transfer coefficient was made proportional to the harmonic mean of the relative permeabilities of the two layers. There was no need to include a dynamic capillarity term. Further investigations showed that the upper part of the lower dry layer exhibited a lower fiber content and higher porosity compared to its middle part. Accordingly, the delaying effect corresponded to interlayer space resistance, which could not be modeled using the Richards model.

To better understand the layer-layer effect on unsaturated fluid flow in a stack of thin non-woven fibrous layers, a comprehensive study was carried out experimentally and numerically on continuous water infiltration into a stack of two polyester 43 gsm layers subject to a 0.3 psi overburden pressure (Chapter4). We previously found in our experimental investigations that water infiltration into a single 86 gsm polyester layer, which had the same thickness as two 43 gsm layers and made of the same material, produced a totally different dynamics of unsaturated fluid flow. This is because water moved toward the bottom boundary of a single layer much faster than with the double layers. The interface resistance caused a delay in water movement towards the bottom layer in case of double 43 gsm layers. We used this as a basis for finding the best approach to model continuous water injection into the center of a double 43-gsm polyester layer pack capable of accounting for the interface effect.

In Chapter 4, we compared both the traditional Richards model and RCM against experimental data. Similar to the liquid redistribution case, the traditional Richards model predicted unrealistically rapid movement of water into the lower layer. This is mostly because the interfacial contact was assumed to be perfect between the two neighboring layers in the Richards model. Based on results of the Richards model and as a result of the very thin nature of the layers, average saturations of both layers linearly increased with comparable slopes having very close values. Contrary to the Richards modeling results, the measured data showed a time lag between the starting times of saturation build-up in the two layers. Additionally, measured saturation profiles versus depth and time were also differed from the numerical results. For instance, at $t=10$ seconds, the measured saturation depth profile was in the form of a bell-shaped function while the Richards model predicted a uniform water saturation profile with depth. We also characterized and simulated the double layer in terms of three homogeneous subdomains using Richards model, thus assuming the interface to be a third virtual subdomain. The interface properties were numerically obtained based on CT images of layers. The unrealistically fast imbibition still persisted in this case, while the profile was slightly better in the interface region. In another approach, the modeling domain was subdivided into fourteen sub-domains to be compared with corresponding measured data points. The saturation depth profiles were predicted reasonably well in this way solving Richards equation. However, the problem of fast movement to

the bottom layer still remained. Results with the traditional Richards model demonstrated that the assumption of two homogenous layers leads to inaccurate saturation profiles for layers whose fibers are not uniformly distributed versus depth. Moreover, the delaying phenomenon due to the interlayer space effect could not be simulated with this modeling approach since perfect contact was assumed between the two layers. In the RCM approach, however, the interlayer effect could be taken into account with the aid of a mass transfer function. This allowed us to introduce a parameter which corresponds to interlayer properties of the two adjacent layers. We validated the RCM approach by applying different injection flow rates at the inlet. Experimental results were simulated reasonably well for the different boundary conditions using RCM. Results of this set of simulations proved the ability of the RCM in modeling through-plane liquid infiltration into a stack of thin fibrous layers compared to the traditional Richards model in terms of layer-layer mass exchange and computational effort.

Finally, applicability of statically measured hydraulic properties of a compressed single thin non-woven fibrous layer was investigated under dynamic fluid flow conditions for a group of six different materials, when a large air pressure step was applied instantaneously (Chapter 5). Results of dynamic inflow simulations using the traditional Darcy two-phase flow model were in good agreement with laboratory data for materials without bonding points, i.e., materials which are bonded with techniques other than calendar bonding (with uniform fiber distribution over their thickness). These layers had perfect contact with a saturated hydrophilic membrane. However, the starting times of saturation buildup in the inflow experiments for materials with bonding points (having bell-shaped fibers distribution over their thickness) showed a clear time delay compared to the two-phase flow modeling results. Again, fast water infiltration into the fibrous layer in the Darcy two-phase flow simulations could be delayed by unrealistically decreasing the relative permeability function and including dynamic capillarity effects. However, we could model systematically all layers without changing the hydraulic properties in the RCM. The λ parameter in the mass exchange coefficient corresponded then to imperfect contact between the two layers. For materials without bonding points, perfect produced a λ value of 1.0. But, when imperfect contact existed, λ had to be decreased by one order of magnitude. Using the same mass exchange coefficient for inflow and outflow simulations,

experimental data of the outflow experiment were predicted reasonably well. Furthermore, the RCM was found to be computationally much faster than the traditional Darcy based models.

In conclusion, the interlayer space effect played a major role in unsaturated fluid flow through a stack of thin porous layers, particularly at low water saturations and slow imbibition and drainage processes. This effect changed depending upon the overburden pressure imposed on a stack of thin layers. The RCM approach proved to be a relatively powerful new technique that enabled us to include the interface effect in the mass exchange coefficient. Additional advantages are that the RCM formulation preserves the REV concept for very thin layers, while also being computationally more efficient than the traditional models.

Samenvatting

Samenvatting

Deze dissertatie gaat over kunstmatig geproduceerde lagen die bestaan uit vezels. Dergelijke lagen worden gebruikt voor het optimaliseren van distributie en absorptie van vloeistoffen, belangrijk in sanitaire producten zoals luiers en verband. De meeste van deze producten bestaan uit meerdere lagen waarbij elke laag een eigen functionaliteit heeft. Voor het optimaliseren van de producteigenschappen is het daarom van belang om te begrijpen hoe een vloeistof door verschillende lagen vezels heen komt.

Sanitaire producten zoals luiers zijn ontworpen om vocht weg te houden bij de huid. Daarom zijn de lagen zo samengesteld dat vloeistof alleen van de bovenste laag naar de onderste laag stroomt. In de onderste laag vindt vervolgens de opslag plaats in speciale superabsorberende polymeerkorrels. Achter deze opslaglaag zit een niet-doorlatende laag om lekkage te voorkomen.

Een aantal processen vinden tegelijkertijd plaats: (1) Twee-fase stroming (lucht + vloeistof) in de dunne vezellagen en de grotere ruimtes tussen de vezellagen, het zwellen van de absorberende korrels, (3) mechanische vervorming van de opslaglaag en (4) het verdampen van de vloeistof uit de verschillende lagen. Het begrijpen en kunnen controleren van deze processen is van grote invloed op het comfort van de gebruiker.

De vezellagen relevant voor dit onderzoek bestaan uit een willekeurige stapeling van vezels. De niet-geweven vezellagen zijn gemakkelijk derformeerbaar, hebben een grote porositeit en een grote permeabiliteit –de doorlaatbaarheid. Druk van buitenaf kan de poriën eenvoudig samendrukken, waardoor de permeabiliteit verandert.

De gebruikte vezels hebben ook verschillende lengtes. Het gevolg van de willekeurige stapeling en de verschillende lengtes is een zeer onregelmatige poriestructuur, in tegenstelling tot geweven vezellagen. Een dunne niet-geweven laag vezels heeft ongeveer 10 – 15 poriën vanaf de bovenkant naar de onderkant. Door dat geringe aantal poriën in de lagen is het van groot belang om ruimte tussen opeenvolgende lagen ook mee te nemen in het ontwerp. Hierdoor ontstaat echter wel een systeem (slechts enkele poriën en een grotere tussenruimte) wat voor de huidige computermodellen lastig is om te modelleren. Deze dissertatie poogt deze kennisleemte in te vullen.

Het vraagstuk is aangepakt met een combinatie van experimentele- en numerieke studies. De hoofdvraag was het onderzoeken van de geldigheid van het traditionele Darcy schaalmodel. Daarnaast is er een nieuw model opgesteld: het gereduceerde continuüm model (reduced continua model – RCM). Beide modellen zijn getoetst aan experimentele observaties.

Het onderzoek begint met een karakterisering van niet-geweven lagen. In hoofdstuk 2 staan de resultaten van een serie experimenten voor de capillaire druk-saturatie relatie van dunne hydrofiele niet-geweven lagen. Op twee verschillende materialen is onderzocht wat de effecten zijn van overbelasting op de laag, opeenvolgende imbibitie-drainage cycli en een toenemend aantal lagen. Het eerste materiaal is een thermisch gebonden niet-geweven polyolefin laag met hechtingspunten. Het tweede materiaal is een laag chemisch gebonden polyester zonder hechtingspunten. De polyolefin laag is later nog gebruikt voor het testen van de verdeling van vloeistoffen en dynamische in- en uitstroom experimenten.

De overdruk opgelegd op een enkelvoudige dunne laag had een significant effect op de gemeten capillaire druk-saturatie kromme. Dit komt door de vervormbaarheid van dergelijke niet-geweven lagen. Door de overdruk veranderde ook de porositeit en de permeabiliteit aanzienlijk. Beide parameters worden gebruikt voor het schalen van capillaire druk-saturatie krommes op basis van de Leveret J functie. Experimentele resultaten kwamen voldoende overeen met deze benadering van schalen.

Een toenemend aantal lagen had weinig effect op de gemeten druk-saturatie kromme. Echter, het dynamische proces van twee lagen was totaal anders in vergelijking tot een enkelvoudige laag. Als we kijken naar een imbibitie-drainage cyclus, dan zien we dat de hoofd imbibitie-kromme beweegt naar een hogere saturatiewaardes en hogere capillariteit in vergelijking tot een primaire imbibitie-kromme. Dit komt doordat er na de primaire imbibitie vloeistof achterblijft tussen de vezels, waardoor de daarop volgende imbibities een grotere saturatie bereiken.

Metingen aan individuele dunne lagen zijn lastig doordat de te meten volumes erg klein zijn. Verbeteringen in de experimentele technieken zijn doorgevoerd om nauwkeuriger resultaten te behalen. De aangepaste opstelling is ook gebruikt voor dynamische in- en uitstroom experimenten. Naast de dunne niet-geweven lagen uit deze studie zijn er ook andere niet-geweven materialen bekeken. Alle resultaten

Samenvatting

zijn bij elkaar genomen en dienen als input voor computersimulaties van vloeistofstromen door niet-verzadigde lagen vezels.

Vervolgens is er bestudeerd hoe de distributie is van een vloeistof over twee vezellagen, zowel experimenteel als met behulp van computersimulaties. Een eenvoudige “NMR MOUSE” is gebruikt om de verandering van water saturatie in de vochtige laag te monitoren ten gevolge van water overdracht naar een droge laag eronder. Het distribueren van water bleek heel klein te zijn en vindt plaats gedurende drie minuten. Deze kleine verandering van saturatie kan worden toegeschreven aan hysteresis van de capillaire druk-saturatie kromme.

Het uiteindelijke evenwichtssaturatie-niveau in de lagen komt overeen met de hysteresis van de druk-saturatie kromme die zijn gemeten voor de vezellaag. Echter, de dynamische verandering van saturatie berekend met het model van Richard is veel sneller dan experimenteel geobserveerd. Het verschil tussen het model en de observaties kan worden verkleind door ofwel de relatieve permeabiliteitsfunctie te veranderen naar hele kleine waarden, of door het toevoegen van een dynamische capillaire term. Daarmee komt het model veel beter overeen met de observaties.

Het is gebruikelijk om het traditionele model gebaseerd op Darcy te gebruiken voor het beschrijven van vloeistoftransport door dunne poreuze lagen. Een fundamenteel bezwaar is het niet kunnen voldoen aan de aanname van een representatief elementair volume (REV). Een REV moet groot genoeg kunnen zijn om lokale heterogeniteit te mogen negeren. In de dunne lagen ongeordende vezels zijn de poriën echter te groot om een REV te mogen aannemen. Bovendien wordt er vaak vanuit gegaan dat opeenvolgende lagen perfect op elkaar aansluiten. Het grensvlak wordt doorgaans niet meegenomen in de modellen.

Daarom is er een nieuw model geformuleerd: Het gereduceerde continuüm model (RCM). Dit model bevat ook de ruimte tussen opeenvolgende lagen door een massauitwisselings-term toe te voegen. Het model maakt een juiste voorspelling van de kortstondige evolutie van watersaturatie door de massauitwisselings coëfficiënt proportioneel te maken aan het harmonisch gemiddelde van de relatieve permeabiliteiten van beide lagen. Het toevoegen van een term voor de dynamische capillariteit was niet nodig.

Verder onderzoek toonde aan dat de bovenlaag van de droge laag minder vezels heeft en daardoor een grotere porositeit heeft dan in het midden van dezelfde laag. De daaruit voortkomende vertraging komt overeen met de weerstand van de tussenruimte tussen de vezellagen, iets wat niet voorkomt in het model van Richard.

Om meer begrip te verkrijgen van het laag-op-laag effect is er uitgebreid onderzoek gedaan naar continuë water infiltratie in een stapeling van twee polyesther 43 gsm lagen met een 0.3 psi overdruk. Eerdere experimenten op een enkellaags 86 gsm polyesther met eenzelfde dikte en samenstelling resulteerde in geheel verschillend dynamisch gedrag. Dit komt doordat water in een enkellaags materiaal veel sneller naar de onderkant kan bewegen dan in een dubbellaags systeem. De weerstand van het grensvlak veroorzaakt een vertraging.

Een vergelijking is gemaakt tussen het model van Richard, het RCM en experimentele data. In overeenkomst met het geval van vloeistof distributie voorspelt het model van Richards een onrealistisch snelle beweging van water naar de onderste laag. Dit komt door de impliciete aanname van een ideaal grensvlak. Uit het model van Richards volgt dat de saturatie in beide lagen ongeveer gelijktijdig oploopt met een sterk vergelijkbare snelheid. Daarentegen laten de experimentele resultaten zien dat er een tijdsverschil is tussen beide lagen. Bovendien zijn de in de tijd gemeten saturatieprofielen anders dan de numerieke uitkomsten. Bijvoorbeeld, na 10 seconde ziet het gemeten saturatieprofiel er uit als een belvormige functie, terwijl het model van Richards een gelijkmatig diepteprofiel laat zien van de saturatie.

Het dubbellaagssysteem met grensvlak is ook gekarakteriseerd en gemodelleerd met drie homogene subdomeinen, waarbij het grensvlak is gedefiniëerd als een derde virtueel subdomein. De eigenschappen van het grensvlak zijn numeriek gebaseerd op CT afbeeldingen van de lagen.

Uit het model volgt nog steeds een onrealistisch snelle imbibitie, maar de saturatieprofielen komen iets beter overeen dichtbij het grensvlak. Bij een andere benadering is het model gesplitst in 14 sub-domeinen die overeenkomen met de experimentele meetpunten. Op deze manier kon het saturatieprofiel best aardig worden voorspeld. Echter, de snelle waterverplaatsing naar de bodem van de twee lagen bleef.

Samenvatting

De resultaten van het model van Richards laten zien dat de aanname van twee homogene lagen leidt tot onnauwkeurige voorspellingen van de saturatieprofielen in ongeordende lagen van vezels. Bovendien kan de vertraging door het grensvlak niet goed worden meegenomen in het model.

Het RCM model is wel in staat om het effect van het grensvlak mee te nemen in de berekening. Hierdoor kan er een parameter worden geïntroduceerd die het grensvlak tussen twee lagen karakteriseert. Het RCM model is gevalideerd door verschillende vloeistofinjectiesnelheden te kiezen. De experimentele resultaten komen redelijk overeen met de RCM simulaties. Daarmee wordt aangetoond dat het RCM model in staat is om een meerlaags materiaal met grensvlakeffecten te modelleren op een computationeel gunstige manier.

De volgende component die aan het model is toegevoegd, zijn hydraulische eigenschappen van samengeperste enkelvoudige dunne vezellagen verkregen uit experimenten. De in- en uitstroom is gemodelleerd als gevolg van een groot instantaan drukverschil. Uitkomsten van het traditionele twee-fase Darcy model voor dynamische vloeistofstromen komen goed overeen met de experimentele uitkomsten in het geval van materialen zonder hechtingspunten. Hierbij geldt dat de hechtingspunten niet met ‘kalenderhechting’ zijn verkregen (met een uniforme verdeling van vezeldikte). Deze lagen hadden een perfect contact met een gesatureerd hydrofiel membraan. Daartegenover is de experimentele starttijd van de opbouw van saturatie in instroom-experimenten van materialen met hechtingspunten (een belvormige vezeldikte distributie) duidelijk vertraagd ten opzichte van het twee-fase vloeistof stromingsmodel (Darcy). Wederom kan de snelle water infiltratie in de vezellaag worden vertraagd door een onrealistische verkleining van de relatieve permeabiliteit en het toevoegen van een dynamisch capillair effect. Maar deze aanpassingen zijn niet nodig als het RCM model wordt gebruikt.

De λ -parameter in de massauitwisselings coëfficiënt komt overeen met een imperfect contact tussen beide lagen. Een perfect contact –een materiaal zonder hechtingspunten – heeft een waarde $\lambda = 1$. In het geval van imperfect contact wordt λ een orde grootte kleiner. Experimentele data van instromend en uitstromend water kan goed worden gemodelleerd met RCM met eenzelfde massauitwisselings coëfficiënt. Daarbij vereist RCM een stuk minder processorkracht dan traditionele Darcy modellen.

In conclusie, de ruimte tussen de twee lagen heeft een significante rol in vloeistofstroming door meerdere lagen dunne poreuze materialen. In het bijzonder als de poreuze materialen een lage saturatie hebben en trage imbibitie en drainage vertonen. De invloed van het grensvlak is afhankelijk van de overdruk op het materiaal.

De RCM benadering is een nieuwe, krachtige techniek die in staat is om het grensvlakeffect mee te nemen in de berekening middels de massauitwisselings coëfficiënt. Bovendien behoudt de methode het concept van REV, ondanks de dunne lagen en tot slot is het minder veeleisend qua benodigde rekenkracht voor een computer.

Acknowledgements

Acknowledgements

I would like to acknowledge a number of people who have encouraged and supported me to fulfil my research in the past four years.

First and foremost, I would like to express my gratitude to my academic supervisor, Majid Hassanizadeh, for opening my eyes to the world of porous media, for supporting and encouraging me from initial to final level of my PhD, and for his invaluable guidance. He taught me how to think critically and motivate me to do research freely. I am deeply thankful for his encouragement to attend conferences and workshops. This work would not have been possible without his contribution to the production of this book and his support in my academic life. As a student and a friend, I would like to thank Majid for his invaluable support. Second, great thanks go to Rodrigo Rosati for his helps, for our numerous discussions and for inviting me to Procter and Gamble Company in Frankfurt. I am thankful for his supports and providing space to set up my experiments in Procter and Gamble laboratory.

I am very grateful to my friend and colleague, Behzad Mohebbi, for his coloration in NMR experiments and for his constructive comments on my research. I am thankful for his enormous support during my stay in Germany. I would like to thank Bernhard Blumisch and Jan Clausen for their comments and suggestions on NMR experiments. Many thanks go to Luigi Digirolamo for his immense support, and also training me to use Autoporosimeter. I would like to thank Dave Maltbie for providing CT images. I gratefully acknowledge my colleagues in Procter and Gamble: Adrian Grenier, Andrea Peri, Cyntia Blanton, Xixi Zhang, Bruno Ehrnsperger, Cornelia Sprengardeichel.

Special thanks go to my doctoral committee, Rien van Genuchten, Marc Prat, Azita Ahmadi, Jacques Huyghe, Amir Raoof for their comments and suggestions. Great thanks go to Rien van Genuchten for fruitful discussions and for his detailed comments on this book.

I would like to thank my colleagues and friends in the Environmental Hydrogeology group of Utrecht University. I really enjoyed various discussions during group meetings and group lunches. I am deeply thankful to my friend and colleague, Chaozhong Qin, for sharing his excellent ideas, for his supports and helps in numerical modeling. I would like to thank our secretaries, Mrgreet and Annuska, for administrative tasks. Many thanks go to Ruud Schotting for his

discussions. I really appreciate my current and former officemates and friends: Luwen Zhuang, Ioannis Zarikos, Willem-Bart Bartels, Tuong Hoang, Jan van Lopik, Hossein Fathi, Ebrahim Ghotbi, and Johan van Leeuwen for having nice talks. Special thanks go to Matthijs de Winter for the Dutch summary translation. I would like to thank Ruben Boelen for his collaboration, which led to production of Chapter 5. Many thanks go to my other colleague and friends in Hydrogeology group: Thomas Sweijen, Amir Raof, Xiaoguang Yin, Enno de Vries, Nikos Karadimitriou, Ehsan Nikooee, Sayantan Ganguly, Pierre Le Fur, Mojtaba Mahmoodlu, Shuai Li., Vahid Jokar-Niasar, Hamed Aslannejad, Lucas van Oosterhout, Vahid Nikpeyman, Suzanne Faber, Lefei Yan, Niels Hartog, Jack Schijven, Gillian Schout.

I would like to thank all my friend in Netherlands and Germany. I am grateful to Majid and Forooz for their support during whole period of my PhD and for nice chats and dinners. Special thanks to Rien and Betty for their encouragements and nice talks. I want to thank Behzad Mohebbi and Mahsa Motarez for their hospitality and delicious dinners and nice discussions in Germany. I would like to thank my other friends in Germany: Mohsen Sotudeh, Salimeh Saleh, Shahed Rezaei, Negar Eftekhari, Reza Najian, Alireza Kavousi, Mohsen Hassanzadeh, Mohammadreza Norouzian, Hamid Rahimi. Special thanks go to Hadi Givi, Hossein Amoohadi, Sepehr Tabatabaie, Ehsan Ansari, Mehdi Mojarad, Hasan Torabi, Amir Golmakani, and many other friends in Iran.

My heartfelt thanks go to my parents and brother for their unconditional support. I would also like to thank family of my wife for their enormous support. Finally, my loving thanks to my wife, Elham, who has helped and supported me in finishing my PhD. While being busy with our lovely son, she helped me a lot during past few months. I really appreciate her endless encouragement and support.

Amir Hossein Tavangarrad
Utrecht
January 2019

